United States Department of Agriculture

# Monitoring Land Surface Phenology in Near Real Time by Using PhenoMap

Charlie Schrader-Patton, Nancy E. Grulke, and Jacqueline Ott

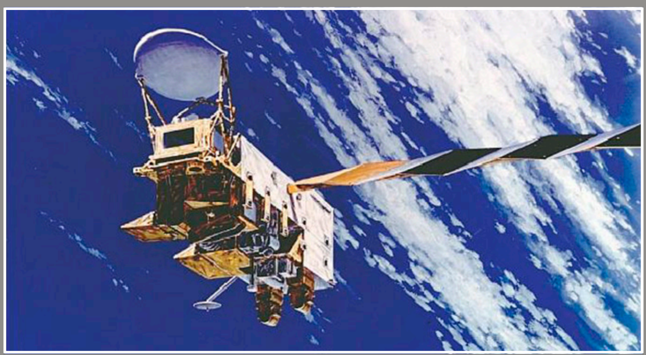

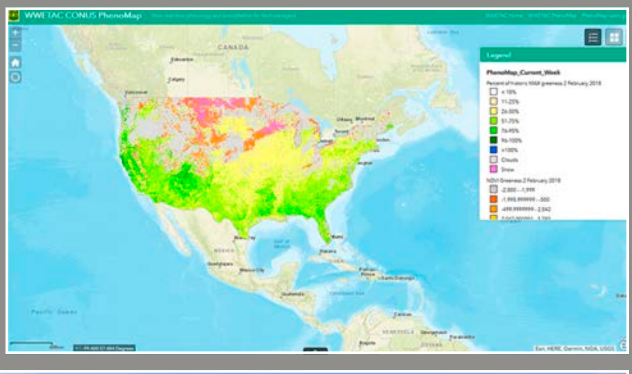


Forest Service
Pacific Northwest Research Station
General Technical Report PNW-GTR-982
February 2020

## Authors

**Charlie Schrader-Patton** is a geospatial analyst, RedCastle Resources, Inc., 2222 West 2 South, Salt Lake City, UT 84119, under contract with the U.S. Department of Agriculture, Forest Service, Geospatial Technology and Applications Center; **Nancy E. Grulke** is a research forest ecologist, U.S. Department of Agriculture, Forest Service, Pacific Northwest Research Station, 63095 Deschutes Market Road, Bend OR 97701; **Jacqueline Ott** is a research ecologist, U.S. Department of Agriculture, Forest Service, Rocky Mountain Research Station, 8221 South Highway 16, Rapid City, SD 57702.

Cover photos: (upper left) National Aeronautics and Space Administration satellite Aqua, part of NASA-centered international Earth Observing System, photo by NASA; (upper right) map generated by PhenoMap Web application; (bottom) a PhenoCam camera in Virginia, photo by Sweet Briar College Land-Atmosphere Research Station.

## Abstract

**Schrader-Patton, Charlie; Grulke, Nancy E.; Ott, Jacqueline. 2020**. Monitoring land surface phenology in near real time by using PhenoMap. Gen. Tech. Rep. PNW-GTR-982. Portland, OR: U.S. Department of Agriculture, Forest Service, Pacific Northwest Research Station. 98 p.

Monitoring vegetation phenology is important for managers at several scales. Across decades, changes in the timing, pattern, and duration of significant life cycle events for plant groups can foreshadow shifts in species assemblages that can affect ecosystem services. In the shorter term, managers need phenological information to time activities such as grazing, ecological restoration plantings, biocontrol of pests, seed collection, and wildlife monitoring. However, tools to deliver timely seasonal development have been limited either spatially (data from a single tower or weather station, or on a single species, or both) or temporally (annually, quarterly, or monthly summaries). We developed another option called PhenoMap. This is a weekly assessment of land surface “greenness” across the continental United States that employs the Normalized Differential Vegetation Index (NDVI) derived from Moderate Resolution Imaging Spectroradiometer (MODIS) satellite data. Here we present the PhenoMap Web map and its validation by using 54 in situ PhenoCam camera sites representing six vegetation structure types and 31 different ecoregions. We found that PhenoMap effectively tracks phenology on grasslands, shrublands, deciduous broadleaf and mixed forests. Results for evergreen needleleaf sites were poor owing to the low green-up signal relative to the total amount of foliage detected by NDVI. Issues of extent and field of view were critical when assessing remotely sensed data with in situ oblique camera imagery.

Keywords: Phenology, vegetation production, NDVI, MODIS, PhenoMap, PhenoCam.

# Contents

## Introduction

Virtually all terrestrial organisms are influenced by the annual cycle of the seasons, either directly or indirectly. Similarly, natural resource managers often schedule activities based on seasonal phases, including grazing, seed collection, tree planting, wildlife surveys, and application of biocontrol agents. Typically, local knowledge of the progression of seasons and the ability to extrapolate/interpolate weather station data has been adequate for resource managers, depending on their length of service in the area. However, managers are being asked to cover increasingly large areas that may be outside their local experience. Moreover, we are currently experiencing environmental change at an unprecedented rate, and these changes do not influence the seasons uniformly across the landscape (Peterson et al. 2011, Reeves et al. 2014). New requirements to address climate change in management plans are being impressed on managers with little specific guidance (Enquist et al. 2014). A near-real-time (NRT) landscape phenology assessment tool allows seasonal vegetation changes to be monitored and is likely to be an invaluable tool in timing management activities for local managers.

In this report, we present our approach to building the PhenoMap tool (https://www.fs.fed.us/wwetac/threat-map/TRMPhenoMap.php) to provide phenological information relevant to management needs. Specifically, we evaluate the ability of this tool to track changes in greenness across 3 years (2014–2016) on 54 sites representing 6 vegetation structure types and 31 U.S. Environmental Protection Agency Level III ecoregions.

PhenoMap is a Web browser map application (Web map) that delivers weekly CONUS-wide[1] raster layers of the current "greenness" of vegetation at a spatial resolution of 250 m. The greenness layer for the current week is updated each Friday, and the previous 3 weeks of data are also accessible in the application. Additional layers available in PhenoMap include weekly precipitation estimates from the National Weather Service, accumulated growing degree-days from the USA National Phenology network, and reference boundary layers (allotments, pastures, federal lands, fire perimeters). PhenoMap is fully self-contained; no geographic information system (GIS) software or data are needed. The only requirements are a Web browser and an Internet connection. Also, PhenoMap can be integrated into the Esri Collector for ArcGIS application for use on Android and iOS (iPad, iPhone) mobile devices.[2]

Validating tools such as PhenoMap is best done with field data that measure vegetation conditions systematically at the pixel level on a weekly basis. However, these data are rare and costly to collect, therefore we used a near-surface remote-sensing network of in situ cameras (PhenoCam, described below) as a surrogate for field data.

---

[1] CONUS = conterminous United States.

[2] The use of trade or firm names in this publication is for reader information and does not imply endorsement by the U.S. Department of Agriculture of any product or service.

# Background

## Phenology

Phenology is the study of the life cycle of a single species or group of similar species; flowering, nesting, migration, and insect emergence are examples of such life cycle events. Phenology provides insights into how species respond to changing environmental conditions and is a sensitive benchmark for monitoring changes induced by climate (Parmesan 2007, Schwartz et al. 2012). Vegetation phenology directly reflects the effects of near-surface temperature and its extremes, as well as water and nutrient availability on processes such as primary production (plant carbon gain), transpiration (plant water loss), flowering, seed-set, and quiescence/dormancy (Chapin et al. 2011). Most terrestrial herbivores have evolved migration or dormancy patterns around the seasonal availability of forage. Insect emergence and development is timed with leaf initiation and flowering of host plant species, and avian reproduction is in turn synchronized with the availability of insect prey. In short, phenology is the drumbeat to which all organisms and ecosystems march.

Remote-sensing technology has made it possible to study vegetation phenology across broad spatial and temporal gradients. This field is known as land surface phenology (LSP) (Meier and Brown 2014). Rather than focusing on the in situ annual cycle of a single species, LSP is the study of phenology as expressed in a pixel, the unit of spatial resolution in remotely sensed data. LSP research centers on the calculation of seasonal transition points such as "start of spring," "peak of growing season," and "end of season," which are based on remotely sensed spectral changes resulting from changes in plant phenology throughout the growing season. These data are typically visualized as a graph with time along the x-axis and spectral reflectance along the y-axis.

# Normalized Differential Vegetation Index

Remote-sensing instruments collect reflected spectral data in distinct areas of the electromagnetic spectrum called bands. Reflectance data from these bands are often combined in indices to increase their effectiveness in discerning features on the ground. These indices usually ratio one or more bands to reduce noise and artifacts from atmospheric influences and topography. The Normalized Differential Vegetation Index (NDVI) was developed to assess vegetation condition in the early 1970s, when Landsat 1 began collecting multispectral data (Rouse et al. 1974); it leverages the red band, which is suppressed in healthy vegetation (owing to absorption by photosynthesis) and the near-infrared (NIR) band, which is slightly reduced in unhealthy or senesced vegetation (fig. 1). NDVI has a long

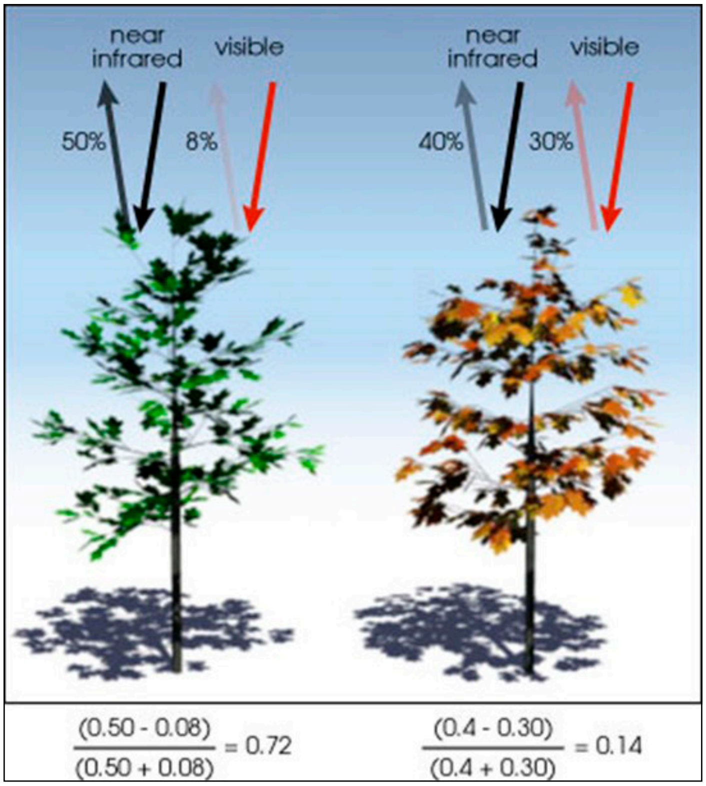


Figure 1—The Normalized Differential Vegetation Index uses the reflectance in the near-infrared and red portions of the spectrum to highlight the differences between healthy peak-season vegetation and senesced, dormant vegetation. (Illustration by Robert Simmon, courtesy of NASA Earth Observatory.)

history of being used to map vegetation characteristics across different land cover types (Hargrove et al. 2009; Malingreau 1986; Rouse et al. 1974), and is a well-established proxy for vegetation "greenness" (Nash et al. 2014, Pettorelli 2013, USDI GS 2017c). NDVI has been used to estimate ecosystem functions like the absorption of photosynthetically active radiation (Grace et al. 2007) and gross primary productivity (Olofsson et al. 2008), and is correlated with carbon dioxide and water flux tower measurements (Balzarolo et al. 2016). LSP researchers use NDVI to evaluate measures of the start of spring (Schwartz et al. 2002, White et al. 2009) and the rate of green-up and time of peak greenness (Reed et al. 1994), as well as in short-term phenology forecasting (White and Nemani 2006). Patterns of NDVI and other vegetation indices across various temporal scales have been used to identify vegetation composition and cause of disturbance within a pixel (Cohen et al. 2010, Dye et al. 2016).

In recent years, the increased availability of historical remotely sensed data has led to a surge in LSP research. Acquisition of the many data layers needed to compose a temporal sequence was an expensive proposition and required significant computer hardware and software, but now these data are freely available. Access to these data has also advanced as cloud-based servers can be harnessed to query, extract, filter, and smooth high volumes of remotely sensed data (see Robinson et al. 2017). Researchers analyze these raster data stacks and look for significant trends in LSP transition points such as an earlier start of spring, magnitude of peak greenness, and extension of the growing season. This information can be important for long-term planning and can be used to compare the current year as it evolves relative to past greenness trajectories in, for example, average or exceptionally dry years. Weekly updates on precipitation and vegetation greenness could help managers forecast fire risk, adjust grazing regimes, optimize biological control applications, and plan restoration plantings and seed collections. They also provide a tool to communicate and document the reasoning behind management decisions.

## PhenoMap

The concept of PhenoMap is rooted in previous efforts to use NDVI-based LSP to assess range conditions (Browning et al. 2010, Gillham and Mellin 2004, Sankey and Weber 2009, Tedrow and Weber 2011); drought (Wardlow et al. 2012); phenology (Reed et al. 1994, Schwartz et al. 2002, White and Nemani 2006); aboveground biomass/production, (Casady et al. 2013, Rossini et al. 2012); and forest disturbance (Chastain et al. 2015, Hargrove et al. 2009). Advances in Web-based GIS have made sophisticated geospatial applications available in Web browsers that previously required a workstation and expensive software. We began investigating Web GIS solutions and potential PhenoMap data sources and methods in 2012, and by 2013 PhenoMap was operational (fig. 2). Several upgrades have taken place, including the recent (2017) expansion to CONUS coverage and the addition of precipitation and accumulated growing-degree-day data (as drivers of vegetation change). PhenoMap is built on the Esri ArcGIS Online cloud-based, software-as-a-service (SaaS) mapping platform (Esri 2018). The U.S. Forest Service has an organizational ArcGIS Online account that can be used to publish geospatial data, services, and applications to support the agency mission. PhenoMap contains more than a dozen basemap options, printing and spatial bookmark tools, and the ability to add local and Web service datasets, and it is open to all users and requires no authentication (username or password). Consult the Western Wildland Environmental Threat Assessment Center PhenoMap Web page for the latest updates and link to the map (https://www.fs.fed.us/wwetac/threat-map/TRMPhenoMap.php).

### Landsat

To develop a near-real-time LSP application, we needed a source of remotely sensed data that can be preprocessed quickly or obtained in a preprocessed state. Additionally, the repeat cycle of the data collection needed to be frequent enough to capture phenological changes and to provide ample opportunities for a cloud-free

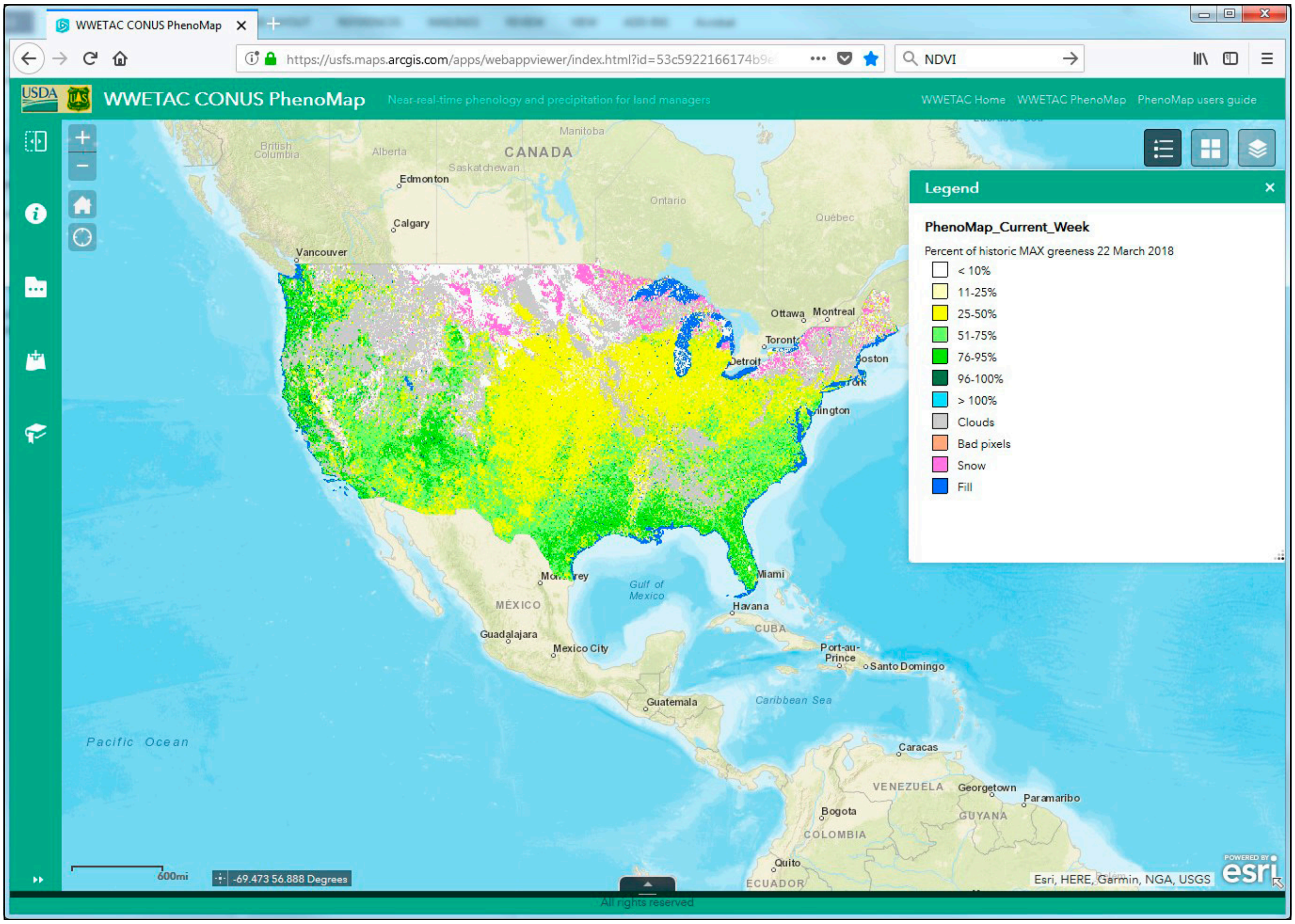


Figure 2—PhenoMap is a Web browser map that displays several weekly land surface phenology map layers, including percentage of historical maximum annual greenness; 14-, 30-, and 60-day cumulative precipitation; and accumulated growing degree-day. PhenoMap is open to all users and requires no software installation or user authentication. To access PhenoMap, go to the PhenoMap Web page on the Western Wildland Environmental Threat Assessment Center (WWETAC) website at https://www.fs.fed.us/wwetac/threat-map/TRMPhenoMap.php.

view of all pixels. The Landsat series of sensors/satellites has a long history of operational data collection (1972 to present), and the 30-m pixel size is suitable for distinguishing most natural resource features. However, the Landsat 16-day revisit cycle is not sufficient to capture NRT phenology, especially in areas prone to cloud cover where there may be a month or more between cloud-free views. Currently, there are two Landsat satellites in operation, Landsat 7 and Landsat 8. They are in offset orbits, which means that together they have a revisit period (the length of time required for the satellite to return to a single ground point) of approximately 8 days. However, Landsat 7 data have been degraded since 31 May 2003, when the scan line corrector failed, so using these data would result in considerable artifacts in an NRT phenology product.

## Moderate Resolution Imaging Spectroradiometer

The Moderate Resolution Imaging Spectroradiometer (MODIS) instrument is present on two satellites, Aqua and Terra, which are part of the National Aeronautics and Space Administration's (NASA) Earth Observing System (EOS). Each MODIS sensor captures reflectance in 36 spectral bands at varying spatial resolutions (nominal resolution at nadir: 250 m (two bands), 500 m (five bands), and 1000 m (29 bands) over the entire Earth's surface every 1 to 2 days.[2] This revisit cycle is due in large part to the 2300-km swath width of the MODIS sensor on both the Aqua and Terra platforms; this makes these data very useful for phenology studies. Although these satellites were not operational until 1999 (Terra) and 2002 (Aqua), the historical depth of the data can be extended by using Advanced High Resolution Radiometer (AVHRR) data. The AVHRR became operational on the NOAA-7 satellite beginning in 1981.

To facilitate use of the MODIS data stream, the U.S. Geological Survey (USGS) Earth Resources Observation Center (EROS) developed a rapid processing system that addresses raw data issues such as variations in radiance resulting from viewing geometry, projection, compositing, and mosaicking. This system is called eMODIS, and it produces atmospherically corrected surface reflectance data for MODIS bands 1 thru 7 as well as NDVI calculated from those bands (Jenkerson et al. 2010). These eMODIS products are created daily from calibrated radiance level 1B MODIS data with a 7-day composite interval to match the historical AVHRR record; these composites are created by using a maximum value-compositing algorithm that isolates the maximum NDVI pixel value for the 7-day interval after filtering for band quality, clouds, snow, poor viewing geometry, and negative surface reflectance. The data type of the composite NDVI raster layer is 16-bit signed integer with a valid range of -1,999 to 10,000. Typically, NDVI values are -1.0 to 1.0, and the eMODIS composites are scaled by 0.0001 to create an integer product. If a pixel is identified that does not have a valid value for the compositing period, it is usually because of persistent cloud or snow cover during the 7-day compositing interval. These pixels are coded with a value of -2000 and can be further classified into clouds, snow, negative reflectance, bad band quality, and fill (Jenkerson et al. 2010). Fill values are assigned when data are missing; most often these are water bodies. The eMODIS NDVI and surface reflectance files are available via file transfer protocol within 24 hours of the last date used in the composite.

[2] The published native resolution for 250 m products is based on arc seconds at the equator. Actual pixel size will vary with latitude.

EOS scientists periodically update the algorithms that are used to convert the raw data from the sensor into derivatives such as the level 1b product used by eMODIS. These algorithms are called collections; the most current is collection 6. With each new collection, updated calibration and geolocation information are used, and all processes to detect atmospheric aerosols, fires, snow/ice, and clouds are revisited (Justice et al. 2002). Historical data are reprocessed with the most recent collection to maintain consistency with current products. In 2016, the MODIS Science Team discontinued collection 5 processing of new layers. Reprocessing of historical data using collection 6 has begun, and all future data will be processed with collection 6 methods (NASA GSFC 2017).

As their names imply, the Aqua and Terra satellites have differences in their orbital characteristics and instrumentation that enable them to focus on ocean and atmospheric applications (Aqua) or land processes (Terra). Terra orbits in a north-to-south trajectory, while Aqua travels in the opposite direction. Terra passes over any given point on the ground at 1030 hours local time, while Aqua will pass that same point at 1330 hours local time. Although the MODIS instruments on board each satellite are identical, they are "decaying" at different rates; anomalies associated with these decay rates are minimized with collection 6 (NASA GSFC 2017).

Initially, we used collection 5 eMODIS data from the Terra satellite, but with the switch to collection 6, eMODIS dropped processing of Terra-based data because of significant sensor degradation.[3] Consequently, we have been using the eMODIS Aqua NDVI data stream for our weekly update since April 2017 and have recalculated the weekly NDVI layer stack back to 2000 using eMODIS Aqua.

**MODIS baseline**—

The greenness level for the current week may be of little value to field managers unless they have a history of observing NDVI values across the landscape. To overcome this, we normalize the NDVI data by calculating the ratio of the current NDVI value and a historical baseline value. This allows the observer to place the current greenness in context with previous years. Researchers have used a variety of baselines to normalize NDVI data, including the historical average (Brown et al. 2008), monthly average (Weier and Herring 2000) and the average of greenness for the same week from prior years (Hargrove et al. 2009). To maintain consistency, we set our baselines as the 2001–2015 mean maximum NDVI value and the 2001–2015 mean midpoint NDVI value. We considered an annually updated baseline where the previous year was added to the data stack. However, this would hinder consistency across years as the median baseline value would change every year.

[3] Wolles, D. 2000. eMODIS question. bulkdatainfo@usgs.gov. (26 September 2018).

## PhenoCam

PhenoCam is a global network of more than 560 cameras that are set at a specific field of view (FOV) and collect multiple images per day (fig. 3). The PhenoCam website (https://phenocam.sr.unh.edu/webcam/) provides image analysis tools and code, in addition to detailed documents on deploying a camera. The cameras typically employ a 3-channel red-green-blue (RGB) sensor that allows extraction of the brightness values (digital numbers [DN]) for each of the individual channels. An increasing number of cameras have added an infrared (IR) band. Software code provided on the PhenoCam website calculates several indices from the RGB data, including the green chromatic coordinate (gcc):

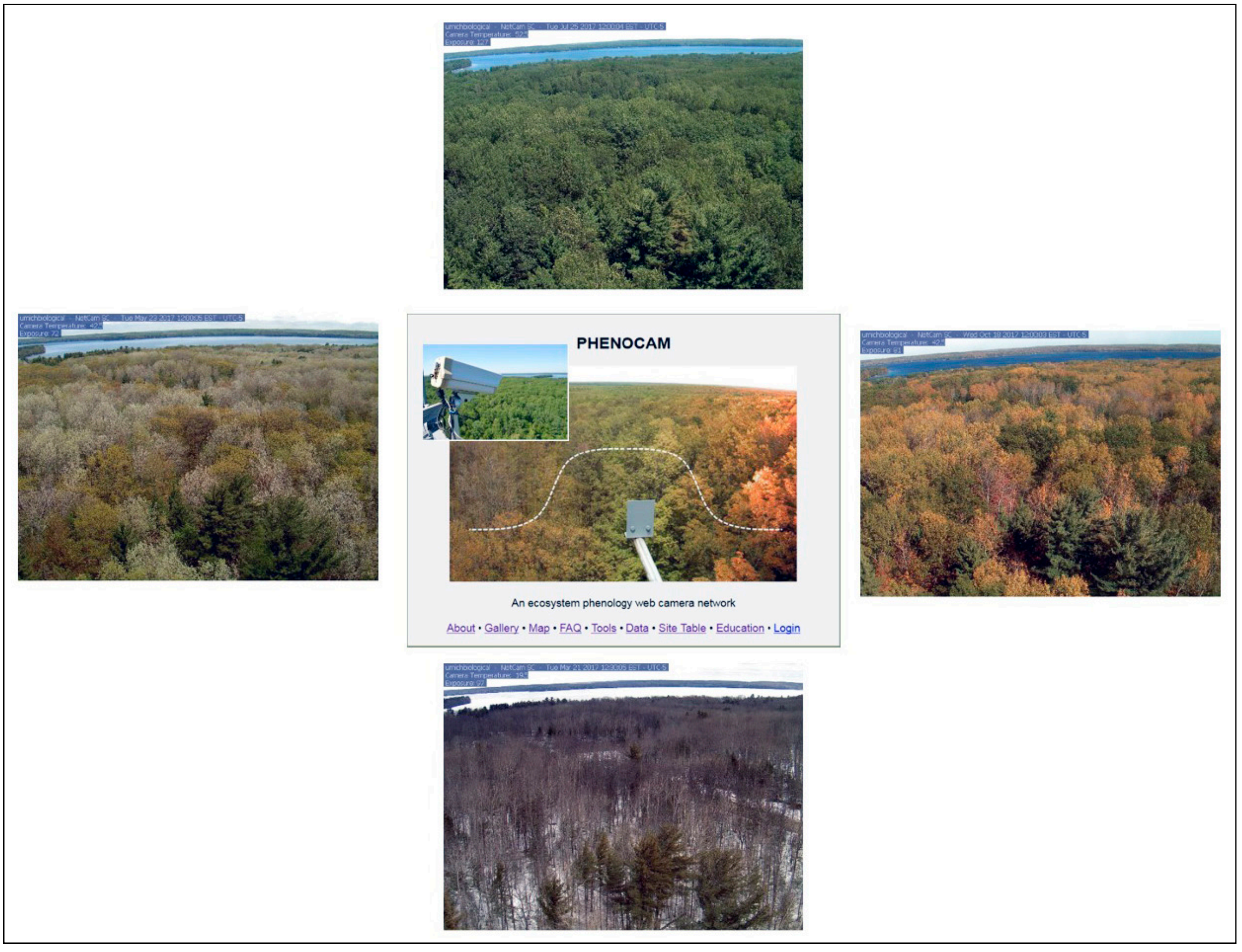


Figure 3—PhenoCam is a global network of more than 560 digital cameras covering a wide variety of biomes. The cameras collect multiple images per day and have a consistent field of view, resulting in a visual record of phenological development. Images and derived data are stored in databases accessed from the PhenoCam website (https://phenocam.sr.unh.edu/webcam/) and are open to all users. The camera sites and infrastructure are hosted by a wide variety of state and federal agencies and academic instituitions.

$$gcc = [DN_{Green}] / [DN_{Red} + DN_{Blue} + DN_{Green}]$$

where $DN_{Green}$ is the digital number for the green channel, $DN_{Red}$ is the digital number for the red channel, and $DN_{Blue}$ is the digital number for the blue channel. The gcc has been recognized as indicator of deciduous broadleaf phenology (Keenan et al. 2014, Sonnetag et al. 2012); canopy greenness and carbon uptake in arid shrublands (Browning et al. 2017, Kurc and Benton 2009); photosynthetic active radiation and rate of canopy photosynthesis (Richardson et al. 2007); aboveground green biomass (Inoue et al. 2015); leaf area index (Liu et al. 2015); and gross primary productivity (Ahrends et al. 2009, Toomey et al. 2015). Also, Sonnetag et al. (2012) found that gcc was superior to other indices in suppressing noise resulting from scene illumination differences; to further reduce these anomalies, they recommended the use of the 90$^{th}$ percentile gcc value for a 3-day period ($gcc_{per90}$).

Different plant cover in the image can be targeted by creating a region of interest (ROI) mask that obscures other areas of the image. Many sites have multiple ROIs, some of which are historical and some that target different species or plant groups in the image. More than 20 statistics and indices based on the RGB DN image values are available for download for each site ROI from the PhenoCam website, including $gcc_{per90}$.

# Methods

## MODIS Baseline

To create an LSP baseline from MODIS data, we obtained annual phenology metric data layers from the EROS data center for 2001–2015 (USDI GS 2017a). Data layers downloaded included the start of season NDVI value (SOSN), described as the NDVI value on the day at which a consistent upward trend in NDVI is detected, and the maximum seasonal NDVI value (MAXN). These EROS phenology layers were created by applying a weighted least-squares temporal smoothing algorithm to the Terra eMODIS weekly composites, then calculating the annual phenology parameters for each year (Swets et al. 1999, USDI GS 2017b). The layers are compiled as the eastern and western parts of the conterminous United States (CONUS); so we merged these layers to create CONUS-wide layers for each metric. For each year, we calculated the midpoint between the SOSN and MAXN to derive the midpoint (MP) layer (fig. 4). Finally the per-pixel median value of the 15 annual NDVI MAXN and MP layers were created; these are the baseline layers used to normalize the weekly eMODIS NDVI composites. Esri ArcGIS v. 10.3 software was used for all processing tasks.

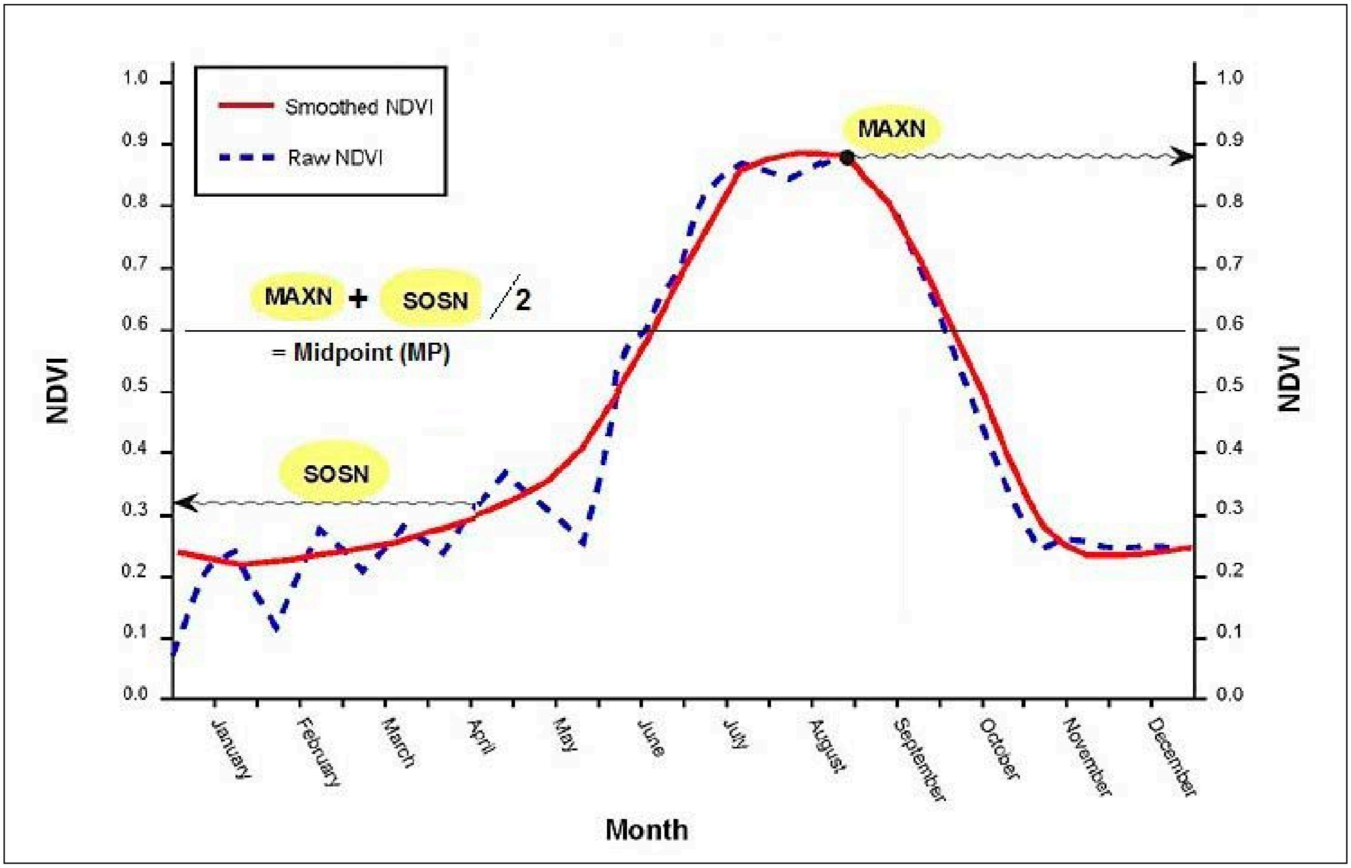


Figure 4—Baseline MODIS, MAXN, and SOSN data were obtained from the U.S. Geological Survey Earth Resources Observation and Science data center for 2001–2015 (USDI GS 2017b). These data were temporally smoothed using techniques described in Swets et al. 1999. MAXN is the maximum NDVI value for a pixel in an annual time series, and SOSN is the NDVI pixel value at the beginning of a consistent upward trend in photosynthetic activity. We calculated midpoint between these two pixel values annually for 2001–2015. (Illustration modified from USDI GS 2017b.)

## Weekly Processing

Terra and Aqua eMODIS 7-day composites are posted on the EROS expedited (eMODIS) data distribution page (https://dds.cr.usgs.gov/emodis/), usually within 12 hours of the last input day (Jenkerson et al. 2010). Seven-day composites are downloaded each Friday. We developed a series of Python scripts to download, uncompress, mask, reproject, and normalize the downloaded 250 m NDVI eMODIS data weekly. Normalization consists of dividing the 7-day composite by each of the 2001–2015 baselines to produce the percentage of historical MAX and percentage of historical AVG (MP) data products. Each eMODIS composite contains a quality layer that identifies pixels flagged as snow/clouds, poor quality (bad bands or negative reflectance), or fill (Jenkerson et al. 2010). We recoded the output raster layers to identify these pixels flagged in the quality layer. Pixels flagged as "fill" typically are water bodies or flooded areas. After recoding using the quality layer, the three raster layers are reprojected and published with symbology classes defined in Esri ArcMap v. 10. 3 software. We published the layers as map services with Esri ArcGIS for Server v. 10. 3 software. Raster files for each of the composite dates are archived for subsequent analyses.

The upgrade to collection 6 included improvements in atmospheric correction, sensor calibration, and geolocation; NASA recommends upgrading to the latest collection whenever possible to leverage these improvements (NASA GSFC 2010). Following this upgrade, the eMODIS team detected anomalous positive data spikes (abnormally high values) in the composite NDVI product (USDI GS 2017b); we filtered out these spikes as part of the data analysis process.

## PhenoCam

We examined all PhenoCam sites across the CONUS and selected 54 sites to validate PhenoMap (fig. 5). These sites were selected based on within-pixel homogeneity and a ROI representing the dominant vegetation in the pixel. Sites that had a complete data record for 2014–2016 were preferred, but we did select some sites that did not meet these criteria. Only nonagricultural sites that had at least 1 calendar year of data were selected. We refer to the sites with the PhenoCam assigned names defined in the metadata for each site. Pixel homogeneity was determined by creating a vector layer of the MODIS pixel boundaries and evaluating the land cover of the pixel that contained the site with imagery available in Google Earth™.

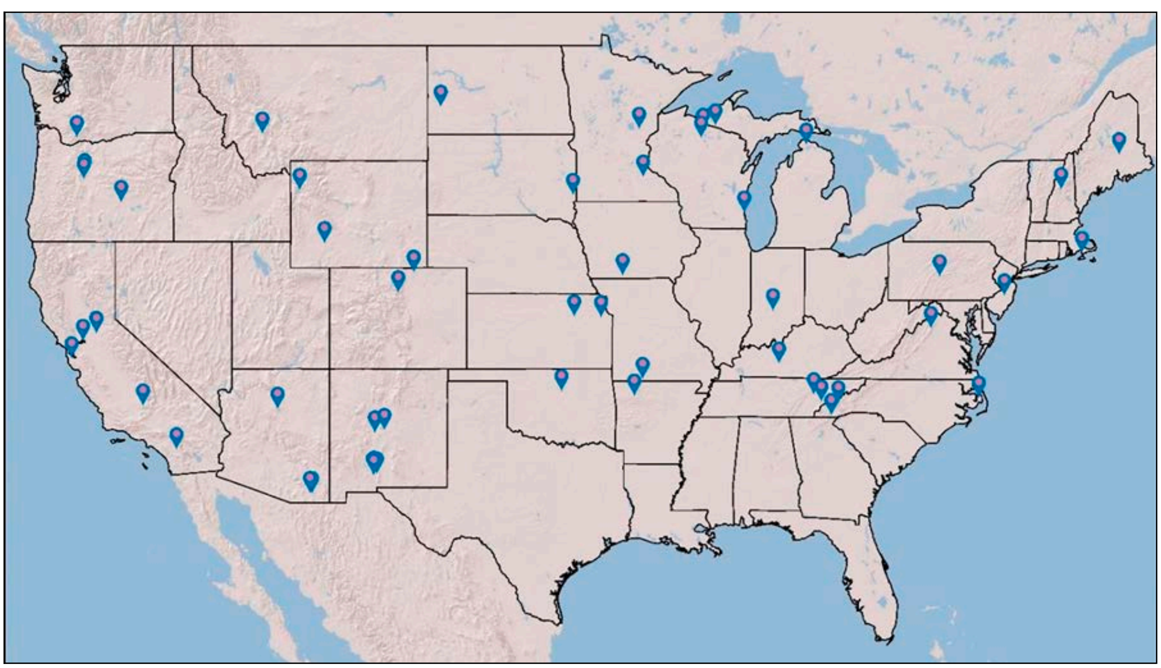

Figure 5—Locations of the 54 PhenoCam sites used in the PhenoMap study.

If the majority of the cover within the pixel matched the vegetation in at least one of the ROIs for the site, and the site contained a data record for at least 2 of the 3 years (2014–2016), then it was selected for analysis. For each site, we downloaded the daily $gcc_{per90}$ data table for the analysis period with Python code and URLs to the PhenoCam website. Included in the PhenoCam metadata for each site were several land cover classifications. We organized the sites by International Global Biosphere Programme (IGBP) land cover classes (Channan et al. 2014) with the following modification: evergreen needleleaf forests were further subdivided into open (percentage of evergreen needleleaf canopy cover greater than 20 but less than 60 percent) and closed (percentage of evergreen needleleaf canopy cover greater than or equal to 60 percent). This classification scheme is referred to as IGBP-modified. This modification was made to distinguish the structural differences in the conifer sites, specifically the increased visibility of understory vegetation in the open needleleaf sites. The PhenoCam site metadata also contained the dominant species present on most sites; if available, these species are listed on the line graphs in appendix 1.

## Analysis

We created a GIS point layer of site locations from coordinates provided by the PhenoCam website. Each site point was examined in Esri ArcMap v. 10.3 software with the pixel boundary layer and moved if the pixel containing the point did not represent the ROI. This was necessary because many of the ROIs consisted of vegetation that was in the middle distance of the FOV and thus outside of the site pixel.

To extract the NDVI data from the raster layers, we used the "multi-value to point" tool in the Spatial Analyst Toolbox within the Esri ArcMap v. 10.3 software. This produced a table with the 2014–2016 weekly NDVI values for the 54 sites. We date-matched the NDVI values tables with the $gcc_{per90}$ values for each site and created graphs and calculated the Pearson's *r* correlation coefficients with Microsoft Excel 2013™ software. Dates in the graphs are expressed cumulatively for the 3-year period. Pearson's *r* values were calculated by year and for the entire 3-year period. When we compiled the overall Pearson's *r* values for each site, we used the value for all 3 years. For those sites that did not have a complete 3-year data record, we used the nearest year to 2016 that had a complete data record.

The eMODIS processing method filters out cloud- and snow-dominated pixels, but many pixels containing thin atmospheric interference or sparse snow cover are present in the NDVI data (Brown et al. 2015). We filtered out (set to #N/A) these cloud- and snow-affected pixels based upon visual analysis of the line graphs. In most cases, snow/cloud-contaminated negative spikes in the line graphs were greater than two standard deviations from the mean of the previous two values before the spike and the two values after the spike. If a negative spike met these criteria, it was designated #N/A. If more than three time periods were cloudy, then these time periods were designated #N/A. We filtered anomalous positive spikes in a similar manner.

We also explored the association between gcc and NDVI by calculating both metrics from a single MODIS MOD09GA date collected on 8 June 2015 with Google Earth Engine (Gorelick et al. 2017). This date was selected because it was a midsummer date reasonably clear of clouds across the CONUS. MODO9GA is a surface reflectance Terra MODIS product containing MODIS bands 1 through 7. Both metrics (NDVI and gcc) were calculated at 65 random points across the CONUS; prior to selection of the points, we masked the imagery so that clouds, water bodies, and other nonvegetated cover types were not included in the point selections. We inspected each point to ensure that it was in a vegetated area (for example, was not in an urban or developed environment), and plotted the points in a scatterplot. Our intent was to visualize gcc vs. NDVI for evidence of a linear or nonlinear relationship.

We examined the site PhenoCam images for evidence of disturbance (grazing animals, ice/storm damage, signs of fire) during the analysis period. The PhenoCam website allows users to search the archive of images for each site. Images for the analysis period were inspected, and if disturbance was evident, the date was noted on the line graphs. For sites on Forest Service lands, we consulted the Forest Service Activity Tracking System geospatial layers, which catalog silvicultural and fuel treatments (USDA FS 2018).

## Results

The 54 PhenoCam sites were in the following IGBP-modified classes: open evergreen needleleaf forest (4 sites); closed evergreen needleleaf forest (2 sites); open shrublands (12 sites); mixed forest (5 sites); grasslands (17 sites), and deciduous broadleaf forest (15 sites). Several sites were placed in a different IGBP-modified class based on the PhenoCam masking of the FOV. For example, the hartprairie site was reclassified as a grassland site because the mixed forest in the background was masked out, isolating the grass cover in the foreground. Originally this site was in the mixed-forest class.

Appendix 1 contains the graphs, scatterplots, and images for all 54 sites in alphabetical order by PhenoCam site name. We found a distinct difference in the NDVI vs. PhenoCam correlations for the needleleaf sites (mean Pearson's $r$ = 0.083137, $n = 6$, four of six sites $p > 0.1$) on the one hand, and the remaining (open shrubland, mixed forest, grassland, and deciduous broadleaf forest) sites (mean

Pearson's $r$ = 0.79, $n$ = 49, all sites $p < 0.001$ except two) (fig. 6; app. 2) on the other. The evergreen sites show a distinct $gcc_{per90}$ seasonal pattern, whereas the corresponding NDVI trend is noisy and erratic (see usmpj, oregonYP, oregonMP, windriver, and niwot sites in app. 1). The deciduous broadleaf sites ($n$ = 15) generally showed well-defined summer greenness peaks and winter dormancy valleys, with the NDVI and $gcc_{per90}$ data matching well (mean Pearson's $r$ = 0.84). All deciduous broadleaf sites were east of the 100$^{th}$ meridian with the exception of tonzi, a blue oak savannah site in the central valley of California. Indications of multimodality suggest slight differences in phenology among species within each site.

There are some observations that can be generalized to most of the sites. Seasonal peaks and corresponding valleys are evident in the line graphs for 2014–2016, especially for the broadleaf deciduous sites. The NDVI data are inherently more noisy (many peaks and valleys representing oscillations from the central trend of the data) than the $gcc_{per90}$.

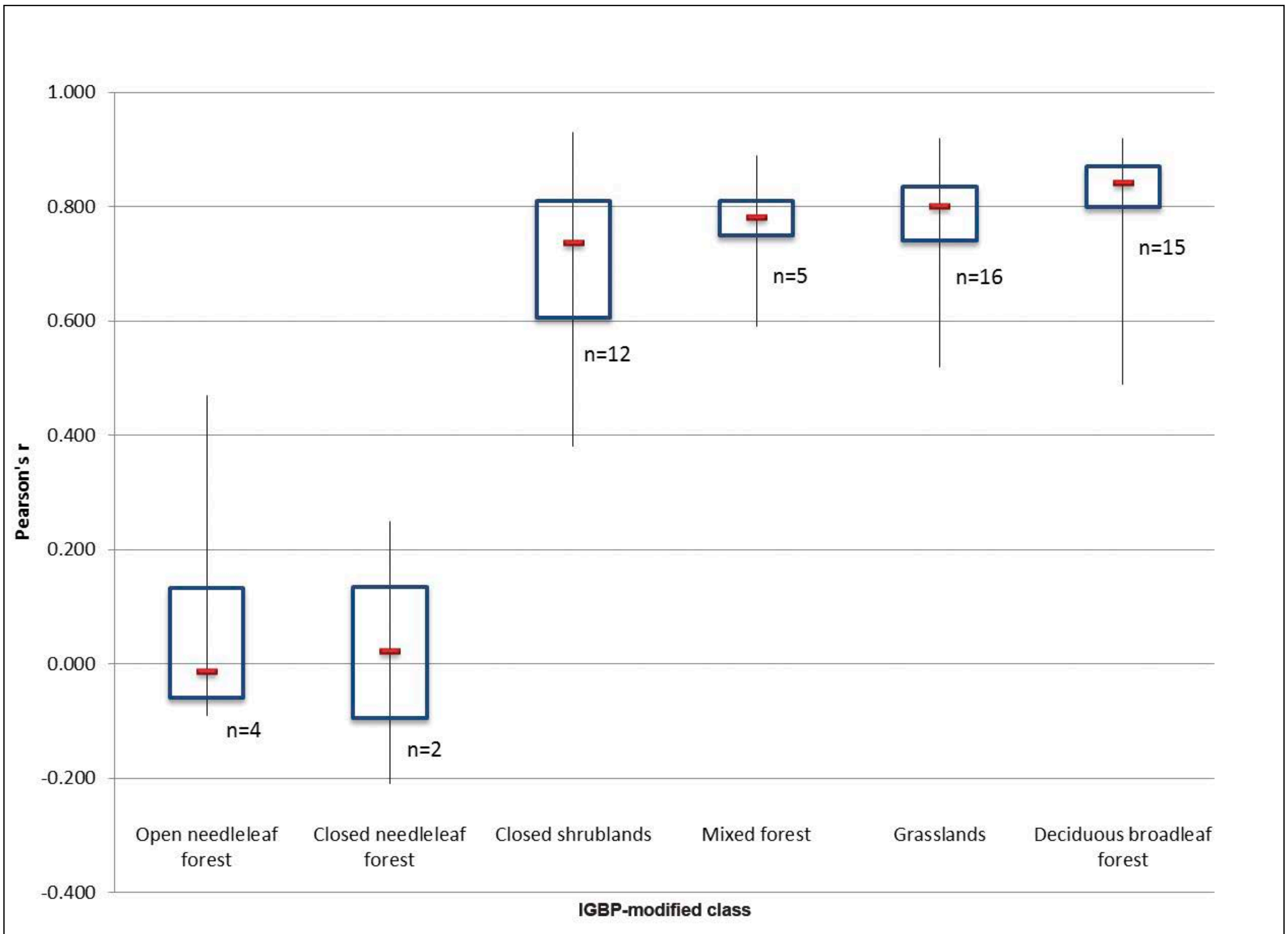


Figure 6—Mean Pearson's $r$ coefficient values for the International Global Biosphere Programme-modified classes.

The mixed-forest sites needleleaf cover percentage (ocular estimate) ranged from 60 percent on howland2 to 20 percent on umichbiological2. With the exception of howland2, these mixed sites exhibited similar trends as the deciduous broadleaf sites. The high needleleaf component in howland2 results in a more erratic NDVI and $gcc_{per90}$ trend. All mixed sites are in temperate forests north of 45° N latitude with the exception of alligatorriver, a bald cypress-tupelo mid-Atlantic coastal plain forest site. The umichbiological2 site $gcc_{per90}$ data has an aberration at day 82 owing to switching ROI masks.

Most of the deciduous broadleaf sites show NDVI lagging behind $gcc_{per90}$ during green-up; the peak NDVI value is often 1 to 3 weeks behind of the peak $gcc_{per90}$ value for the same year. This can also be observed in the mixed-forest, grassland, and shrubland sites, but the lag is not as prevalent. Deciduous broadleaf sites have a sharply defined increase in $gcc_{per90}$ and NDVI during spring green-up, a flat plateau of sustained greenness for approximately 140 days, then a steep decrease indicating fall senescence. Within the summer plateaus, there are often one or more small spikes of greenness (peaklets) that are visible in the NDVI data and to a lesser extent in the $gcc_{per90}$ data.

On sites with overstory canopies (forests and shrublands), the oblique PhenoCam views are biased toward the overstory at the expense of understory grass and forbs, whereas the nadir view of satellite data for these sites is under greater understory influence. The oak/grass savanna tonzi site in the central valley of California is an example of this bias; this site has two ROIs—one for understory grass and one for the overstory oaks (fig. 7). The corresponding data for these two ROIs are correlated to the satellite NDVI dataset reflecting land cover in the MODIS pixel from a nadir perspective (fig. 8). Correlation with the NDVI data is stronger (Pearson's $r = 0.81$) for the tonzi grass component than for the tonzi blue oak (*Quercus douglasii* Hook. & Arn.) overstory component (Pearson's $r = 0.71$). Further evidence of the influence of understory grass on the NDVI measurements is the tight association of the grass $gcc_{per90}$ to the NDVI during a late-season green-up at day 355. This green-up peak is not evident in the $gcc_{per90}$ oak data. The increase in the oak canopy $gcc_{per90}$ (fig. 8a) is much more subtle than that of the grass (fig. 8b), as oak root growth response to increased soil moisture is much slower than that of grass, and a large proportion of the oak foliage was lost in the 2013–2016 drought. Blue oak is a drought-obligate deciduous species, meaning that leaves are shed under extreme drought conditions, and when moisture is abundant, some leaves are retained through the winter (Pavlik et al. 1991). Considering the extreme drought in California during 2011–2016, we would expect significant summer oak leaf loss. A similar grass green-up event around day 355 was also detected at the vaira site, 2.7

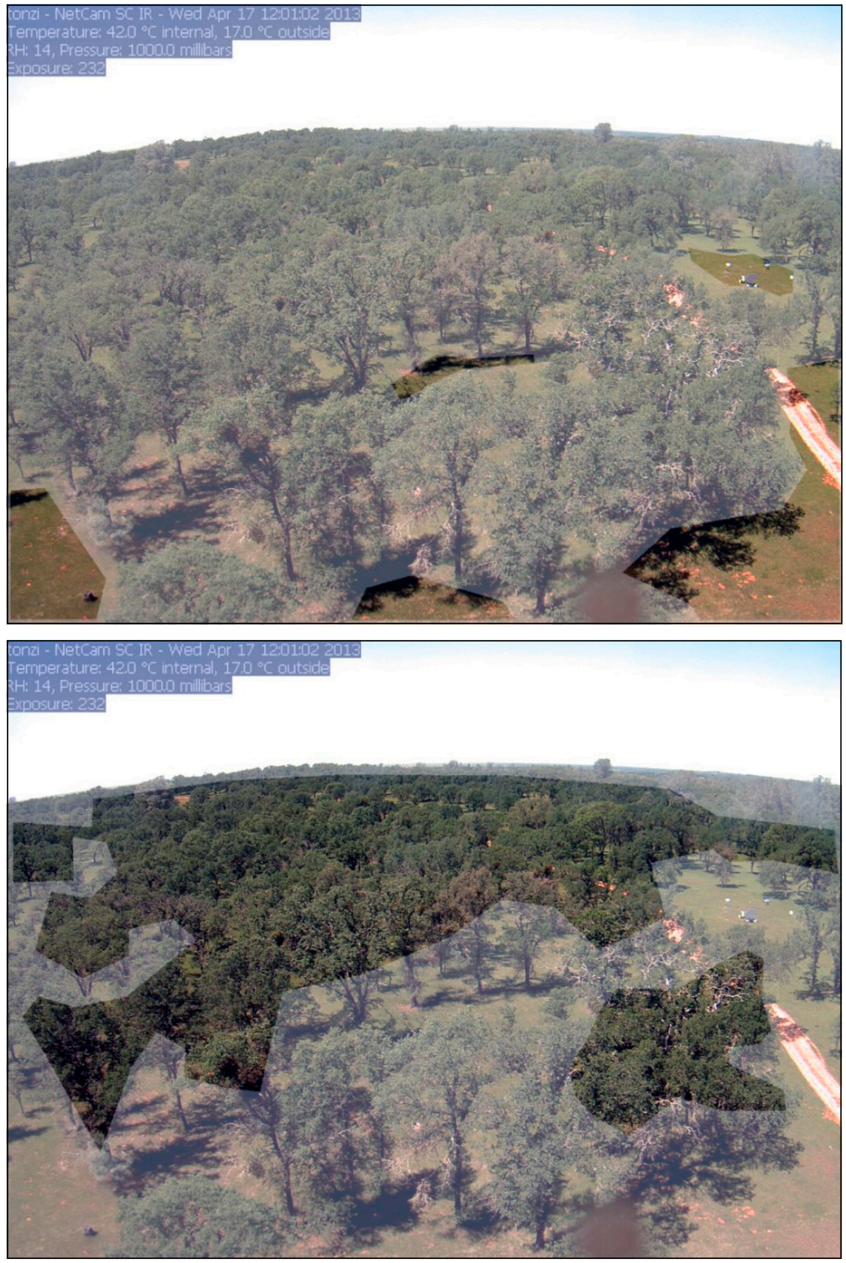


Figure 7—Region of interest (ROI) overlays mask out parts of the PhenoCam image field of view. On the tonzi site the overstory tree component is masked out to focus on (A) the grass understory, and conversely, (B) the grass is masked to isolate the trees.

**A**

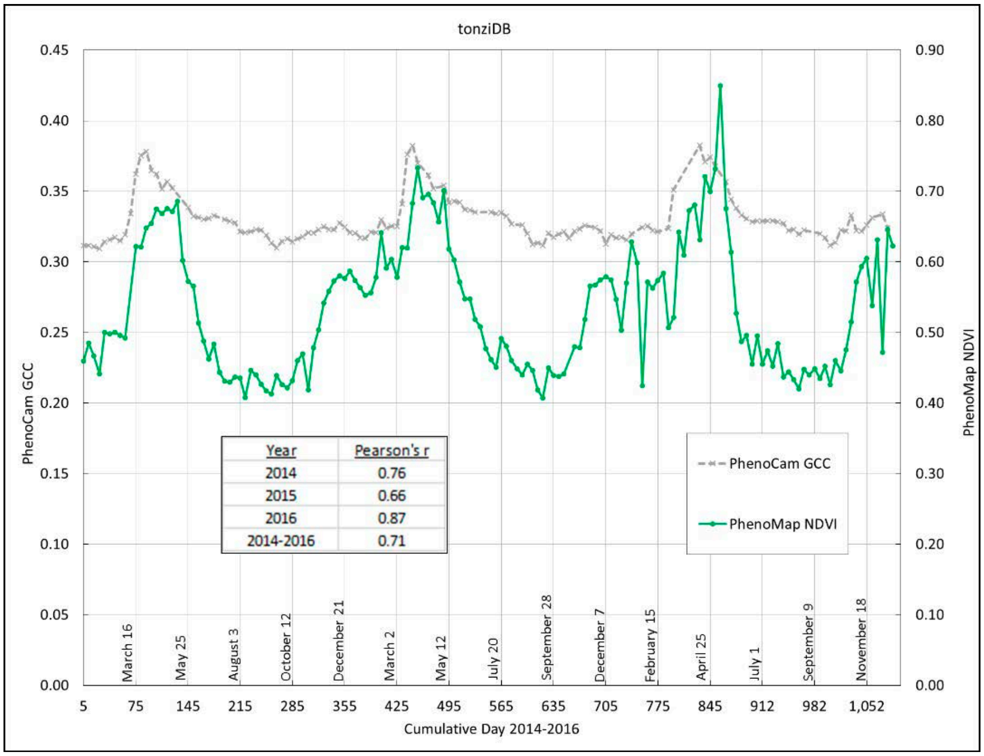


**B**

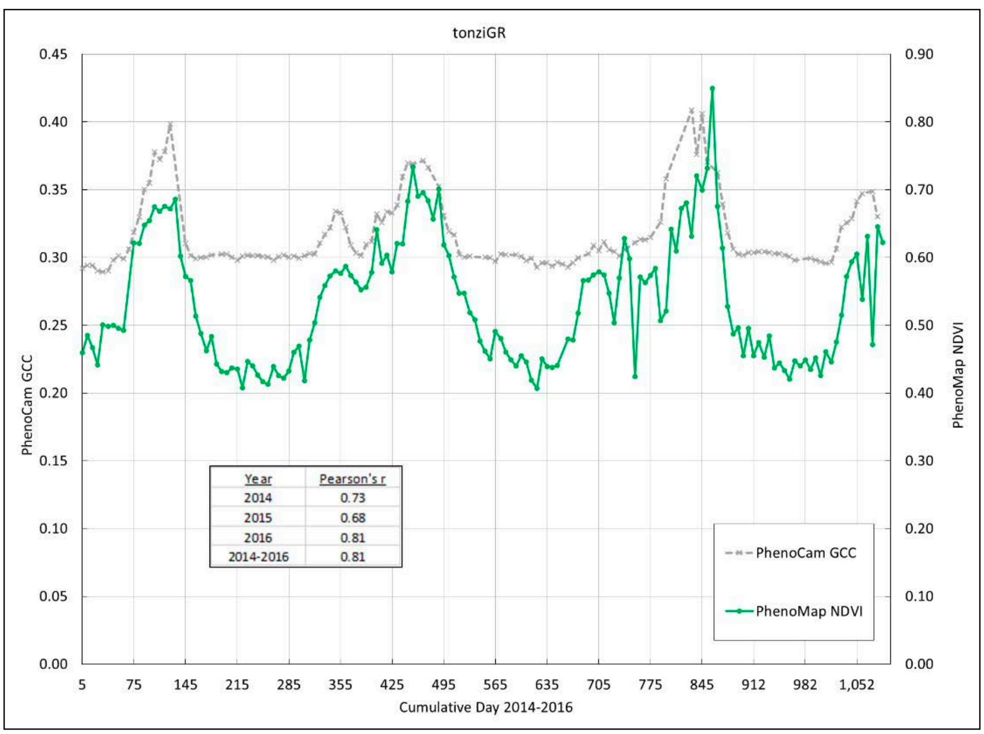


Figure 8—Line graphs of the PhenoCam green chromatic coordinate ($gcc_{per90}$) and PhenoMap eMODIS NDVI weekly values 2014–2016 for (A) the tonzi site deciduous broadleaf component and (B) grassland component.

km to the south (fig. 66a). Leaf area appears to be reduced based on visual exams of the summer (June-July-August) PhenoCam images, while $gcc_{per90}$ values peak in late March, then drop to near seasonal low values by the end of June.

The area selected for calculation of $gcc_{per90}$ (ROI) usually consisted of the overstory shrub or tree species dominant on the site (fig. 9). This has implications for the open shrubland and open evergreen needleleaf sites as understory and ground cover elements are affecting the NDVI value but not the $gcc_{per90}$ value. The eMODIS pixel for usmpj site (fig. 10) shows that an estimated 35 percent of the pixel area is not evergreen needleleaf, presumably the bare ground and sparse bunch grasses suppressed the NDVI signal during the growing season (fig. 11).

The burnssagebrush site did not have a specific sagebrush ROI, but rather the single ROI covers all vegetation in a 1.33-ha area, of which 1.15 ha are within the pixel sampled for the NDVI data (fig. 12). A late-season (November–December 2015) green-up event is evident in the burnssagebrush NDVI data, but not in the $gcc_{per90}$ data (fig. 13). This event corresponds to higher than normal precipitation in November 2014; precipitation that was measured 3 km northwest of the site was 1.06 inches for November 2015, whereas for November 2014 and November 2016, it was 0.43 inch (1.1 cm) and 0.45 inch (1.1 cm), respectively (USDC NOAA 2018).


Figure 9—PhenoCam image of the usmpj site with white outline showing the region of interest (ROI) mask used in calculating the green chromatic coordinate ($gcc_{per90}$). All areas outside of the white polygon were not used in calculating $gcc_{per90}$.

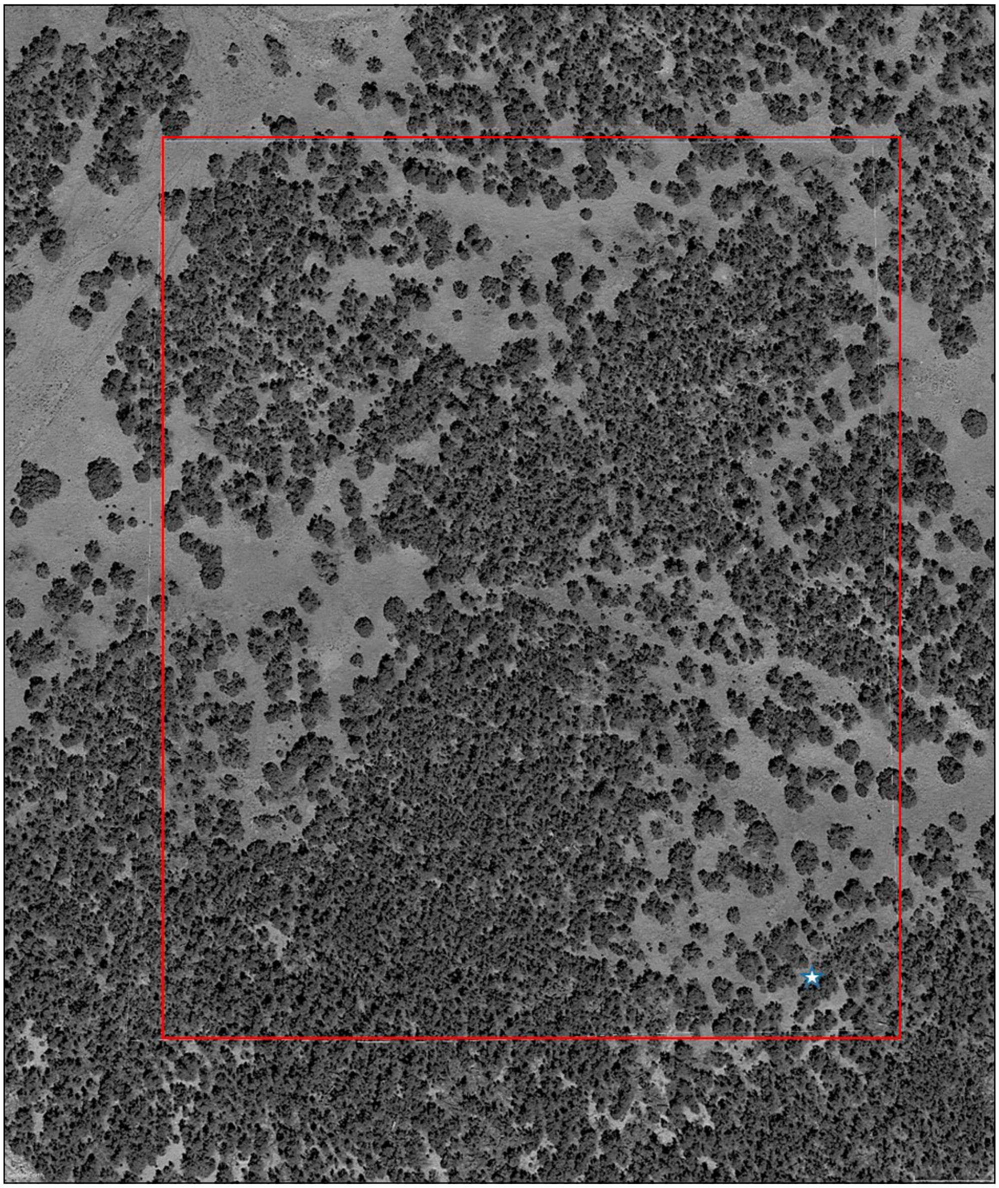

Figure 10—Image of the usmpj phenocam site location (star icon) from Google Earth™. The red outline is the approximate eMODIS pixel boundary. Image source:”usmpj” 34.438450° N and -106.254361° W. Google Earth. 20 April 2013, 26 January, 2018.

The majority of shrubland sites showed some form of multimodality—one or more greenness peaks in a single growing season. Four of these sites are within 20 km of each other on the Jornada Experimental Range in New Mexico; two are dominated by *Larrea tridentata* (DC.) Coville (jersand and jerbajada), and two with *Prosopis glandulosa* Torr. (ibp2 and jernort) in their mix of species. NDVI- $gcc_{per90}$ agreement was much better on ipb2 and jernort (Pearson’s *r* of 0.81 and 0.89, respectively) than jersand and jerbajada (Pearson’s *r* of 0.75 and 0.61, respectively).

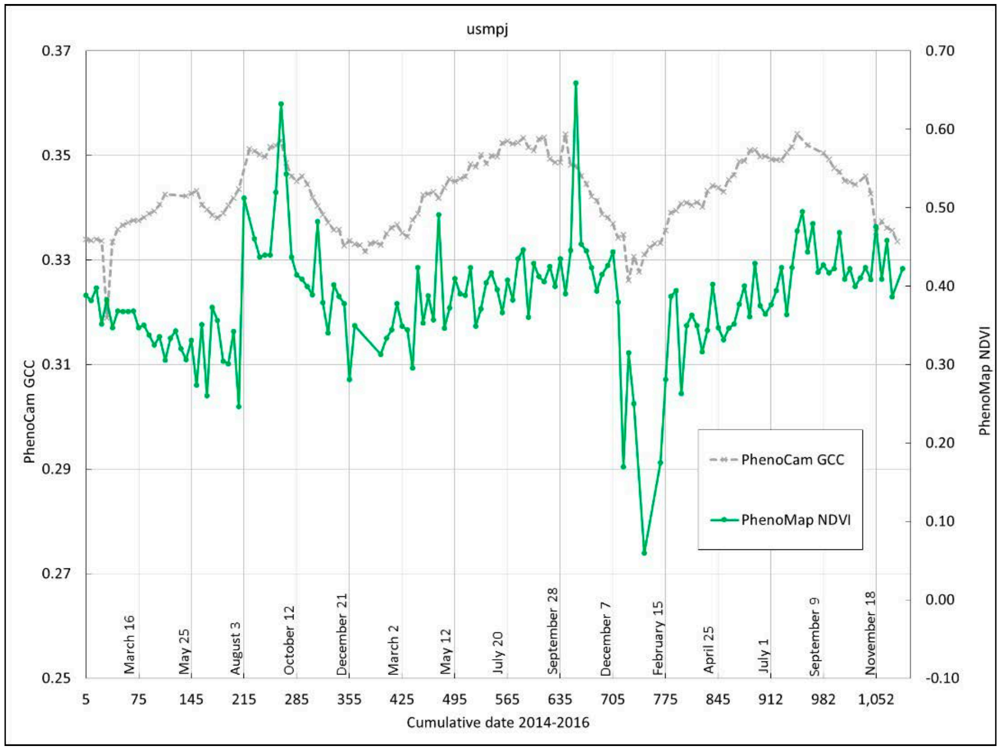


Figure 11—Line graph of the PhenoCam green chromatic coordinate ($gcc_{per90}$) and PhenoMap eMODIS NDVI weekly values 2014–2016 for the usmpj site. The $gcc_{per90}$ response is focused on the overstory (fig. 9), whereas the PhenoMap eMODIS NDVI values are a composite response of all the land cover within the sample pixel (fig. 10).

Despite our efforts to minimize their effects, the eMODIS NDVI data still contained pixels affected by clouds and snow. Snow- and cloud-contaminated NDVI pixels manifest in the data in different ways; the cloudy pixels will not be reflected in the $gcc_{per90}$ because of the oblique ground-level perspective of the cameras and the selection of the 3-day 90$^{th}$ percentile gcc value ($gcc_{per90}$). This method reduces variability as a result of differences in scene illumination (Sonnetag et al. 2012). An example of cloud contamination can be seen in the line graph for the umichbiological2 site (fig. 62b), days 945–1,017. Snow reduces both the $gcc_{per90}$ and the NDVI data, although its effect is less evident with the $gcc_{per90}$ data owing to the oblique perspective of the camera views, which tends to deemphasize ground snow cover.

Most of the sites were established for long-term ecological research and were therefore relatively protected from major disturbance; however, several sites were undergoing grazing or restoration treatments. Kansas State University operates the Konza Prairie Biological Station (KPBS) with the goal of maintaining the tallgrass prairie ecosystem through prescribed burning. The konza PhenoCam site is located in KPBS and was burned on 12 April 2014 (2014–2016 cumulative day 104), 14 April 2015 (2014–2016 cumulative day 469), and 3 May 2016 (2014–2016

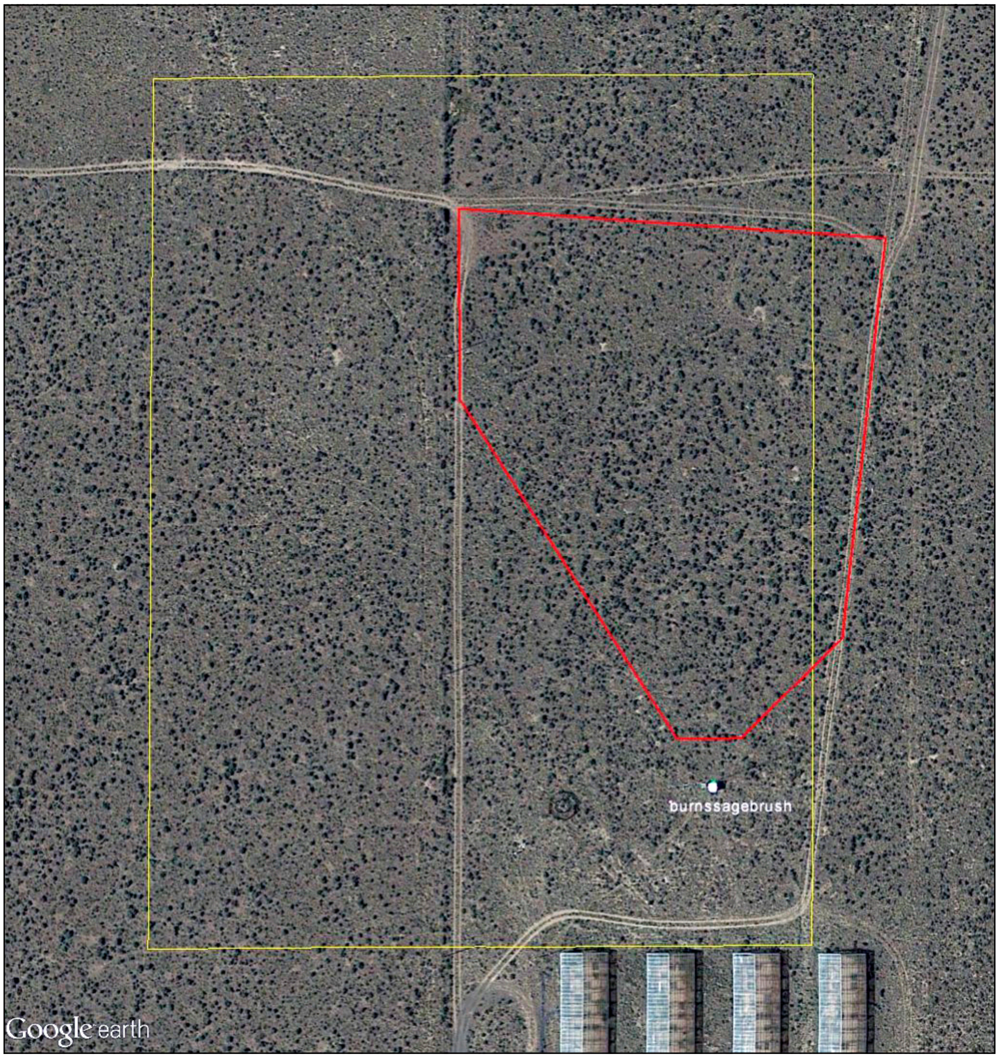


Figure 12—Image of the burnssagebrush Phenocam site location from Google Earth™. The yellow outline is the eMODIS pixel boundary and the red outline is the approximate area covered by the PhenoCam region of interest (ROI). Image source: "burnssagebrush" 43.4712° N and -119.69° W. Google Earth. 8 May 2015, 26 January, 2018.

cumulative day 853). These spring burn events resulted in complete combustion of the biomass produced in the previous growing season, but are not evident in either the $gcc_{per90}$ or NDVI data. The dates correspond exactly to the beginning of the steep rise of $gcc_{per90}$ values with spring (fig. 37b). Cattle grazing occurred on the marena (April 2014, 2015, and 2016) and grandriver (August 2015, July 2016) grassland sites. Inflections in the NDVI signals on or near the dates of these events were not consistent. For marena, an NDVI drop occurred in May 2014 and in April 2015, but not April 2016 (fig. 41b). On the grandrivergrass site, a sharp drop in NDVI is associated with the July 2016 grazing, but no similar drop is associated with the August 2015 grazing (fig. 25a). We were unable to obtain information on

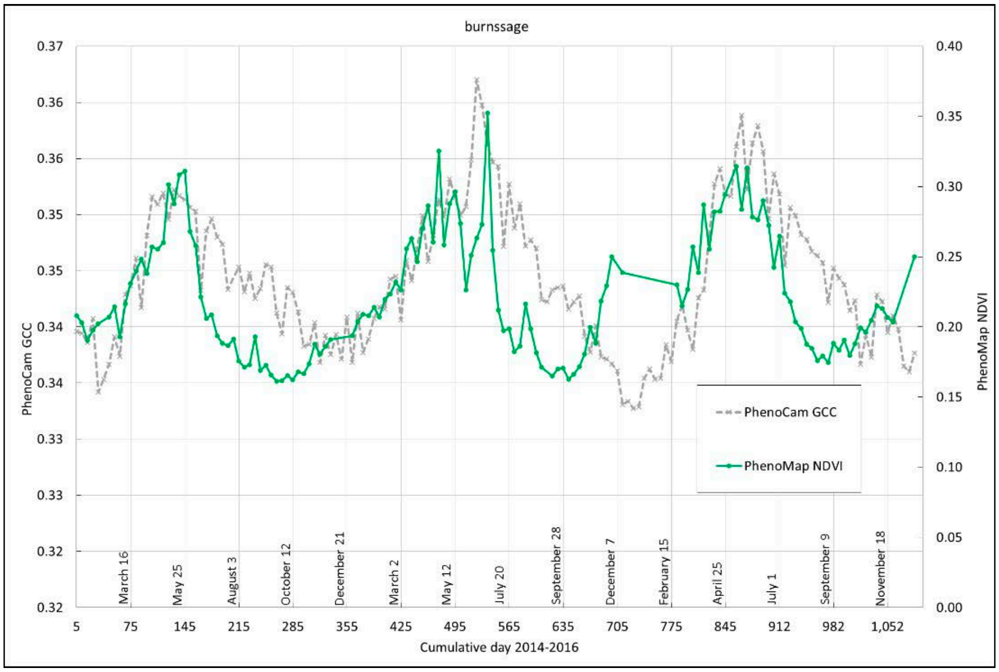


Figure 13— Line graph of the PhenoCam green chromatic coordinate ($gcc_{per90}$) and PhenoMap eMODIS NDVI weekly values 2014–2016 for the burnssagebrush site. Increase in NDVI in late 2015 corresponds to an increase in precipitation (see text).

grazing intensity or duration for either of these sites. The eastend site was completely flooded from January until August 2014 based on the PhenoCam images; this is apparent in the NDVI data (fig. 24b). In 2015 and 2016, this site had more consistent vegetation cover, and it appears that the water component was approximately 10 to 25 percent for these 2 years. This site appears to have undergone a restoration in 2013–2014 that entailed reseeding followed by flooding, probably an activity under the USGS subsidence reversal project (Shouse and Cox 2013). The oregonYP open needleleaf site underwent three fuels treatments in 2015–2016—machine mowing/crushing/compaction of fine fuels (18 January 2019), machine piling (30 September 2015), and burning of piles (10 November 2015) (USDA FS 2018). These activities are difficult to discern in the NDVI data given the high level of noise and are also not apparent in the $gcc_{per90}$ data because the treatments did not remove overstory canopy trees in the oregonYP ROI (fig. 46a)

## Discussion

When developing a tool such as PhenoMap, for which the goal is to support field management, it is essential to conduct validation studies. The cost of collecting weekly field data for even a single season across the many different ecotypes that we hope PhenoMap can represent is prohibitive, so we used the PhenoCam network of near-surface cameras. Weekly greenness ($gcc_{per90}$) measures extracted from these in situ cameras were compared to eMODIS NDVI (PhenoMap) values for 3 years on 54 sites across CONUS.

Upon initial inspection, the line graphs in appendix 1 reveal the inherent noise in the NDVI data compared to the $gcc_{per90}$ data, which is apparent across all sites. This is largely an issue of perspective and extent. Helman (2018) postulated that within-pixel vegetation heterogeneity and multilayered vegetation can confound calculation of LSP metrics such as the start of spring. Undoubtedly, we had similar issues in our study. A mosaic of different plant functional types with different phenological signals may occur within a MODIS pixel, resulting in a more variable NDVI signal than in the PhenoCam images, which cover a smaller area. The eMODIS NDVI pixel is 5.29 ha, and its value is influenced by all vegetation contained within as well as nonvegetated surfaces such as snow, bare soil, and rock. The PhenoCam ROIs usually are focused on one species and represent a fraction of the area of an eMODIS pixel. The tonziDB site exemplifies this with two ROIs (and two corresponding $gcc_{per90}$ datasets) representing the two primary components of the site—*Quercus douglasii* and a mix of understory grasses and forbs (figs. 7 and 8). In this case, the understory is driving the NDVI measurements, not the drought-stressed, blue oak overstory. Within-pixel horizontal heterogeneity is exemplified in the usmpj site (figs. 9 and 10). These issues of perspective and extent cannot be overemphasized and must be considered on a site-by-site basis. We attempted to minimize the effects of vertical and horizontal heterogeneity by selecting sites with a reasonable amount of pixel homogeneity, and by careful selection of the ROI for the PhenoCam site where multiple ROIs were available.

Spaceborne NDVI measurements are subject to cloud, snow, and aerosol contamination. Most of these pixels are excluded in the eMODIS processing algorithm; however, many partially contaminated pixels do make it past the eMODIS filter. We eliminated most of these contaminated values thru visual analysis and outlier filtering; nevertheless, some persist in the NDVI data to reduce the signal-to-noise ratio.

Data smoothing is a process by which an algorithm is applied to a dataset to remove aberrations (noise) while preserving the general trend observed in the data. Many researchers temporally smooth the camera and satellite data (i.e., Browning et al. 2017, Filippa et al. 2018), as this is a prerequisite for determining transition points (start of spring, season peak, end of season), which are then compared across time series. We avoided smoothing because of the potential to lose small features in the data, such as a late-season green-up event or subtle disturbances, and because the data delivered in PhenoMap are not smoothed.

For needleleaf forest types (open and closed), the link between $gcc_{per90}$ and NDVI is poor. This demonstrates the difficulty in tracking phenology with NDVI in conifer-dominated areas, a trend noted by others (Filippa et al. 2018). We were able to use only data for 6 PhenoCam needleleaf sites in this study (oregonYP, oregonMP, niwot, breckenridge, windriver, and usmpj), as other potential sites did not have data within our analysis window (2014–2016).

In contrast to deciduous broadleaf forests, needleleaf forests lack a strong seasonal green-up pulse owing to the relatively small contribution of bud burst and elongation to total leaf area (Jönsson et al. 2010). By definition, these evergreen forests maintain foliage throughout the season, and thus the interannual variability of NDVI levels is low. In addition, phenology progresses at a gradual rate with an extended period of bud elongation in the spring and needle loss in the fall. Combined with the effects of inconsistent illumination, aerosols, clouds and snow, this results in a low signal-to-noise ratio. Needleleaf forests generally have NDVI values lower than deciduous types despite having greater leaf area (Chapin et al. 2011). Spectrally, needleleaf reflectance is generally similar to deciduous leaves throughout the visible portion of the spectrum but differentiate starting in the NIR wavelengths, particularly in the SWIR region (Rautiainen et al. 2018). Needleleaf canopy foliage tends to have lower SWIR reflectance (Rautiainen et al. 2018); this is partially due to needleleaf canopy structure—photons tend to scatter and have a greater chance of absorption. Unlike NDVI, the normalized differential moisture index (NDMI) includes a SWIR band:

$$\text{NDMI} = \text{NIR (MODIS B2)} - \text{SWIR (MODIS B7/NIR (MODIS B2)} \\ + \text{SWIR (MODIS B7)}$$

NDMI may be more effective at tracking conifer phenology and disturbance (Chastain et al. 2015). Other indices that show promise include the chlorophyll/carotenoid index (CCI) (Gamon et al. 2016), and the photochemical reflective index (PRI) (Ulsig et al. 2017). Filippa et al. (2018) provide more evidence that NDVI may be ill-suited for needleleaf phenology. They demonstrate that in situ NDVI did not detect the increase in biomass associated with shoot elongation but did detect new needle formation in eastern white pine (*Pinus strobus* L.).

Snow cover is frequently still present on conifer sites when the trees begin green-up in the spring (Ulsig et al. 2017). This will suppress the NDVI values whereas the $gcc_{per90}$ values (with the PhenoCam ROI focused on the overstory trees) record the increase in photosynthetic activity (Jönsson et al. 2010). This was evident at the niwot site where snow was present well into June of 2014 and 2015. Snow was negligible at the other needleleaf sites.

Our eMODIS NDVI data are 7-day maximum value composites, so a pixel value for a composite date could be as many as 7 days before to the composite date. During green-up we can assume that the maximum value is close to the composite date; however, as the season winds down, the maximum value for the composite period is more likely to be farther from the composite date. This is exhibited as the NDVI curve lagging behind the $gcc_{per90}$ during vegetation senescence. Additionally, $gcc_{per90}$ may be more sensitive to senescent leaves and leaf area loss in grasslands and deciduous broadleaf types than NDVI (Filippa et al. 2018). This is not an obvious trend that can be seen in our data, probably because of the inherent heterogeneity in vegetation in a single MODIS pixel and possible cloud contamination of NDVI low values.

The presence of the near-infrared band in NDVI means a high sensitivity to the chlorophyll content in leaves. NDVI detects the drop in chlorophyll before $gcc_{per90}$ and thus cancels out any NDVI lag associated with the 7-day composite method or greater $gcc_{per90}$ sensitivity to senescence. This also may play a role in those sites showing the NDVI lag behind $gcc_{per90}$ during green-up—$gcc_{per90}$ may detect an increase in greenness before an increase in chlorophyll is detected in the NDVI data. This NDVI lag runs counter to that described by Filippa et al. (2018); they reported that NDVI trends ahead of $gcc_{per90}$ during green-up on deciduous broadleaf and grassland sites. However, they compared specific transition dates (start of spring, end of season) from $gcc_{per90}$ and in situ camera NDVI data, whereas we qualitatively compared peak $gcc_{per90}$ and NDVI values. MODIS NDVI green-up values for deciduous broadleaf sites have been shown to be influenced by understory leaf-out, which can occur 8 to 11 days earlier than the overstory canopy (Ryu et al. 2014).

The NDVI lag we see in our data is comparing peak $gcc_{per90}$ to peak NDVI; when we examine the start of season for $gcc_{per90}$ and NDVI (defined as the first upward inflection values), no bias is obvious. On deciduous broadleaf sites, Keenan et al. (2014) observed that leaf development/senescence lagged behind $gcc_{per90}$, and that because of the oblique view of PhenoCam data, maximum greenness is reached before satellite NDVI. Based on this finding, we can assume that NDVI may more accurately represent leaf conditions than $gcc_{per90}$, but this needs to be investigated further, particularly on sites where the understory vegetation can be quantified.

NDVI saturation at high biomass sites (largely because of red band saturation) is problematic as the index fails to respond at values above 0.90 (Huete et al. 1997, 2002). Our analysis of MODIS gcc and NDVI calculated for 65 “wildland” (no agricultural, urban/developed, or water samples) sites exhibits an asymptotic NDVI saturation relative to gcc (fig. 14), indicating the potential for NDVI values to saturate relative to gcc.

Several deciduous broadleaf and mixed-forest sites show asymptotic saturation, and this is a likely source of $gcc_{per90}$ - NDVI error (see figs. 18a, 55a, 58a, 62a, and 69a). Windriver, our only temperate closed-canopy needleleaf site, had an average NDVI of 0.80 for the 3 years of study and showed a lack of NDVI seasonality (summer high, winter low) that was present in the corresponding $gcc_{per90}$ values (fig. 68). Saturation may play a role in the lack of NDVI response to winter dormancy in the mature conifers on this and the other needleleaf sites, but it is also likely that these trees are not truly dormant during the winter, particularly at the windriver site (a temperate site with mild winters). Evergreen conifers are dominant where growing seasons are short and are able to leverage optimal growing conditions without having to create leaves.

It is not surprising that grassland sites show a strong NDVI - $gcc_{per90}$ correlation (mean Pearson's $r$ = 0.81). Structurally, these sites are not complicated by multiple canopy layers and are dominated by one plant functional type (grass). Like the deciduous broadleaf sites, many grassland sites have multiple summer peaks (multimodal),

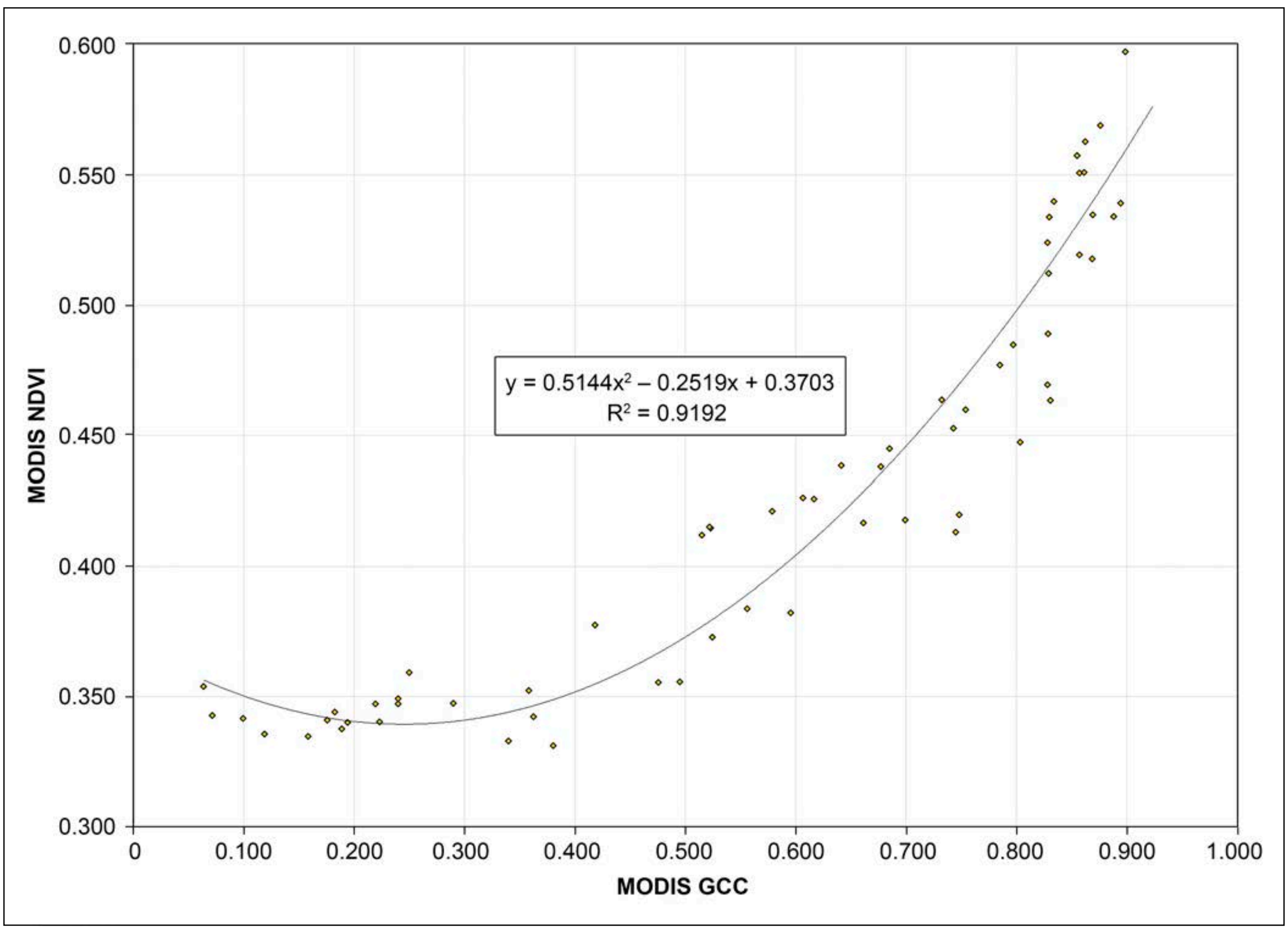


Figure 14—Scattergraph of MODIS NDVI-MODIS GCC (green chromatic coordinate) values for 65 randomly selected points across the conterminous United States.

which may be the phenological response of different species or responses to precipitation events. When precipitation occurs during winter, we suspect that the corresponding green-up event is at least partially the result of moisture altering the spectral properties of the soil and senesced plant material, as the cold temperatures are not conducive to plant development. Dominant species for each site were provided in the PhenoCam metadata, and the majority of the multimodal sites had multiple dominant species. To confirm that NDVI is registering different species, more detailed plot data are needed, including identification of species in the PhenoCam imagery. Bare soil has been shown to confound NDVI assessments of biomass, particularly if the bare soil is 20 percent or more of the pixel area (Huete and Jackson 1987, Sankey and Weber 2009). One grassland site in this study (sevilletagrass) has an estimated 20 to 25 percent of bare soil and a low signal-to-noise ratio, particularly in 2015 (fig. 50). Bare soil may be a major factor in this $gcc_{per90}$-NDVI noise, but further study with additional in situ camera data would be required for a definitive answer. Other studies have compared NDVI measurements over arid sites ranging from 10 to 30 percent bare soil to biomass (Sankey and Weber 2009) or other biophysical parameters such as leaf-area-index (Huete et al. 1994); these results may not be applicable in this comparison of two spectrally derived metrics ($gcc_{per90}$ and NDVI). However, the $gcc_{per90}$ to NDVI correlation at this site is substantially weaker (Pearson's $r = 0.59$) than the average for all grassland sites (Pearson's $r = 0.80$). Alternative vegetation indices have been developed specifically for areas with significant bare soil or urban areas; see Piyoosh and Ghosh (2017) for a thorough review of these indices.

Three grassland sites had documented disturbances—grazing and burning. These were detectable in the $gcc_{per90}$ - NDVI data, but not consistently. The konza site was burned in April of all 3 years as spring green-up was beginning, so the effect of fire on greenness was lost owing to the postburn steep increase in both NDVI and $gcc_{per90}$. The burns are primarily removing dead grass from the previous year's crop before any new grass has emerged. Because the burns occurred in April of all 3 years, we do not have a comparison year with no burn. Burns increase light availability and soil surface temperatures following fire. Although nitrogen (N) is volatilized during fire, unburned tallgrass prairie that has been recently burned will have greater N availability than an annually burned prairie (Seastedt and Ramundo 1990). The increased light and N availability in infrequently burned grasslands can result in an increase in chlorophyll content over prefire vegetation; presumably, NDVI and $gcc_{per90}$ would also increase. Possibly the burns accelerate the phenology, so a year with no spring burn might have a reduced rate of spring green-up.

More research is needed on the level (duration, intensity) of grazing that can be detected with NDVI and PhenoCam; the addition of camera sites on pastures under experimental grazing regimes at the Central Plains Experimental Range near Nunn, Colorado, in 2015 and 2016 provides an opportunity for this investigation.

The shrubland sites ($n = 12$) are predominately west of the $100^{th}$ meridian with the exception of lostcreek, an alder-willow wet meadow complex in northern Minnesota. These western sites are moisture limited, so most of the green peaks are probably related to moisture events as we observed at the burnssagebrush site. Also notable at the burnssagebrush site is the discontinuity between NDVI and $gcc_{per90}$ between November 2015 and February 2016, which corresponds to an increase in precipitation during that period. The pixel has a higher percentage of grasses and forbs visible than the ROI and thus the NDVI response to the rainfall event, whereas $gcc_{per90}$ does not. The timing of peak greenness for the *Artemisia*-dominated sites (quickbird, burnssagebrush, and grandteton) coincides with rapid shoot growth in *Artemisia tridentata*—mid May to early July (Barker and McKell 1986). Similarly, there are green spikes in September and October, which roughly correspond to the flowering period observed near Clarkston, Washington (Tirmenstein 1999).

*Larrea tridentata* (creosotebush) is a long-lived perennial desert evergreen shrub with thick waxy leaves (Marshall 1995). Phenological events (leaf-out, flowering) are largely controlled by precipitation; in drought years, significant defoliation can occur (Marshall 1995). In contrast, *Prosopis glandulosa* (honey mesquite) is a deciduous shrub or small tree with an extensive root system adapted for arid soils. Bud burst occurs in mid-April, and leaves are fully expanded by mid-May and drop with the first hard frost, usually in November or December (Steinberg 2001). These differences are apparent in the sites jernort and ibp2 (*Prosopis glandulosa*-dominated), which have a distinct green-up, peak season, and dormant period typical of deciduous broadleaf sites (figs. 30 and 33). The jersand and jerbajada (*Larrea tridentata*-dominated sites) have a noisier $gcc_{per90}$ - NDVI pattern typical of evergreen forest sites. The greater signal-to-noise ratio of the *Prosopis glandulosa*-dominated sites means stronger $gcc_{per90}$ - NDVI correlation (mean Pearson's $r$ = 0.83) than that of the *Larrea tridentata* sites (mean Pearson's $r$ = 0.68).

## Conclusions

Our efforts essentially are comparing a near-surface method of observing and tracking vegetation greenness with the use of data from a satellite. Although neither method will provide the fine-scale information obtained in species-specific phenological studies, they do provide managers with a synoptic landscape view of phenology that can help track vegetation changes resulting from an increasingly volatile climate.

Our work has demonstrated that MODIS NDVI (and by extension PhenoMap) tracks land surface phenology successfully in grassland, shrubland, mixed-forest, and deciduous broadleaf forest vegetation types, despite the confounding factors of snow, clouds, and observation extent/perspective. This assertion is contingent on acceptance of $gcc_{per90}$ and NDVI as analogous measures of vegetation greenness; undoubtedly there are differences between the two indices. We selected NDVI over other indices because of its long history in land surface phenology and vegetation mapping studies, so these results can be compared to a large body of previous work. Also, the eMODIS NDVI data were readily available—an important consideration in a near-real-time application. Likewise, the $gcc_{per90}$ metric we used is calculated by the PhenoCam processing software and is easily obtained via download; this enabled us to analyze a fairly large number of sites because we did not have to download and process large stacks of PhenoCam images.

Needleleaf seasonal patterns were poorly detected by NDVI; however, our low number of sites (six) makes this result inconclusive. Assessing phenology of needleleaf types by using NDVI should be done cautiously. Since 2016, PhenoCam has added dozens of new sites, some of which are needleleaf. Future efforts on these sites should focus on other vegetation indices from satellite or airborne data such as NDMI. The majority of these newer sites use cameras capable of capturing IR reflectance, which will enable calculation of indices such as NDMI and NDVI from PhenoCam images.

Ultimately, the nature of land surface phenology is that it is an amalgamation of spectral reflectance from all the land cover in a pixel. For MODIS, that pixel is 5.29 ha, and the likelihood of land cover heterogeneity within that pixel is high. With their local knowledge of the ground, managers can focus on rapid and large changes or relatively homogenous key indicator areas such as pastures, meadows, and stands—or both. These key indicator areas can be monitored with PhenoMap and extrapolated to other areas. Focusing on these changes and areas will aid interpretation of more heterogeneous areas and will provide much needed phenological insight for short-term management decisions such as timing, location, and duration of grazing permits.

Rapid changes in the climate promise to bring an unprecedented level of uncertainty for natural resource management. Extreme events such as droughts will be more common. Models tell us that these changes will differ across both space and time, so simple answers—such as that it will be warmer and wetter in a region by 2050—are misleading at best. Developing management strategies that employ information from near-real-time LSP observations from monitoring tools like PhenoMap will allow managers to incorporate resilience and adaptation in an environment of shrinking budgets.

## Plant Species Identified in This Report

| Scientific name | Common name |
|---|---|
| *Abies amabilis* (Douglas ex Loudon) Douglas ex Forbes | Pacific silver fir |
| *Abies concolor* (Gord. & Glend.) Lindl. ex Hildebr. | White fir |
| *Abies lasiocarpa* (Hook.) Nutt. | Subalpine fir |
| *Acacia constricta* (Benth.) Seigler & Ebinger | Whitethorn acacia |
| *Acer rubrum* L. | Red maple |
| *Acer saccharum* Marshall | Sugar maple |
| *Achillea millefolium* L. | Common yarrow |
| *Adenostoma fasciculatum* Hook. & Arn. | Chamise |
| *Adenostoma sparsifolium* Torr. | Redshank |
| *Agropyron cristatum* (L.) Gaertn. | Crested wheatgrass |
| *Alnus* spp. | Alder |
| *Alnus incana* (L.) Moench | Gray alder |
| *Andropogon gerardii* Vitman | Big bluestem |
| *Arctostaphylos manzanita* Parry | Whiteleaf manzanita |
| *Artemisia arbuscula* Nutt. | Little sagebrush |
| *Artemisia tridentata* Nutt. | Big sagebrush |
| *Artemisia tridentata* Nutt. ssp. *wyomingensis* Beetle & Young | Wyoming big sagebrush |
| *Avena* spp. | Oat |
| *Balsamorhiza sagittata* (Pursh) Nutt. | Arrowleaf balsamroot |
| *Betula alleghaniensis* Britton | Yellow birch |
| *Betula papyrifera* Marshall | Paper birch |
| *Bothriochloa saccharoides* (Sw.) Rydb. | Silver bluestem |
| *Bouteloua curtipendula* (Michx.) Torr. | Sideoats grama |
| *Bouteloua eriopoda* (Torr.) Torr. | Black grama |
| *Bouteloua gracilis* (Willd. ex Kunth) Lag. ex Griffiths | Blue grama |
| *Brachypodium distachyon* (L.) P. Beauv. | Purple false brome |
| *Bromus* spp. | Brome |
| *Bromus inermus* Leyss. | Smooth brome |
| *Bumelia lanuginosa* (Michx.) Pers. | Gum bully |
| *Carya* spp. | Hickory |
| *Carya cordiformis* (Wangenh.) K. Koch | Bitternut hickory |
| *Carya ovata* (Mill.) K. Koch | Shagbark hickory |
| *Carya tomentosa* (Lam.) Nutt. | Mockernut hickory |
| *Centaurea maculosa* L. | Spotted knapweed |
| *Centaurea solstitialis* L. | Yellow star-thistle |
| *Ceanothus* spp. | Ceanothus |
| *Cercis canadensis* L. | Eastern redbud |
| *Cirsium* arvense (L.) Scop. | Canada thistle |
| *Cynodon dactylon* (L.) Pers. | Bermudagrass |

| Scientific name | Common name |
|---|---|
| *Desmodium sessilifolium* (Torr.) Torr. & A. Gray | Sessileleaf ticktrefoil |
| *Dichelostemma volubile* (Kellogg) A. Heller | Twining snakelilly |
| *Diospyros virginiana* L. | Common persimmon |
| *Elymus canadensis* L. | Canada wildrye |
| *Eragrostis lehmanniana* Nees. | Lehmann lovegrass |
| *Ericameria nauseosa* (Pall. ex Pursh) G.L. Nesom & Baird | Rubber rabbitbrush |
| *Eriogonum umbellatum* Torr. | Sulphur-flower buckwheat |
| *Erodium botrys* (Cav.) Bertol. | Longbeak stork's bill |
| *Fagus grandifolia* Ehrh. | American beech |
| *Festuca idahoensis* Elmer | Idaho fescue |
| *Flourensia cernua* DC. | American tarwort |
| *Fraxinus* spp. | Ash |
| *Fraxinus americana* L. | White ash |
| *Fraxinus pennsylvanica* Marshall | Black ash |
| *Geum triflorum* Pursh | Old man's whiskers |
| *Hypochaeris glabra* L. | Smooth cat's ears |
| *Juniperus monosperma* (Engelm.) Sarg. | Oneseed juniper |
| *Juniperus virginiana* L. | Eastern redcedar |
| *Larrea tridentata* (DC.) Coville | Creosote bush |
| *Linaria vulgaris* Mill. | Butter and eggs |
| *Liriodendron tulipifera* L. | Tuliptree |
| *Lupinus* sp. | Lupine |
| *Melilotus officinalis* (L.) Lam. | Sweetclover |
| *Nyssa aquatica* L. | Water tupelo |
| *Nyssa sylvatica* Marshall | Blackgum |
| *Panicum virgatum* L. | Switchgrass |
| *Parthenium incanum* Kunth | Mariola |
| *Penstemon* sp. | Penstemon, beardtongue |
| *Phalaris arundinacea* L. | Reed canarygrass |
| *Picea engelmannii* Parry ex Engelm. | Engelmann spruce |
| *Picris echioides* L. | Bristly oxtongue |
| *Pinus contorta* Douglas ex Loudon | Lodgepole pine |
| *Pinus edulis* Engelm. | Twoneedle pinyon |
| *Pinus ponderosa* Lawson & C. Lawson | Ponderosa pine |
| *Pinus rigida* Mill. | Pitch pine |
| *Pinus strobus* L. | Eastern white pine |
| *Poa pratensis* L. | Kentucky bluegrass |
| *Poa secunda* J. Presl. | Sandberg bluegrass |
| *Populus tremuloides* Michx. | Quaking aspen |
| *Prosopis glandulosa* Torr. | Honey mesquite |
| *Pseudoroegneria spicata* (Pursh) Á. Löve | Bluebunch wheatgrass |

| **Scientific name** | **Common name** |
|---|---|
| *Pseudotsuga menziesii* (Mirb.) Franco | Douglas-fir |
| *Quercus* sp. | Oak |
| *Quercus alba* L. | White oak |
| *Quercus coccinea* Münchh. | Scarlet oak |
| *Quercus douglasii* Hook. & Arn. | Blue oak |
| *Quercus falcata* Michx. | Southern red oak |
| *Quercus marilandica* Münchh. | Blackjack oak |
| *Quercus muehlenbergii* Engelm. | Chinquapin oak |
| *Quercus prinoides* Willd. | Dwarf chinquapin oak |
| *Quercus prinus* L. | Chestnut oak |
| *Quercus rigida* | |
| *Quercus rubra* L. | Northern red oak |
| *Quercus stellata* Wangenh. | Post oak |
| *Quercus velutina* Lam. | Black oak |
| *Rhododendron maximum* L. | Great laurel |
| *Salix* sp. | Willow |
| *Schizachyrium scoparium* (Michx.) Nash | Little bluestem |
| *Schoenoplectus acutus* (Muhl. ex Bigelow) Á. Löve & D. Löve | Hardstem bulrush |
| *Senecio* sp. | Ragwort |
| *Sorghastrum nutans* (L.) Nash | Indiangrass |
| *Taxodium distichum* (L.) Rich. | Bald cypress |
| *Taxus brevifolia* Nutt. | Pacific yew |
| *Thuja plicata* Donn ex D. Don | Western redcedar |
| *Tilia americana* L. | American basswood |
| *Trifolium dubium* Sibth. | Suckling clover |
| *Trifolium hirtum* All. | Rose clover |
| *Tsuga canadensis* (L.) Carrière | Eastern hemlock |
| *Tsuga heterophylla* (Raf.) Sarg. | Western hemlock |
| *Typha* sp. | Cattail |
| *Ulmus americana* L. | American elm |

## Acknowledgments

The authors thank Andrew Richardson, principal investigator for the PhenoCam network (Northern Arizona University), and Tom Milliman, data analyst at the University of New Hampshire, for assistance in extracting data and providing insightful and relevant papers. We also thank the many agencies and personnel behind the PhenoCam sites used in this study for making their data available, as well as the staff at the U.S. Geological Survey Earth Resources Observation and Science Center for continued development of the eMODIS data stream, without which PhenoMap would not be possible. Finally, we thank Robert Chastain, Ian Housman, and Mike Simpson for insightful reviews of the draft manuscript. Chastain and Housman are onsite contract remote-sensing analysts, USDA Forest Service Geospatial Technology and Applications Center, Salt Lake City, Utah, and Simpson is an ecologist, USDA Forest Service, Deschutes and Ochoco National Forests.

## U.S. Equivalents

| When you know: | Multiply by: | To find: |
|---|---|---|
| Centimeters (cm) | 0.394 | Inches |
| Meters (m) | 3.28 | Feet |
| Meters | 1.094 | Yards |
| Kilometers (km) | .621 | Miles |
| Hectares (ha) | 2.47 | Acres |

## Literature Cited

**Ahrends, H.E.; Etzold, S.; Kutsch, W.L.; Stoeckli, R.; Bruegger, R.; Jeanneret, F.; Wanner, H.; Buchmann, N.; Eugster, W. 2009.** Tree phenology and carbon dioxide fluxes: use of digital photographs for process-based interpretation at the ecosystem scales. Climate Research. 39: 261–274.

**Balzarolo, M.; Vicca, S.; Nguy-Robertson, A.L.; Bonal, D.; Elbers, J.A.; Fu, Y.H.; Grünwald, T.; Horemans, J.A.; Papale, D.; Peñuelas, J.; Suyker, A.; Veroustraete, F. 2016.** Matching the phenology of net ecosystem exchange and vegetation indices estimated with MODIS and FLUXNET in-situ observations. Remote Sensing of Environment. 174: 290–300.

**Barker, J.R.; McKell, C.M. 1986**. Differences in big sagebrush (*Artemisia tridentata*) plant stature along soil water gradients: genetic components. Journal of Range Management. 39(2): 147–150.

**Brown, J.; Howard, D.M.; Wylie, B.K.; Frieze, A.M.; Ji, L.; Gacke, C. 2015**. Application-ready expedited MODIS data for operational land surface monitoring of vegetation condition. Remote Sensing. 7(12): 16226–16240.

**Brown, J.F.; Wardlow, B.D.; Tadesse, T.; Hayes, M.J.; Reed, B.C. 2008.** The Vegetation Drought Response Index (VegDRI): a new integrated approach for monitoring drought stress in vegetation. GIScience and Remote Sensing. 45: 16–46.

**Browning, D.M.; Karl, J.W.; Moran, D.; Richardson, A.D.; Tweedie, C.E. 2017**. Phenocams bridge the gap between field and satellite observations in an arid grassland ecosystem. Remote Sensing. 2017(9): 1071–1092.

**Browning, D.M.; Peters, D.C.; Steele, C.M.; Rango, A. 2010**. Field validation of biomass retrieved from Landsat for rangeland assessment and monitoring. International Geoscience and Remote Sensing Symposium Proceedings. 4 p. http://jornada.nmsu.edu/files/bibliography/10-028.pdf. (4 October 2017).

**Casady, G.M.; van Leeuwen, W.J.D.; Reed, B.C. 2013**. Estimating winter annual biomass in the Sonoran and Mojave Deserts with satellite- and ground-based observations. Remote Sensing. 5: 909–926.

**Channan, S.; Collins, K.; Emanuel, W. 2014**. Global mosaics of the standard MODIS land cover type data. College Park, MD: University of Maryland; Richland, WA: Pacific Northwest National Laboratory. http://glcf.umd.edu/data/lc/. (15 October 2017).

**Chapin, F.S. III; Matson, P.A.; Vitousek, P. 2011.** Principals of terrestrial ecosystem ecology. New York: Springer-Verlag. 529 p.

**Chastain, R.A.; Fisk, H.; Ellenwood, J.R.; Sapio, F.J.; Ruefenacht, B.; Finco, M.V.; Thomas, V. 2015.** Near-real time delivery of MODIS-based information on forest disturbances. In: Lippitt, C.; Stow, D.; Coulter, L., eds. Time sensitive remote sensing. New York: Springer-Verlag: 147–164.

**Cohen, W.B.; Yang, Z.; Kennedy, R. 2010.** Detecting trends in forest disturbance and recovery using yearly Landsat time series: 2. Timesynch—tools for calibration and validation. Remote Sensing of Environment. 114(12): 2911–2924.

**Dye, D.G.; Middleton, B.R.; Vogel, J.M.; Wu, Z.; Velasco, M.G. 2016.** Exploiting differential vegetation phenology for satellite-based mapping of semiarid grass vegetation in the southwestern United States and northern Mexico. Remote Sensing. 8(11): 889.

**Enquist, C.A.; Kellermann, J.L.; Gerst, K.L.; Miller-Rushing, A.J. 2014.** Phenology research for natural resource management in the United States. International Journal of Biometeorology. 58(4): 579–589.

**Esri. 2018.** ArcGIS Online. https://www.esri.com/en-us/arcgis/products/arcgis-online/overview. (1 March 2018).

**Filippa, G.; Cremonese, E.; Migliavacca, M.; Galvagno, M.; Sonnentag, O.; Humphreys, E.; Hufkens, K.; Ryu, Y.; Verfaillie, J.; Morra di Cella, U.; Richardson, A.D. 2018**. NDVI derived from near-infrared-enabled digital cameras: applicability across different plant functional types. Agricultural and Forest Meteorology. 249: 275–285.

**Gamon, J.A.; Huemmrich, K.F.; Wong, C.Y.S.; Ensminger, I.; Garrity, S.; Hollinger, D.Y.; Noormets, A.; Peñuelas, J. 2016.** A remotely sensed pigment index reveals photosynthetic phenology in evergreen conifers. Proceedings of the National Academy of Sciences of the United States of America. 113(46): 13087–13092.

**Gillham, J.; Mellin, T. 2004**. Monitoring rangeland trends using remote sensing. In: Proceedings of the 2004 10th biennial Forest Service remote sensing applications conference. [CD-ROM]. Salt Lake City, UT: U.S. Department of Agriculture, Forest Service, Remote Sensing Applications Center.

**Gorelick, N.; Hancher, M.; Dixon, M.; Ilyushchenko, S.; Thau, D.; Moore, R. 2017.** Google Earth Engine: planetary-scale geospatial analysis for everyone. Remote Sensing of Environment. 202: 18–27.

**Grace, J.; Nichol, C.; Disney, M.; Lewis, P.; Quaife, T.; Bowyer, P. 2007**. Can we measure terrestrial photosynthesis from space directly, using spectral reflectance and fluorescence? Global Change Biology. 13: 1484−1497.

**Hargrove, W.W.; Spruce, J.P.; Gasser, G.E.; Hoffman, F.M. 2009.** Toward a national early warning system for forest disturbances using remotely sensed canopy phenology. Photogrammetric Engineering and Remote Sensing. 75: 1150–1156.

**Helman, D. 2018.** Land surface phenology: What do we really ‘see’ from space? Science of the Total Environment. 618: 665–673.

**Huete, A.R.; Didan, K.; Miura, T.; Rodriguez, E.P.; Gao, X.; Ferreira, L.G. 2002.** Overview of the radiometric and biophysical performance of the MODIS vegetation indices. Remote Sensing of Environment. 83: 195–213.

**Huete, A.R.; Justice, C.; Liu, H. 1994.** Development of vegetation and soil indices for MODIS-EOS. Remote Sensing of Environment. 49(3): 224–234.

**Huete, A.R.; Liu, H.Q.; Batchily, K.; van Leeuwen, W. 1997.** A comparison of vegetation indices over a global set of TM images for EOS-MODIS. Remote Sensing of Environment. 59(3): 440–451.

**Huete, A.R.; Jackson, R.D. 1987.** Suitability of spectral indices for evaluating vegetation characteristics on arid rangelands. Remote Sensing of Environment. 23(2): 213–218.

**Inoue, T.; Nagai, S.; Kobayashi, H.; Koizumi, H. 2015**. Utilization of ground-based digital photography for the evaluation of seasonal changes in the aboveground green biomass and foliage phenology in a grassland ecosystem. Ecological Informatics. 25: 1–9.

**Jenkerson, C.; Maiersperger, T.; Schmidt, G. 2010**. eMODIS: a user-friendly data source. Open-File Report 2010–1055. Reston, VA: U.S. Department of the Interior, Geological Survey. 10 p.

**Jönsson, A.M.; Eklundh, L.; Hellström, M.; Bärring, L.; Jönsson, P. 2010**. Annual changes in MODIS vegetation indices of Swedish coniferous forests in relation to snow dynamics and tree phenology. Remote Sensing of Environment. 114: 2719–2730.

**Justice, C.O.; Townsend, J.R.G.; Vermote, E.F.; Masuoka, E.; Wolfe, R.E.; Saleous, N.; Roy, E.P.; Morisette, J.T. 2002.** An overview of MODIS lLand data processing and product status. Remote Sensing of Environment. 83: 3–15.

**Keenan, T.F.; Darby, B.; Felts, E.; Sonnentag, O.; Friedl, M.A.; Hufkens, K.; O'Keefe, J.; Klosterman, S.; Munger, J.W.; Richardson, A.D. 2014.** Tracking forest phenology and seasonal physiology using digital repeat photography: a critical assessment. Ecological Applications. 24(6): 1478–1489.

**Kurc, S.A.; Benton, L.M. 2009.** Digital image derived greeness links deep soil moisture to carbon uptake in a creosotebush-dominated shrubland. Journal of Arid Environments. 74(5): 585–594.

**Liu, Z.; Hu, H.; Yu, H.; Yang, X.; Yang, H.; Ruan, C.; Wang, Y.; Tang, J. 2015.** Relationship between leaf physiographic traits and canopy color indices during the leaf expansion period in an oak forest. Ecosphere. 6(12): 1–9.

**Malingreau, J.-P. 1986**. Global vegetation in dynamics, satellite observations over Asia. International Journal of Remote Sensing. 7(9): 1121–1146.

**Marshall, K. 1995**. *Larrea tridentata*. In: Fire Effects Information System. Missoula, MT: U.S. Department of Agriculture, Forest Service, Rocky Mountain Research Station, Fire Sciences Laboratory. https://www.feis-crs.org/feis/. (2 March 2018).

**Meier, G.A.; Brown, J.F. 2014**. Remote sensing of land surface phenology. Fact Sheet 2014-3052. Reston, VA: U.S. Department of the Interior, Geological Survey. 2 p. https://pubs.er.usgs.gov/publication/fs20143052. (30 April 2019).

**Nash, M.S.; Bradford, D.F.; Wickham, J.D.; Wade, T.G. 2014**. Detecting change in landscape greenness over large areas: an example for New Mexico, USA. Remote Sensing of Environment. 150(2014): 152–162.

**National Aeronautics and Space Administration, Goddard Space Flight Center [NASA GSFC]. 2010**. What is a product collection? https://landweb.modaps.eosdis.nasa.gov/cgi-bin/QA_WWW/newPage.cgi?fileName=collection. (3 October 2017).

**National Aeronautics and Space Administration, Goddard Space Flight Center [NASA GSFC]. 2017**. MODIS news. https://modis-land.gsfc.nasa.gov/news.html. (25 July 2017).

**Olofsson, P.; Lagergren, F.; Lindroth, A.; Lindstrom, J.; Klemedtsson, L.; Kutsch, W. 2008.** Towards operational remote sensing of forest carbon balance across Northern Europe. Biogeosciences. 5(3): 817−832.

**Parmesan, C. 2007**. Influences of species, latitudes and methodologies on estimates of phenological response to global warming. Global Change Biology 13(9): 1860–1872.

**Pavlik, B.; Muick, P.; Johnson, S.; Popper, M. 1991**. Oaks of California. Los Olivos, CA: Cachuma Press. 184 p.

**Peterson, D.L.; Millar, C.I.; Joyce, L.A.; Furniss, M.J.; Halofsky, J.E.; Neilson, R.P.; Morelli, T.L. 2011**. Responding to climate change on national forests: a guidebook for developing adaptation options. Gen. Tech. Rep. PNW-GTR-855. Portland, OR: U.S. Department of Agriculture, Forest Service, Pacific Northwest Research Station. 109 p.

**Pettorelli, N. 2013**. The normalized difference vegetation index. Oxford, United Kingdom: Oxford University Press. 224 p.

**Piyoosh, A.T.; Ghosh, S.K. 2017.** Development of a modified bare soil and urban index for Landsat 8 satellite data. Geocarta International. 33(4): 1–20.

**Rautiainen, M.; Lukeš, P.; Homolová, L.; Hovi, A.; Pisek, J.; Mõttus, M. 2018.** Spectral properties of coniferous forests: a review of in situ and laboratory measurements. Remote Sensing. 10(2): 207.

**Reed, B.C.; Brown, J.F.; VanderZee, D.; Loveland, T.R.; Merchant, J.W.; Ohlen, D.O. 1994**. Measuring phenological variability from satellite imagery. Journal of Vegetation Science. 5(5): 703–714.

**Reeves, M.C.; Moreno, A.L.; Bagne, K.E.; Running, S.W. 2014**. Estimating climate change effects on net primary production of rangelands in the United States. Climate Change. 126: 429–442.

**Richardson, A.D.; Jenkins, J.P.; Braswell, B.H.; Hollinger, D.Y.; Ollinger, S.V.; Smith, M.-L. 2007.** Use of digital webcam imagers to track spring green-up in a deciduous broadleaf forest. Oecologia. 152: 323–354.

**Robinson, N.P.; Allred, B.W.; Jones, M.O.; Moreno, A.; Kimball, J.S.; Naugle, D.E.; Erickson, T.A.; Richardson, A.D. 2017.** A dynamic Landsat derived normalized difference vegetation index (NDVI) product for the conterminous United States. Remote Sensing. 2017(9): 863.

**Rossini, M.; Cogliati, S.; Meroni, M.; Migliavacca, M.; Galvagno, M.; Busetto, L.; Cremonese, E.; Julitta, T.; Siniscalco, C.; Morradi Cella, U. 2012.** Remote sensing-based estimation of gross primary production in a subalpine grassland. Biogeosciences. 9(7): 2565–2584.

**Rouse, J.W.; Haas, R.H.; Scheel, J.A.; Deering, D.W. 1974**. Monitoring vegetation systems in the Great Plains with ERTS. Proceedings, 3rd Earth Resources Technology Satellite-1 Symposium. 1: 48–62. https://ntrs.nasa.gov/archive/nasa/casi.ntrs.nasa.gov/19740022614.pdf. (25 July 2017).

**Ryu, Y.; Lee, G.; Jeon, S.; Song, Y.; Kimm, H. 2014**. Monitoring multi-layer canopy spring phenology of temperate deciduous and evergreen forest using low-cost spectral sensors. Remote Sensing of Environment. 149: 277–238.

**Sankey, T.; Weber, K. 2009**. Rangeland assessments using remote sensing: Is NDVI useful? In: Weber, K.T.; Davis, K., eds. Final report: comparing effects of management practices on rangeland health with geospatial technologies: 113–122.

**Schwartz, M.D.; Betancourt, J.L.; Weltzin, J.F. 2012.** From Caprio's lilacs to the USA Phenology Network. Frontiers in Ecology and the Environment. 10(6): 324–327.

**Schwartz, M.D.; Reed, B.C.; White, M.A. 2002.** Assessing satellite-derived start of season measures in the conterminous USA. International Journal of Climatology. 22: 1793–1805.

**Seastedt, T.R.; Ramundo, R.A. 1990.** The influence of fire on belowground processes. In: Collins, S.L.; Wallace, L.L., eds. Fire in North American tallgrass prairies. Norman, OK: University of Oklahoma Press: 99–117.

**Shouse, M.K.; Cox, D.A. 2013.** USGS science at work in the San Francisco Bay and Sacramento–San Joaquin delta estuary. Fact Sheet 2013–3037. Sacramento, CA: U.S. Department of the Interior, Geological Survey. 6 p. https://pubs.usgs.gov/fs/2013/3037/pdf/fs2013-3037.pdf. (15 January 2018).

**Sonnetag, O.; Hufkens, K.; Teshera-Sterne, C.; Young, A.M.; Friedl, M.; Braswell, B.H.; Milliman, T.; O'Keefe, J.; Richardson, A.D. 2012.** Digital repeat photography for phenological research in forest ecosystems. Agricultural and Forest Meterology. 152: 159–177.

**Steinberg, P. 2001**. *Prosopis glandulosa*. In: Fire Effects Information System, USDA Forest Service, Rocky Mountain Research Station, Fire Sciences Laboratory. https://www.feis-crs.org/feis/. (2 March 2018).

**Swets, D.L.; Reed, B.C.; Rowland, J.; Marko, S.E. 1999**. A weighted least-squares approach to temporal NDVI smoothing. In: From image to imagination: 1999 ASPRS annual conference. Bethesda, MD: American Society for Photogrammetry and Remote Sensing. [Page range unknown].

**Tedrow, L.; Weber, K. 2011.** NDVI changes over a calendar year in the rangelands of southeast Idaho. In: Weber, K., Davis, K., eds. Final report: assessing post-fire recovery of sagebrush-steppe rangelands in southeastern Idaho. Pocatello, ID: Idaho State University: 105–116.

**Tirmenstein, D. 1999**. *Artemisia tridentata* subsp. *tridentata*. In: Fire Effects Information System. Missoula, MT: U.S. Department of Agriculture Forest Service, Rocky Mountain Research Station, Fire Sciences Laboratory. https://www.feis-crs.org/feis/. (2 March 2018).

**Toomey, M.; Friedl, M.A.; Frolking, S.; Hufkens, K.; Klosterman, S.; Sonnentag, O.; Baldocchi, D.D.; Bernacchi, C.J.; Biraud, S.C.; Bohrer, G.; Brzostek, E.; Burns, S.P.; Coursolle, C.; Hollinger, D.Y.; Margolis, H.A.; McCaughey, H.; Monson, R.K.; Munger, J.W.; Pallardy, S.; Phillips, R.P.; Torn, M.S.; Wharton, S.; Zeri M.; Richardson, A.D. 2015**. Greenness indices from digital cameras predict the timing and seasonal dynamics of canopy scale photosynthesis. Ecological Applications. 25(1): 99–115.

**Ulsig, L.; Nichol, C.J.; Huemmrich, K.F.; Landis, D.R.; Middleton, E.M.; Lyapustin, A.I.; Mammarella, I.; Levula, J.; Porcar-Castell, A. 2017.** Detecting inter-annual variations in the phenology of evergreen conifers using long-term MODIS Vegetation Index Time Series. Remote Sensing. 9(1): 49.

**U.S. Department of Agriculture, Forest Service [USDA FS]. 2018**. Natural Resource Manager (NRM) Forest Service Activity Tracking System (FACTS) database. https://www.fs.fed.us/nrm/. (19 April 2019).

**U.S. Department of Commerce, National Oceanic and Atmospheric Administration [USDC NOAA]. 2018**. Record of climatological observations, Squaw Butte Northern Great Basin Experimental Range. Washington, DC: National Centers for Environmental Information. https://www.ncdc.noaa.gov/cdo-web/datasets/GHCND/stations/GHCND:USC00358029/detail. (10 February 2018).

**U.S. Department of the Interior, Geological Survey [USDI GS]. 2017a.** C6 Aqua Western U.S. 250 m eMODIS remote sensing phenology data. https://phenology.cr.usgs.gov/get_data_Aqua_C6_250w.php. (30 August 2019).

**U.S. Department of the Interior, Geological Survey [USDI GS]. 2017b.** EROS Moderate Resolution Imaging Spectroradiometer (eMODIS). https://www.usgs.gov/centers/eros/science/usgs-eros-archive-vegetation-monitoring-eros-moderate-resolution-imaging?qt-science_center_objects=0#qt-science_center_objects. (20 December 2017).

**U.S. Department of the Interior, Geological Survey [USDI GS]. 2017c.** NDVI, the foundation for remote sensing phenology. https://www.usgs.gov/land-resources/eros/phenology/science/ndvi-foundation-remote-sensing-phenology?qt-science_center_objects=0#qt-science_center_objects. (19 April 2019).

**Wardlow, B.D.; Tadesse, T.; Brown, J.F.; Callahan, K.; Swain, S.; Hunt, E. 2012.** Vegetation drought response index: an integration of satellite, climate, and biophysical data. In: Wardlow, Brian D.; Anderson, M.C.; Verdin, P., eds. Remote sensing of drought: innovative monitoring approaches. Lincoln, NE: University of Nebraska-Lincoln, School of Natural Resources, National Drought Mitigation Center: 51–74. Chapter 3.

**Weier, J.; Herring, D. 2000.** Measuring vegetation (NDVI & EVI). Washington, DC: National Aeronautics and Space Administration, Earth Observing System Project Science Office, Earth Observatory. https://earthobservatory.nasa.gov/Features/MeasuringVegetation/. (11 September 2017).

**White, M.; De Beurs, K.; Didan, K.; Inouye, D.; Richardson, A.; Jensen, O.; O'Keefe, J.; Zhang, G. 2009.** Intercomparison, interpretation and assessment of spring phenology in North America estimated from remote sensing for 1982–2006. Global Change Biology. 15: 2335–2359.

**White, M.; Nemani, R. 2006**. Real-time monitoring and short-term forecasting of land surface phenology. Remote Sensing of Environment. 104: 43–46.

# Appendix 1: PhenoCam Graphs, Scatterplots, and Images

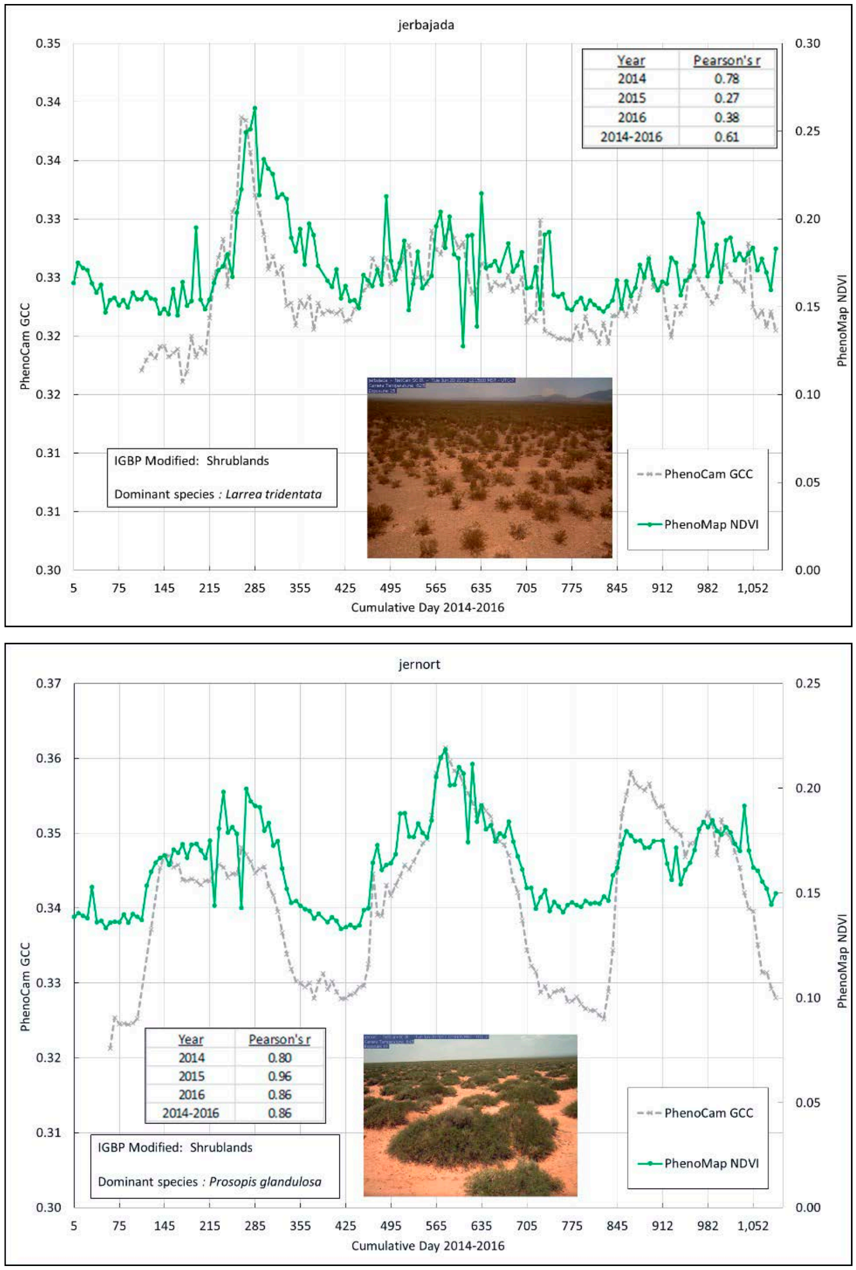


Figure 15— Line graph of the PhenoCam green chromatic coordinate ($gcc_{per90}$) and PhenoMap eMODIS NDVI weekly values 2014–2016 for the jerbajada and jernort sites. These sites are both located on the Jornada Experimental Range in New Mexico, are approximately 15 km apart and are in the Chihuahuan Deserts level 3 ecoregion. The difference in phenological patterns in both NDVI and $gcc_{per90}$ is primarily because of the different adaptations to aridity by the dominant species on each site.

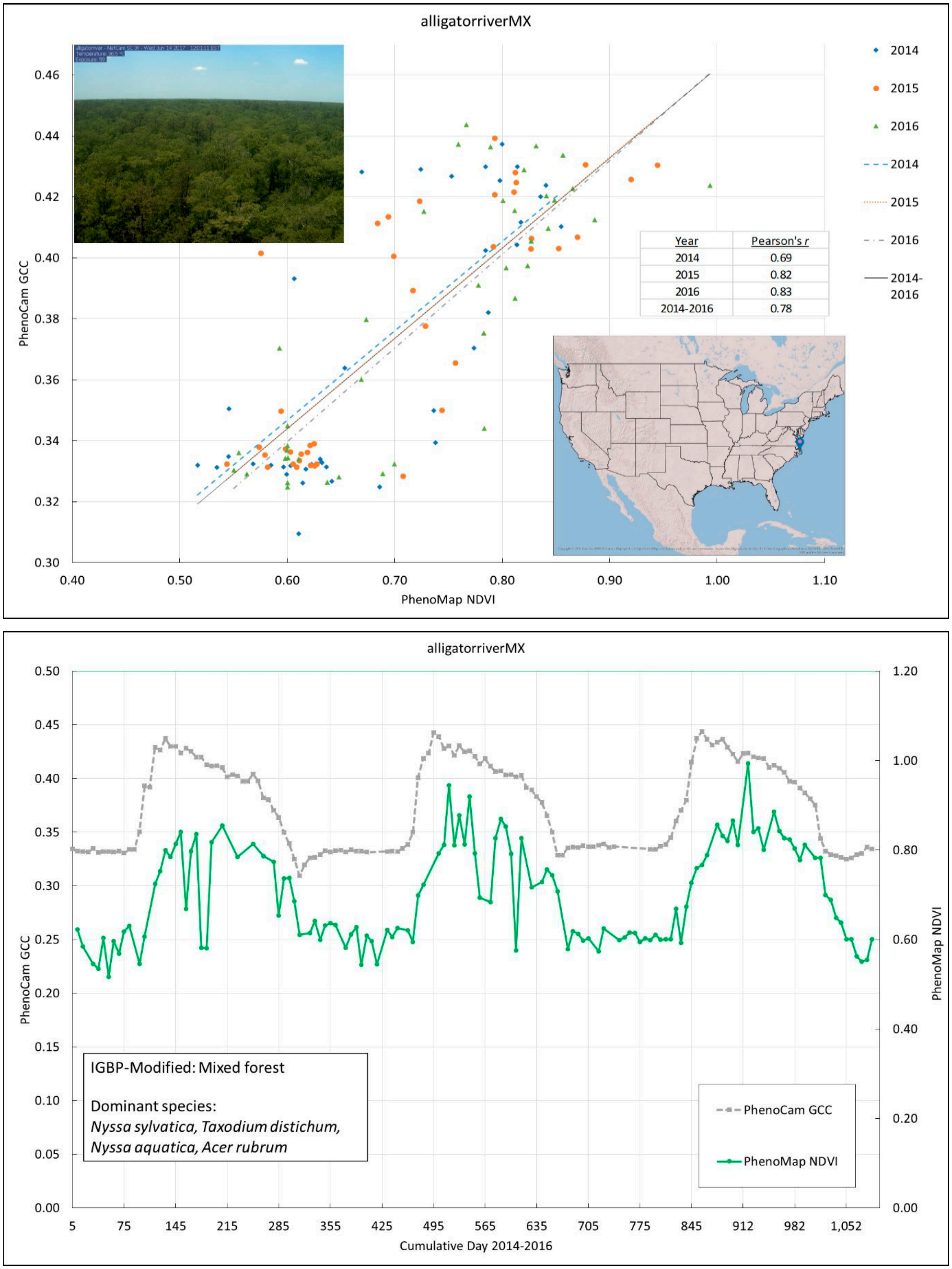


Figure 16—(A) Line graph and (B) scatterplot of the PhenoCam green chromatic coordinate ($gcc_{per90}$) and PhenoMap eMODIS NDVI weekly values 2014–2016 for the alligatorriverMX site. Inset graphics in the line graph show a representative PhenoCam image and a map showing the location of the site.

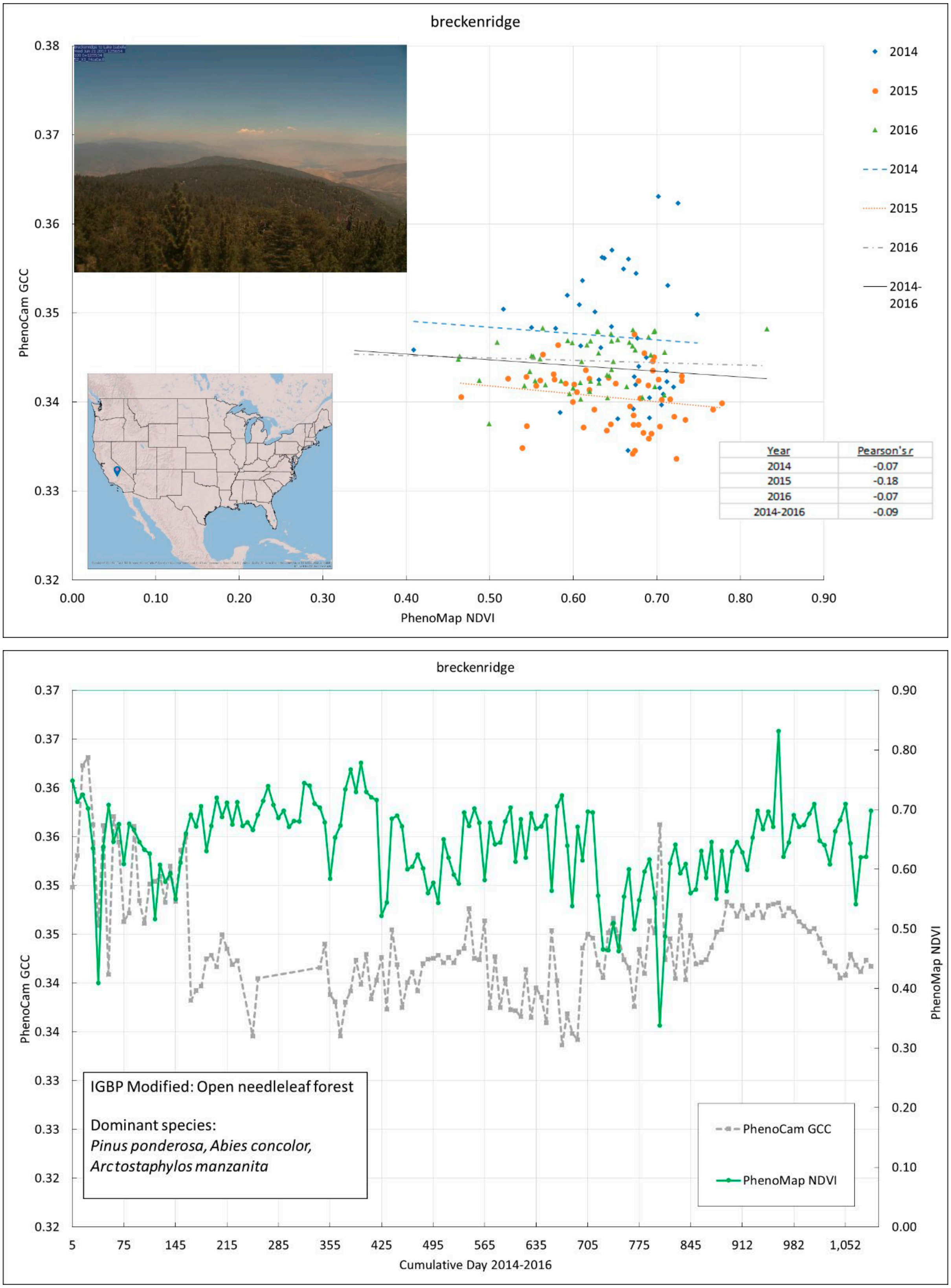


Figure 17—(A) Line graph and (B) scatterplot of the PhenoCam green chromatic coordinate ($gcc_{per90}$) and PhenoMap eMODIS NDVI weekly values 2014–2016 for the breckenridge site. Inset graphics in the line graph show a representative PhenoCam image and a map showing the location of the site.

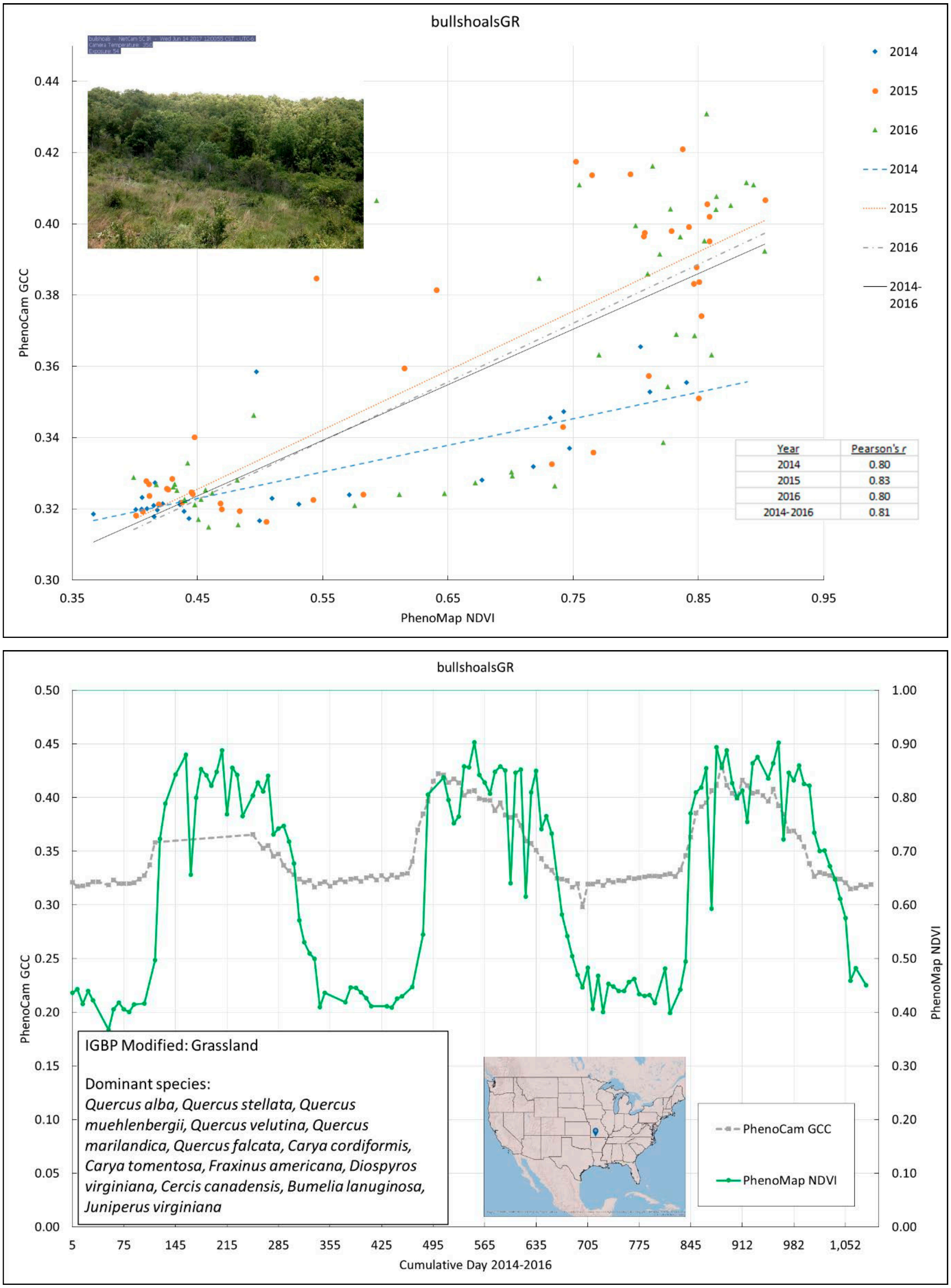


Figure 18—(A) Line graph and (B) scatterplot of the PhenoCam green chromatic coordinate ($gcc_{per90}$) and PhenoMap eMODIS NDVI weekly values 2014–2016 for the bullshoalsGR site. Inset graphics in the line graph show a representative PhenoCam image and a map showing the location of the site.

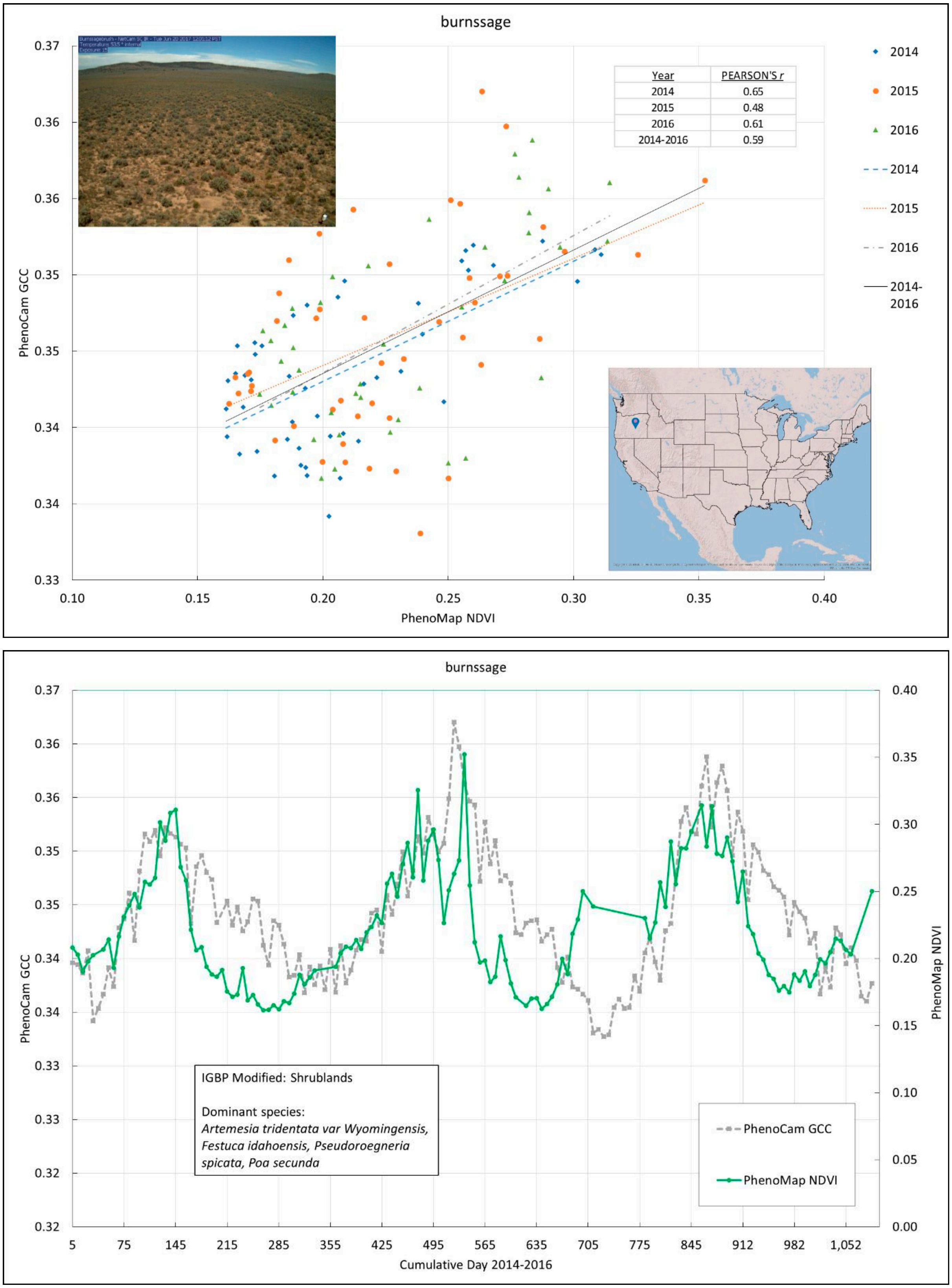


Figure 19—(A) Line graph and (B) scatterplot of the PhenoCam green chromatic coordinate ($gcc_{per90}$) and PhenoMap eMODIS NDVI weekly values 2014–2016 for the burnssage site. Inset graphics in the line graph show a representative PhenoCam image and a map showing the location of the site.

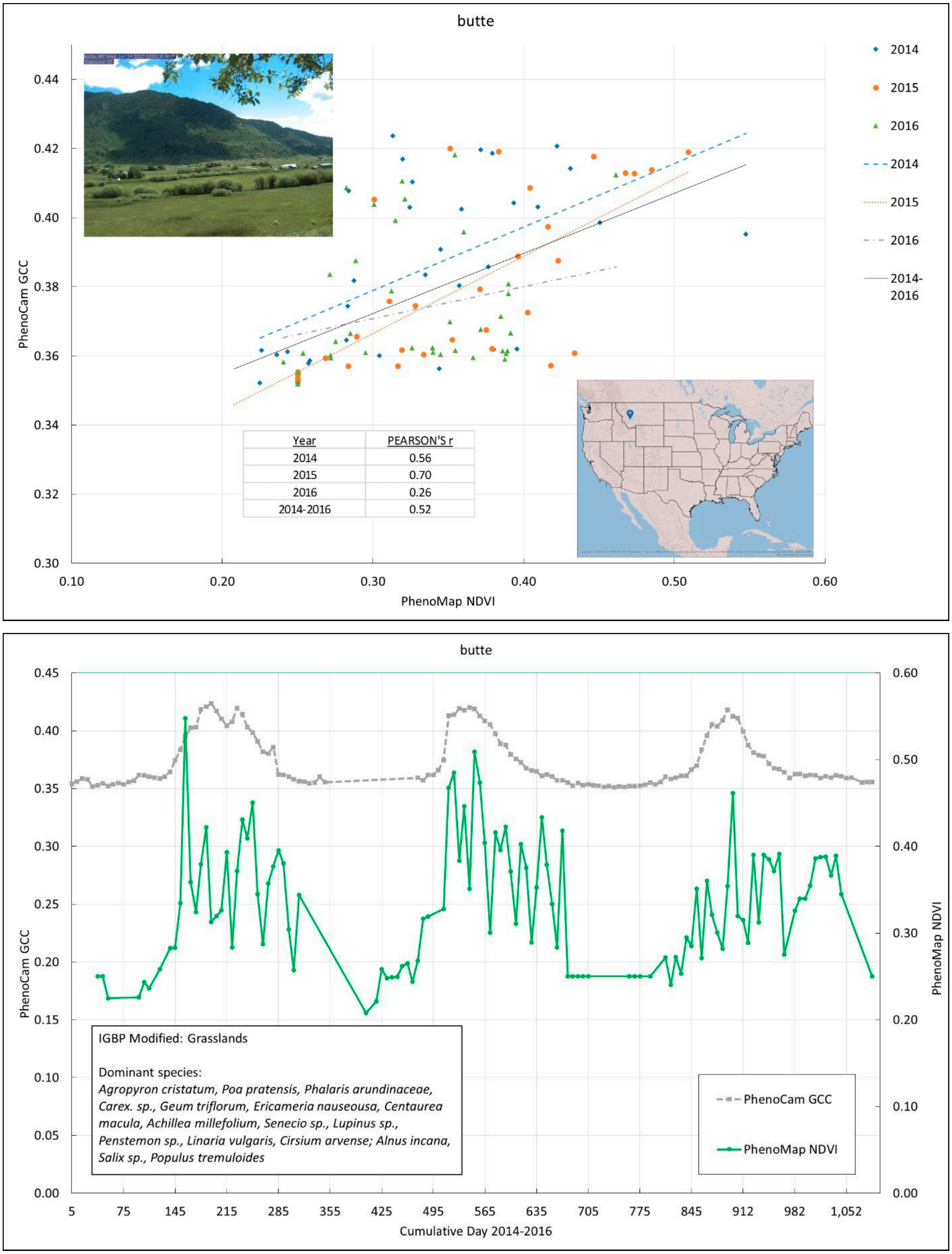


Figure 20—(A) Line graph and (B) scatterplot of the PhenoCam green chromatic coordinate ($gcc_{per90}$) and PhenoMap eMODIS NDVI weekly values 2014–2016 for the butte site. Inset graphics in the line graph show a representative PhenoCam image and a map showing the location of the site.

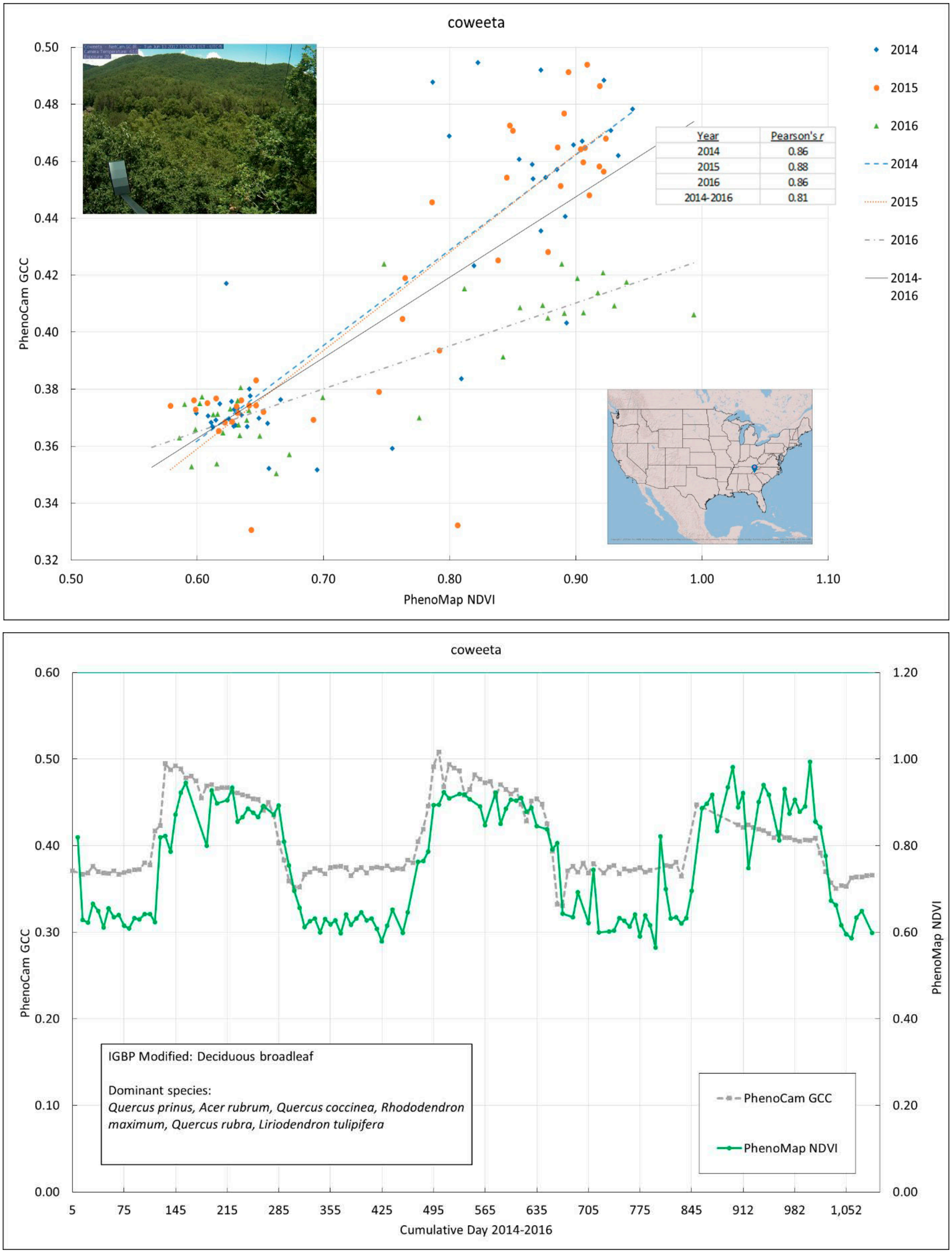


Figure 21—(A) Line graph and (B) scatterplot of the PhenoCam green chromatic coordinate ($gcc_{per90}$) and PhenoMap eMODIS NDVI weekly values 2014–2016 for the coweeta site. Inset graphics in the line graph show a representative PhenoCam image and a map showing the location of the site.

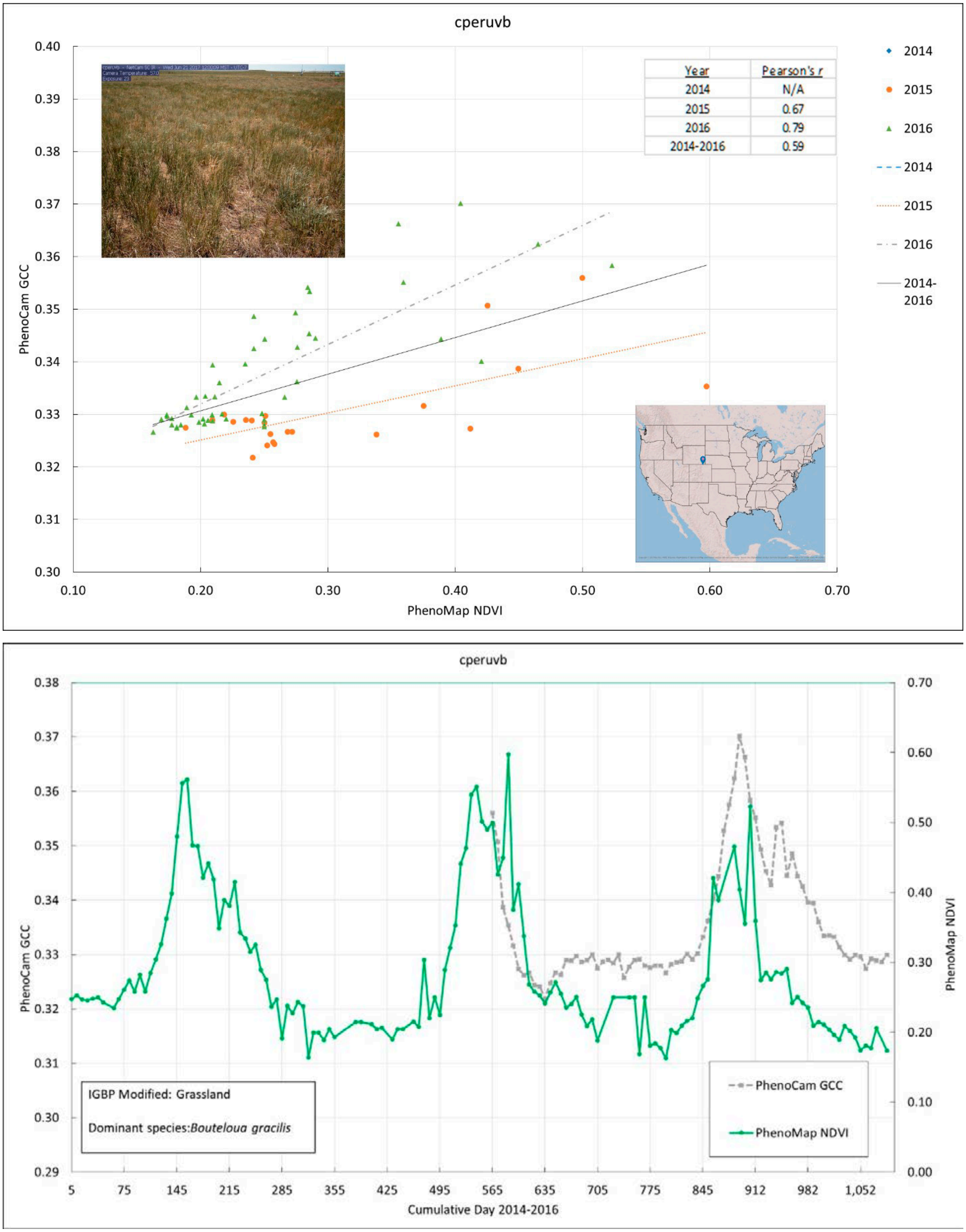


Figure 22—(A) Line graph and (B) scatterplot of the PhenoCam green chromatic coordinate ($gcc_{per90}$) and PhenoMap eMODIS NDVI weekly values 2014–2016 for the cperuvb site. Inset graphics in the line graph show a representative PhenoCam image and a map showing the location of the site.

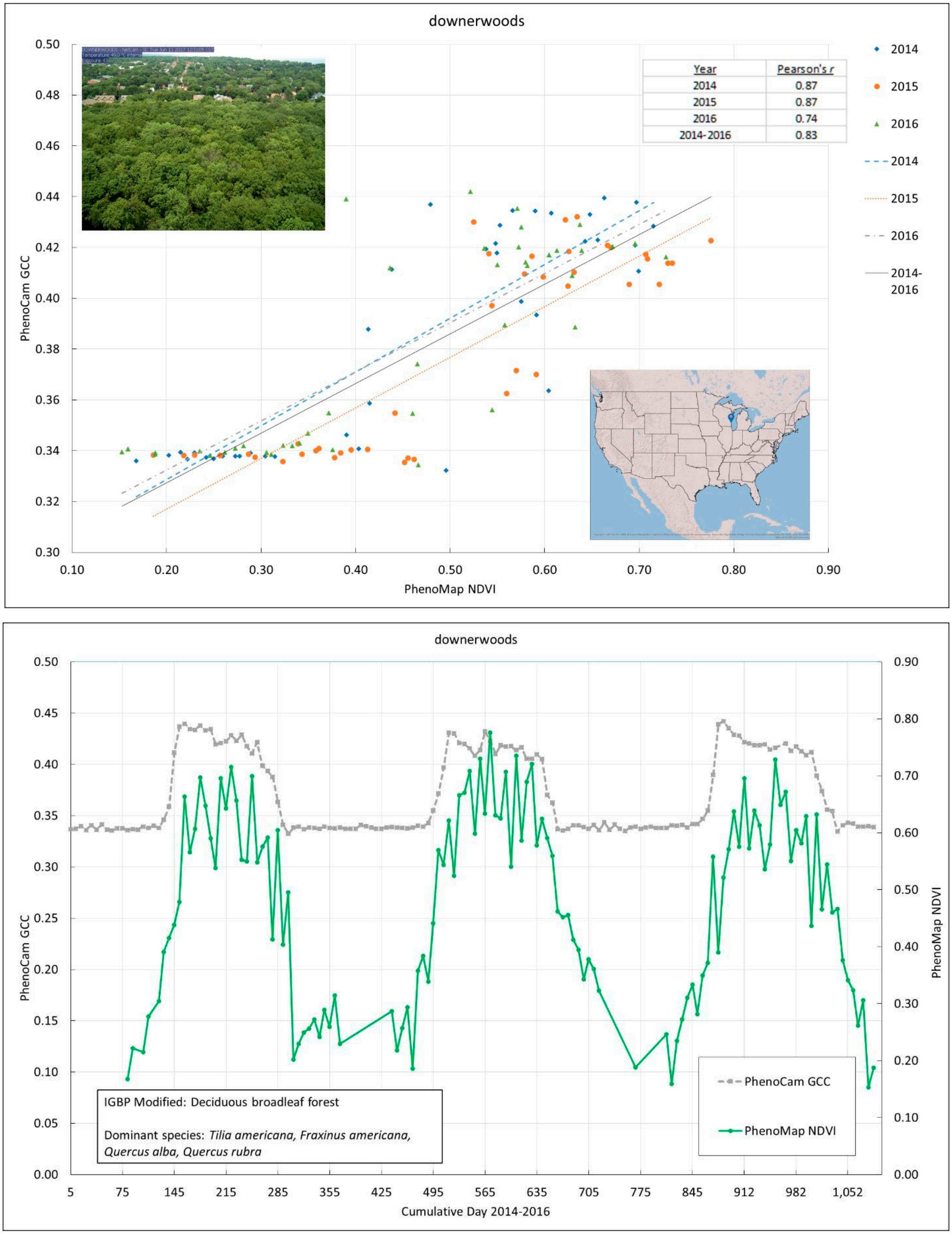


Figure 23—(A) Line graph and (B) scatterplot of the PhenoCam green chromatic coordinate ($gcc_{per90}$) and PhenoMap eMODIS NDVI weekly values 2014–2016 for the downerwoods site. Inset graphics in the line graph show a representative PhenoCam image and a map showing the location of the site.

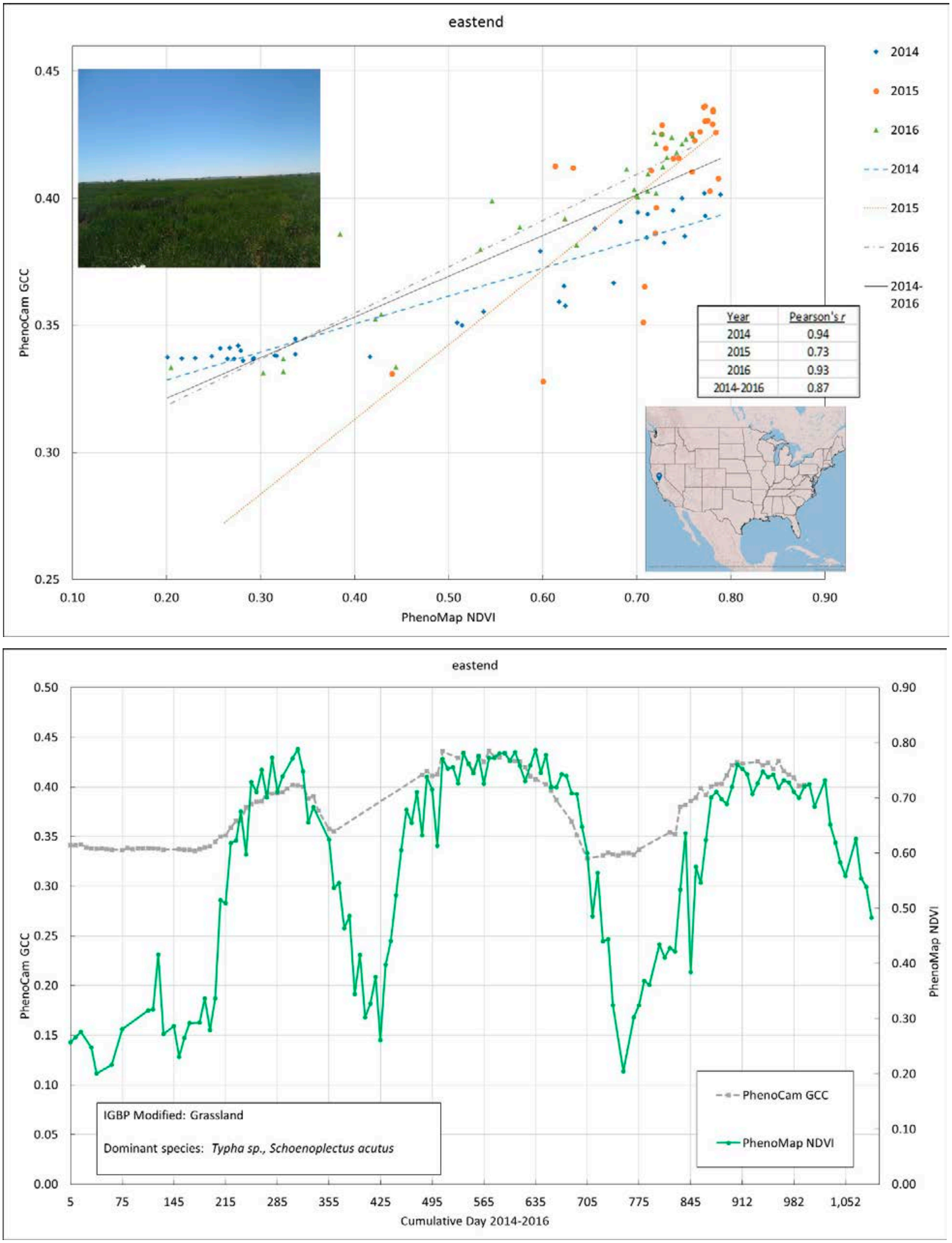


Figure 24—(A) Line graph and (B) scatterplot of the PhenoCam green chromatic coordinate ($gcc_{per90}$) and PhenoMap eMODIS NDVI weekly values 2014–2016 for the eastend site. Inset graphics in the line graph show a representative PhenoCam image and a map showing the location of the site.

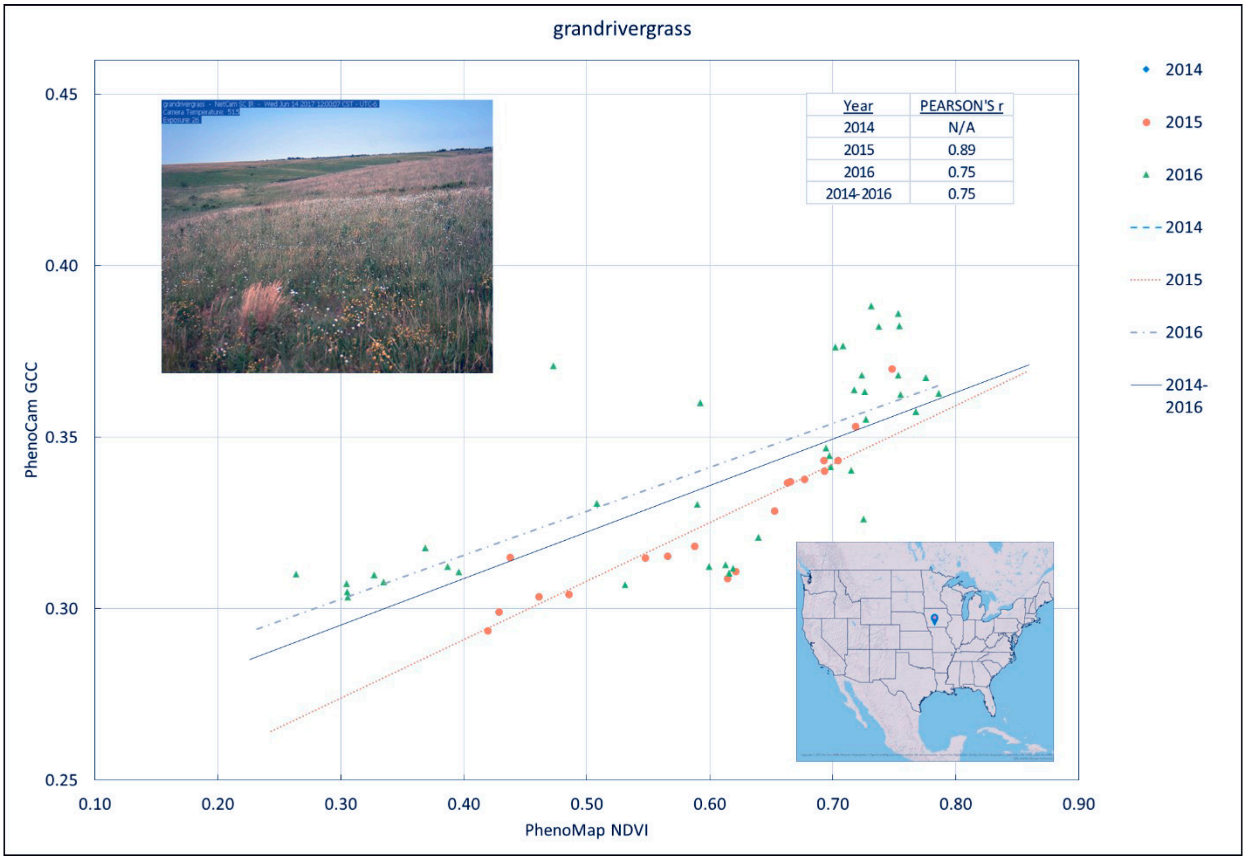


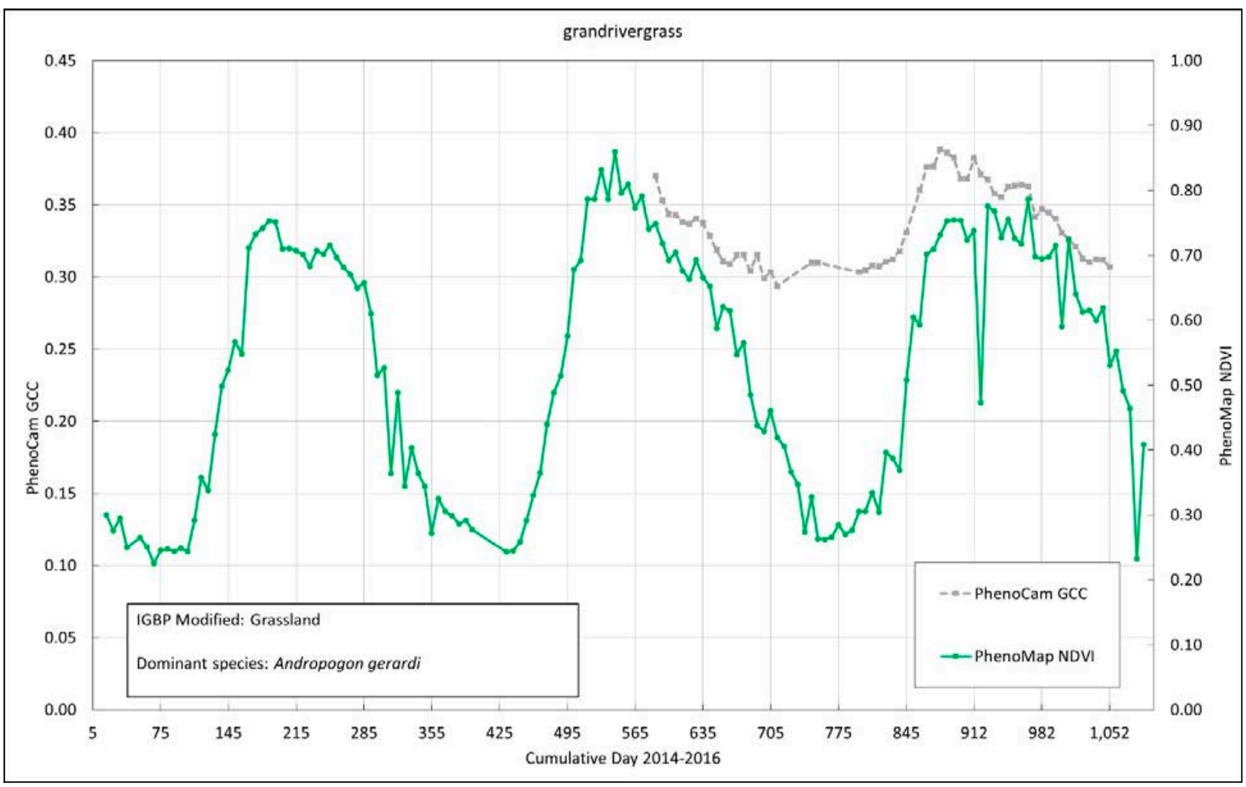


Figure 25—(A) Line graph and (B) scatterplot of the PhenoCam green chromatic coordinate ($gcc_{per90}$) and PhenoMap eMODIS NDVI weekly values 2014–2016 for the grandrivergrass site. Inset graphics in the line graph show a representative PhenoCam image and a map showing the location of the site.

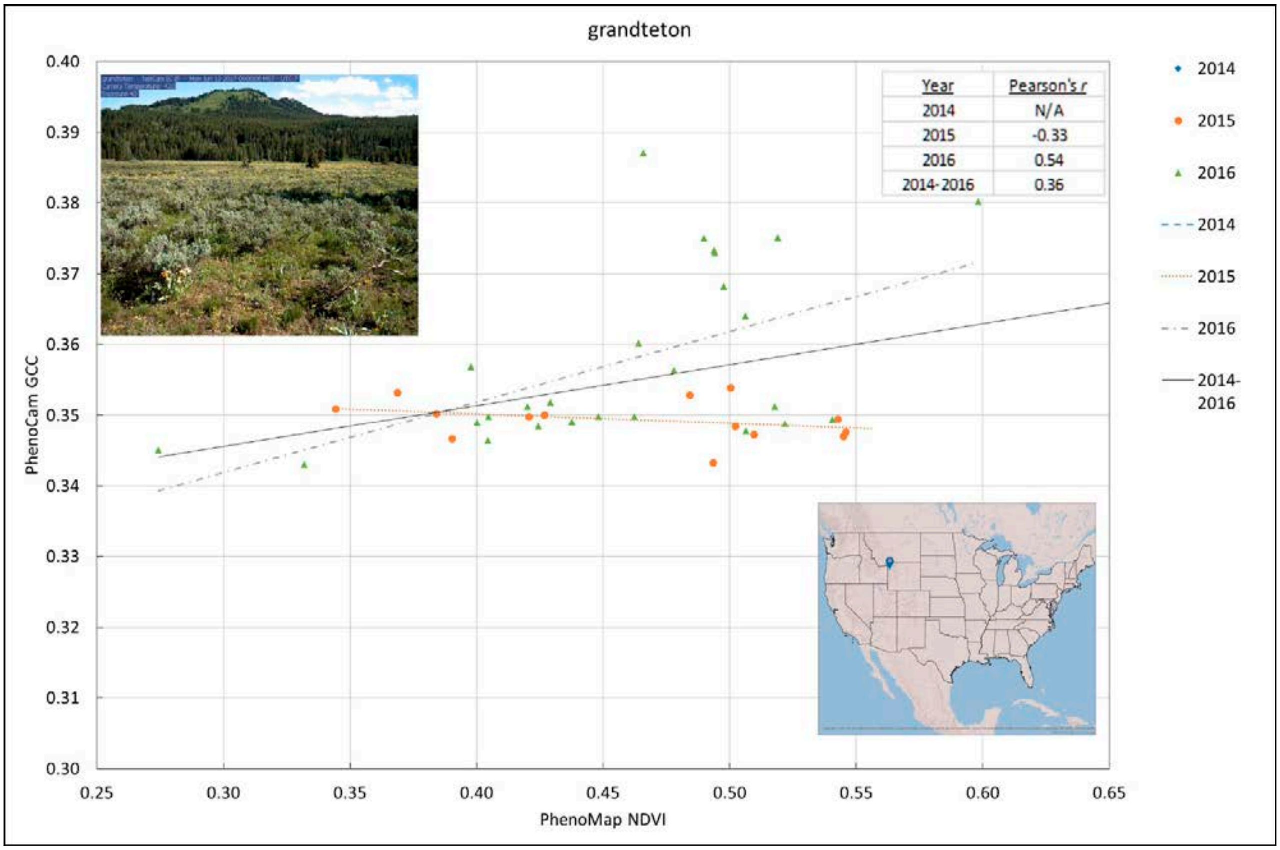


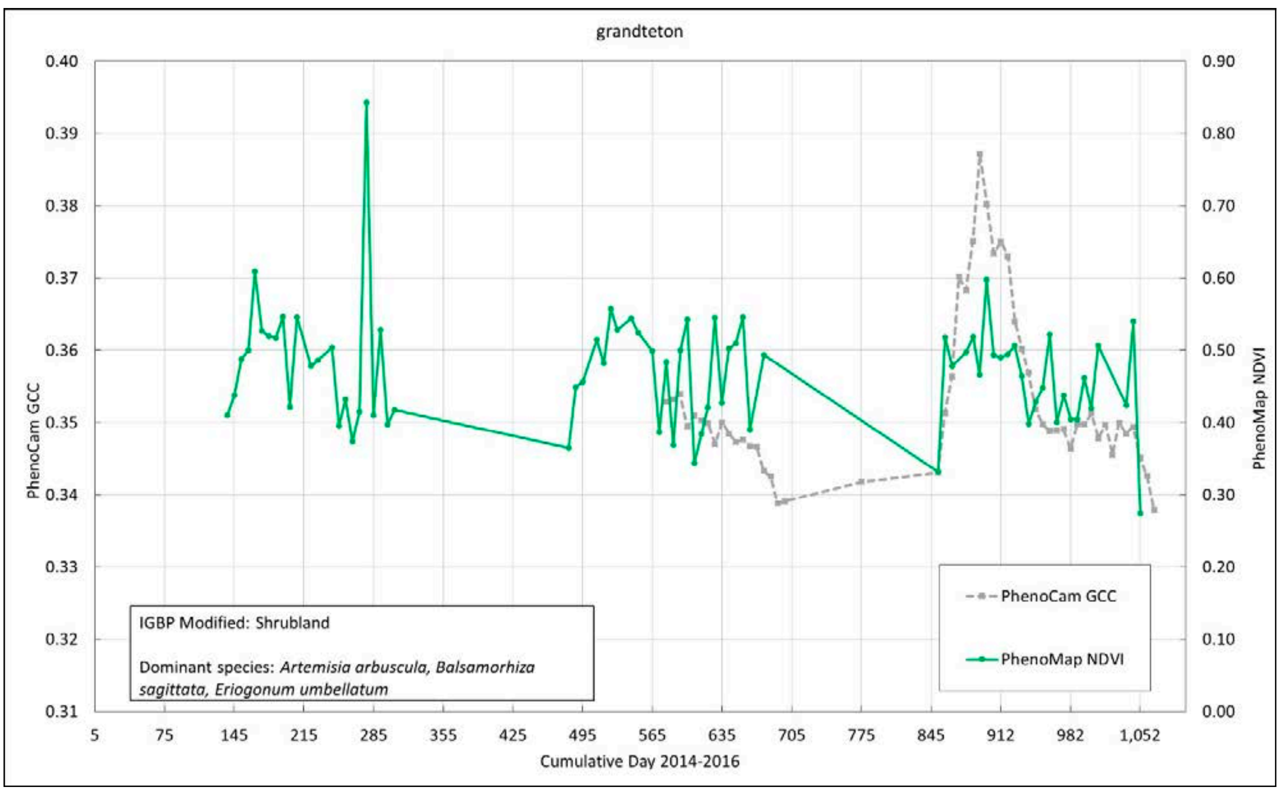


Figure 26—(A) Line graph and (B) scatterplot of the PhenoCam green chromatic coordinate ($gcc_{per90}$) and PhenoMap eMODIS NDVI weekly values 2014–2016 for the grandteton site. Inset graphics in the line graph show a representative PhenoCam image and a map showing the location of the site.

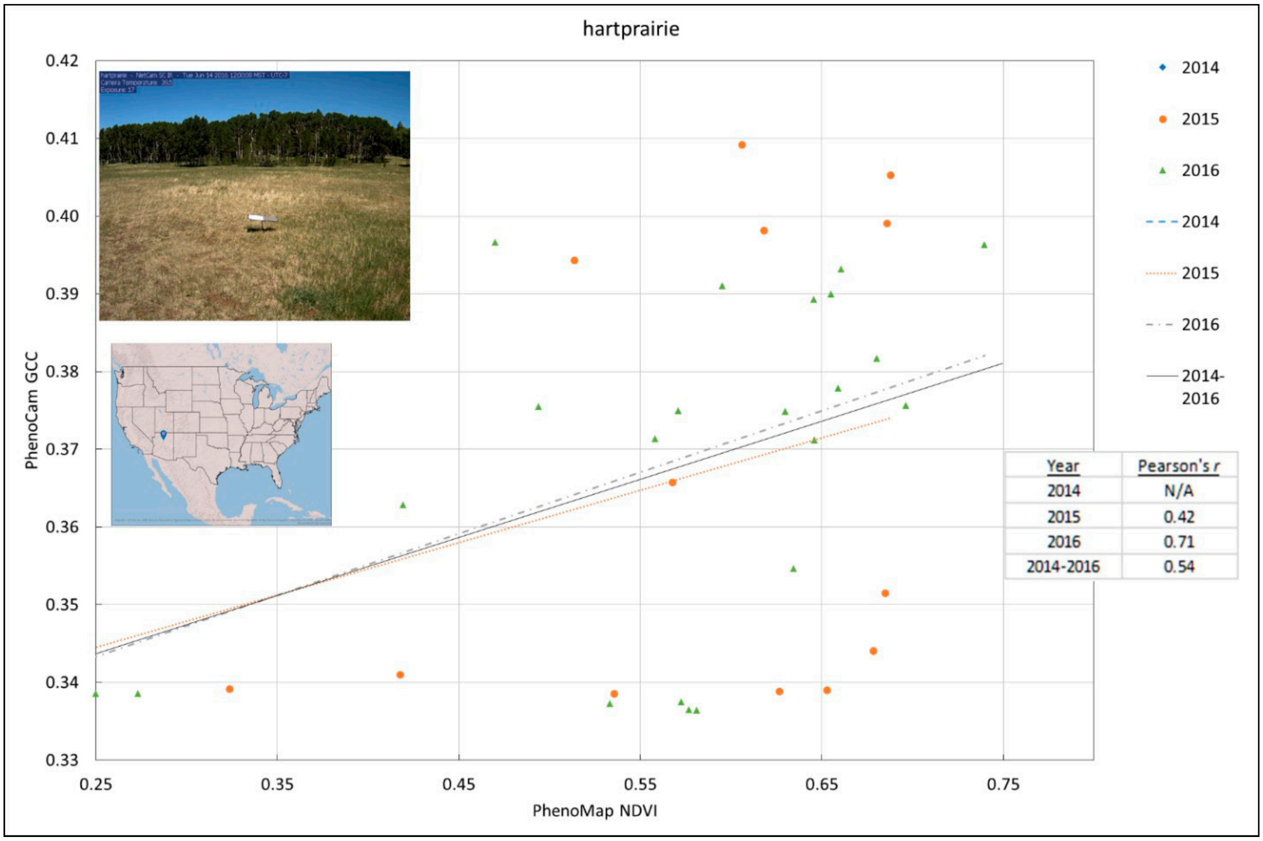


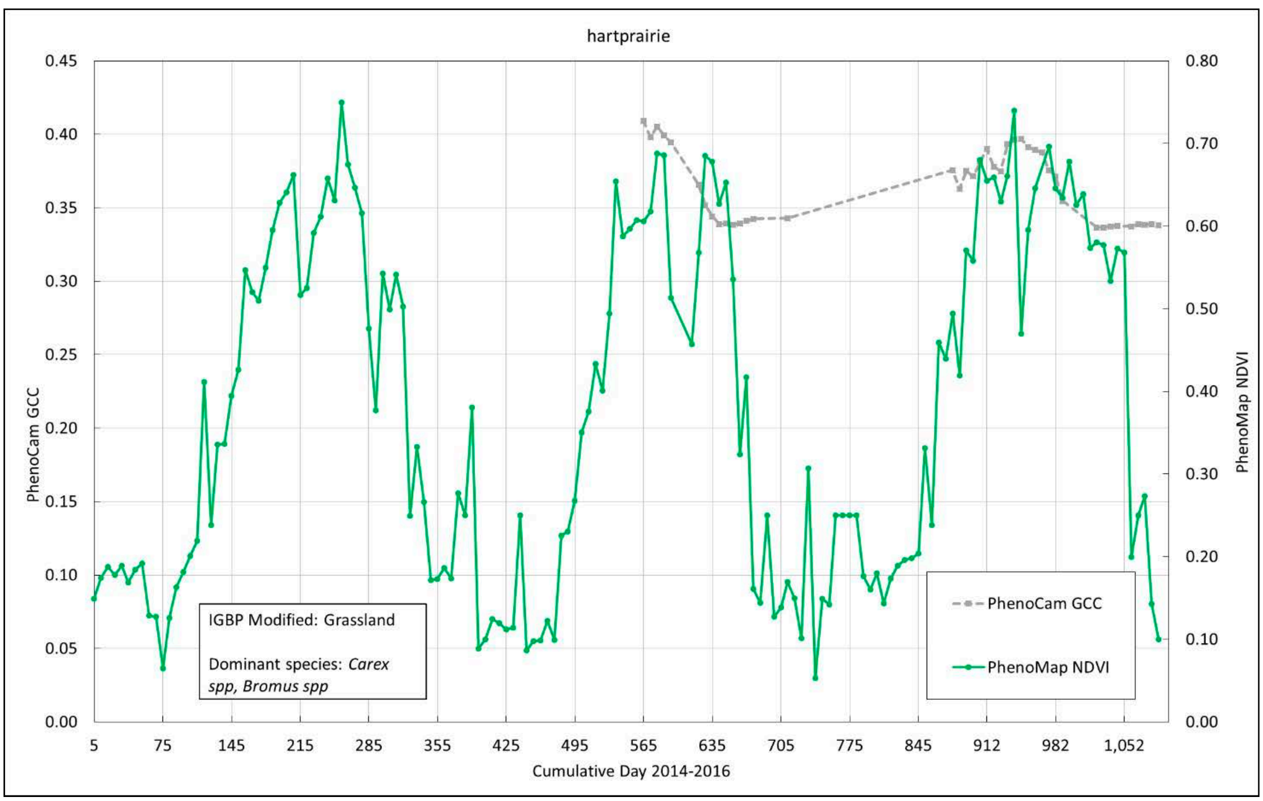


Figure 27—(A) Line graph and (B) scatterplot of the PhenoCam green chromatic coordinate ($gcc_{per90}$) and PhenoMap eMODIS NDVI weekly values 2014–2016 for the hartprairie site. Inset graphics in the line graph show a representative PhenoCam image and a map showing the location of the site.

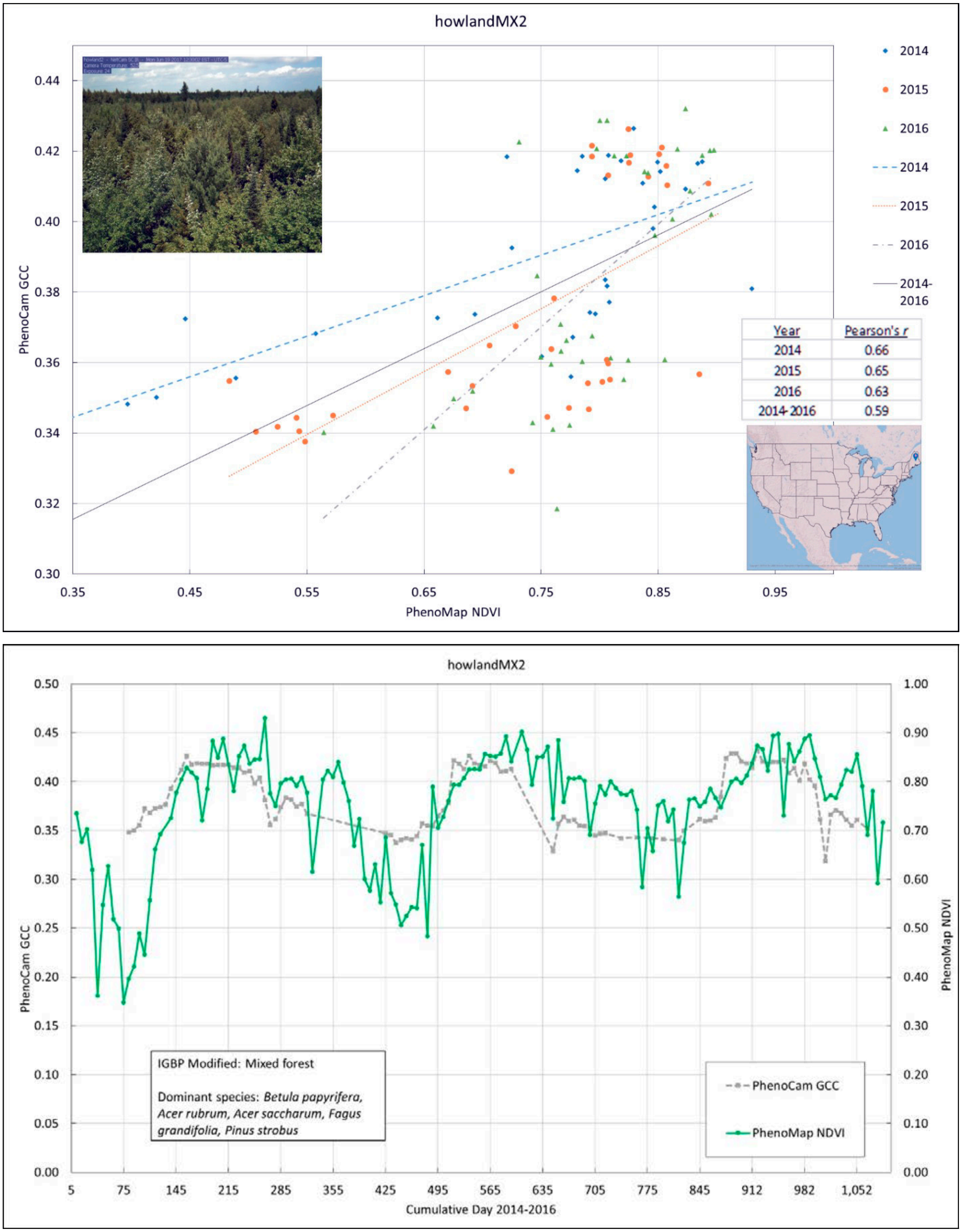


Figure 28—(A) Line graph and (B) scatterplot of the PhenoCam green chromatic coordinate ($gcc_{per90}$) and PhenoMap eMODIS NDVI weekly values 2014–2016 for the howlandMX2 site. Inset graphics in the line graph show a representative PhenoCam image and a map showing the location of the site.

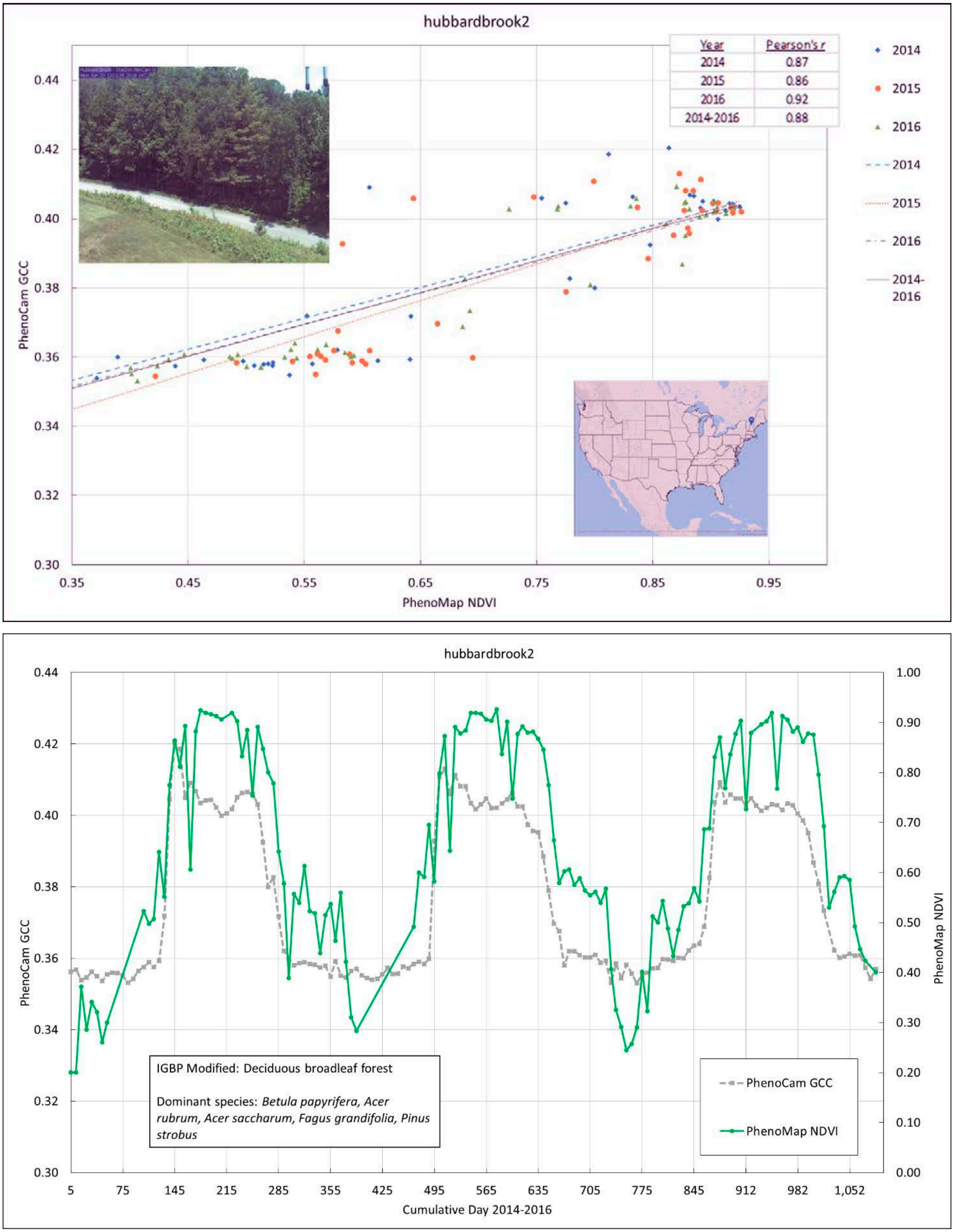


Figure 29—(A) Line graph and (B) scatterplot of the PhenoCam green chromatic coordinate ($gcc_{per90}$) and PhenoMap eMODIS NDVI weekly values 2014–2016 for the hubbardbrook2 site. Inset graphics in the line graph show a representative PhenoCam image and a map showing the location of the site.

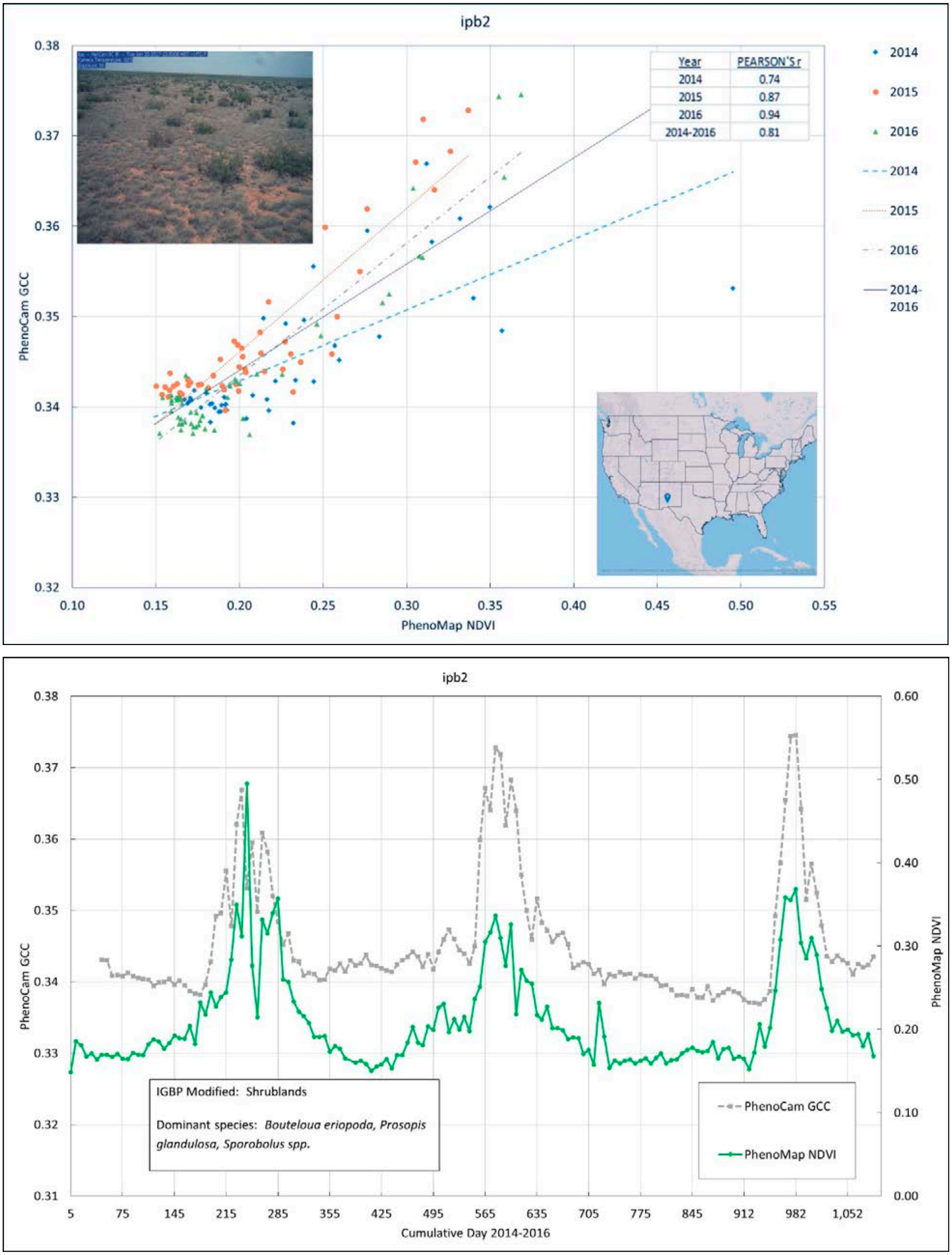


Figure 30—(A) Line graph and (B) scatterplot of the PhenoCam green chromatic coordinate ($gcc_{per90}$) and PhenoMap eMODIS NDVI weekly values 2014–2016 for the ibp2 site. Inset graphics in the line graph show a representative PhenoCam image and a map showing the location of the site.

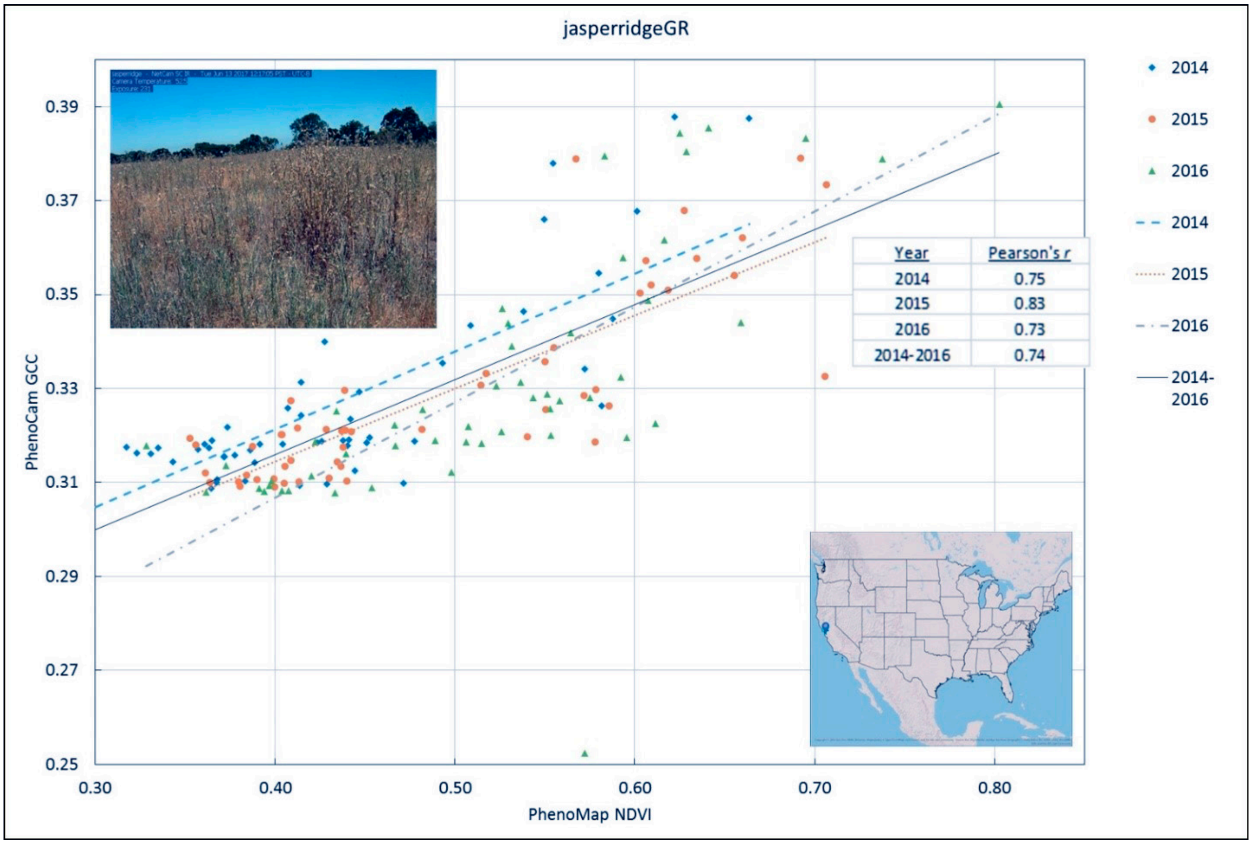


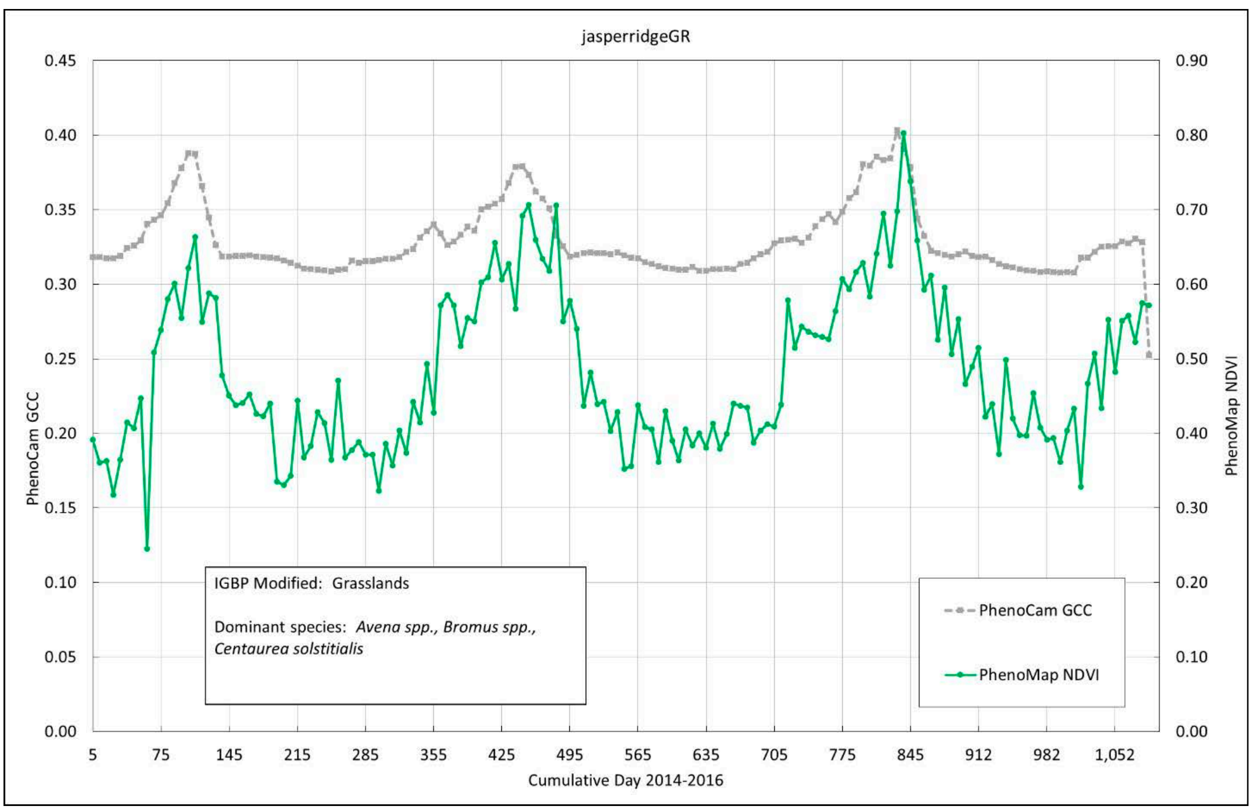


Figure 31—(A) Line graph and (B) scatterplot of the PhenoCam green chromatic coordinate ($gcc_{per90}$) and PhenoMap eMODIS NDVI weekly values 2014–2016 for the jasperridgeGR site. Inset graphics in the line graph show a representative PhenoCam image and a map showing the location of the site.

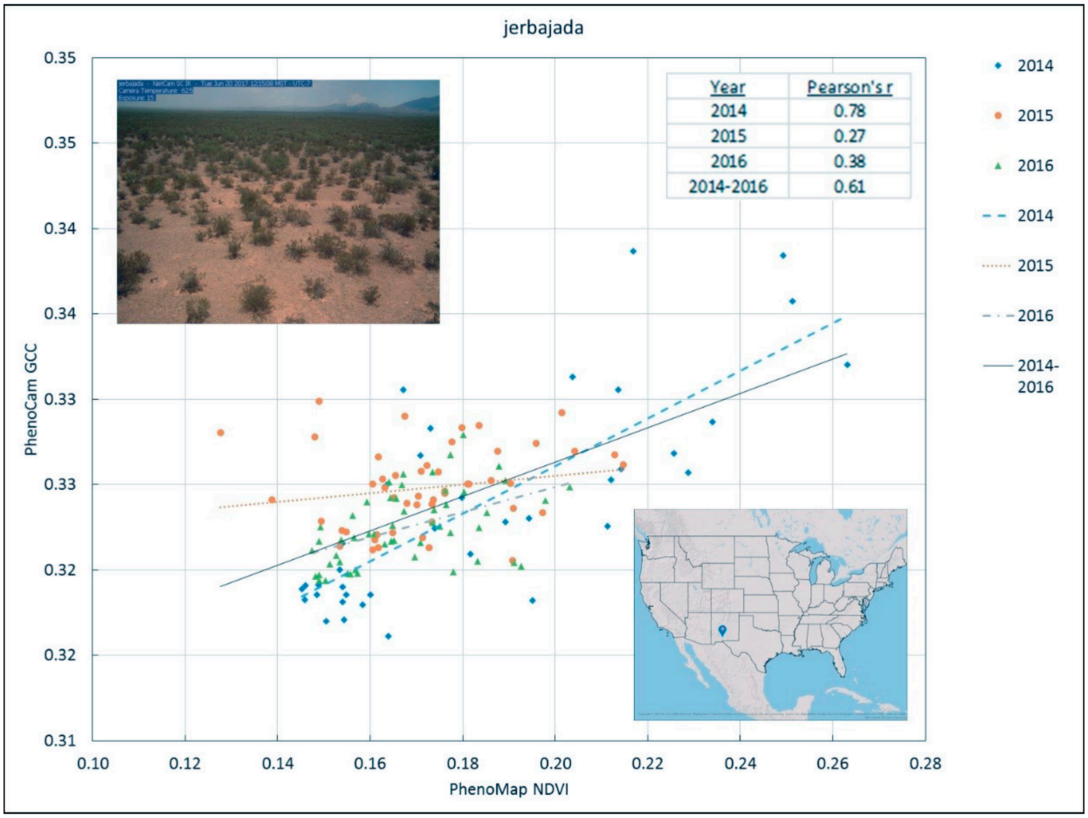


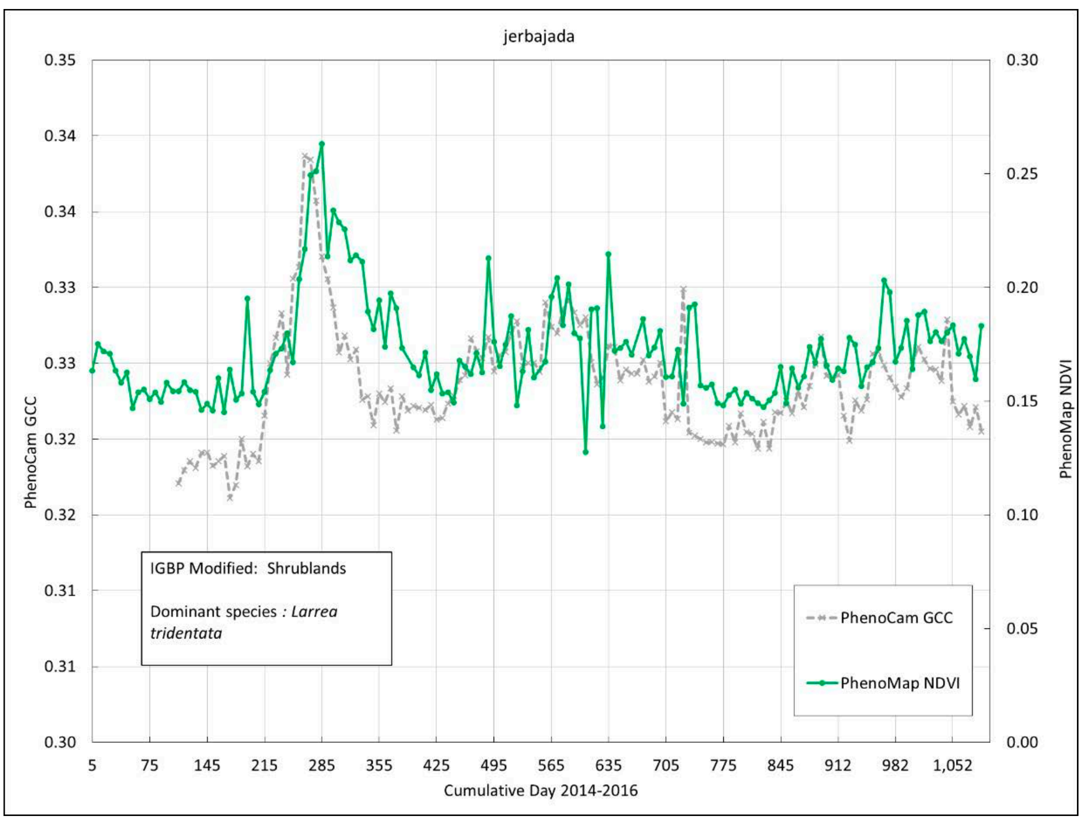


Figure 32—(A) Line graph and (B) scatterplot of the PhenoCam green chromatic coordinate ($gcc_{per90}$) and PhenoMap eMODIS NDVI weekly values 2014-2016 for the jerbajada site. Inset graphics in the line graph show a representative PhenoCam image and a map showing the location of the site.

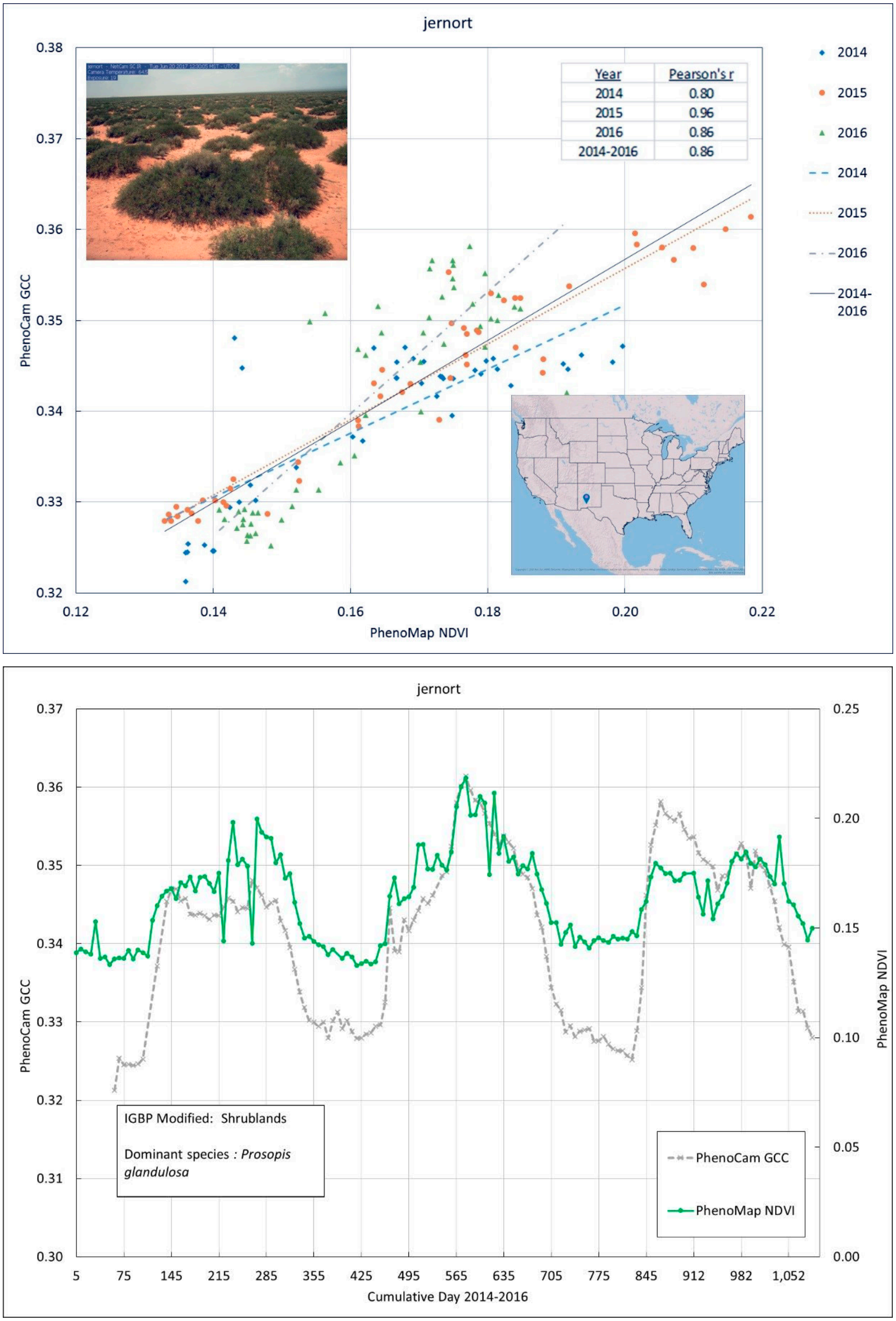


Figure 33—(A) Line graph and (B) scatterplot of the PhenoCam green chromatic coordinate ($gcc_{per90}$) and PhenoMap eMODIS NDVI weekly values 2014–2016 for the jernort site. Inset graphics in the line graph show a representative PhenoCam image and a map showing the location of the site.

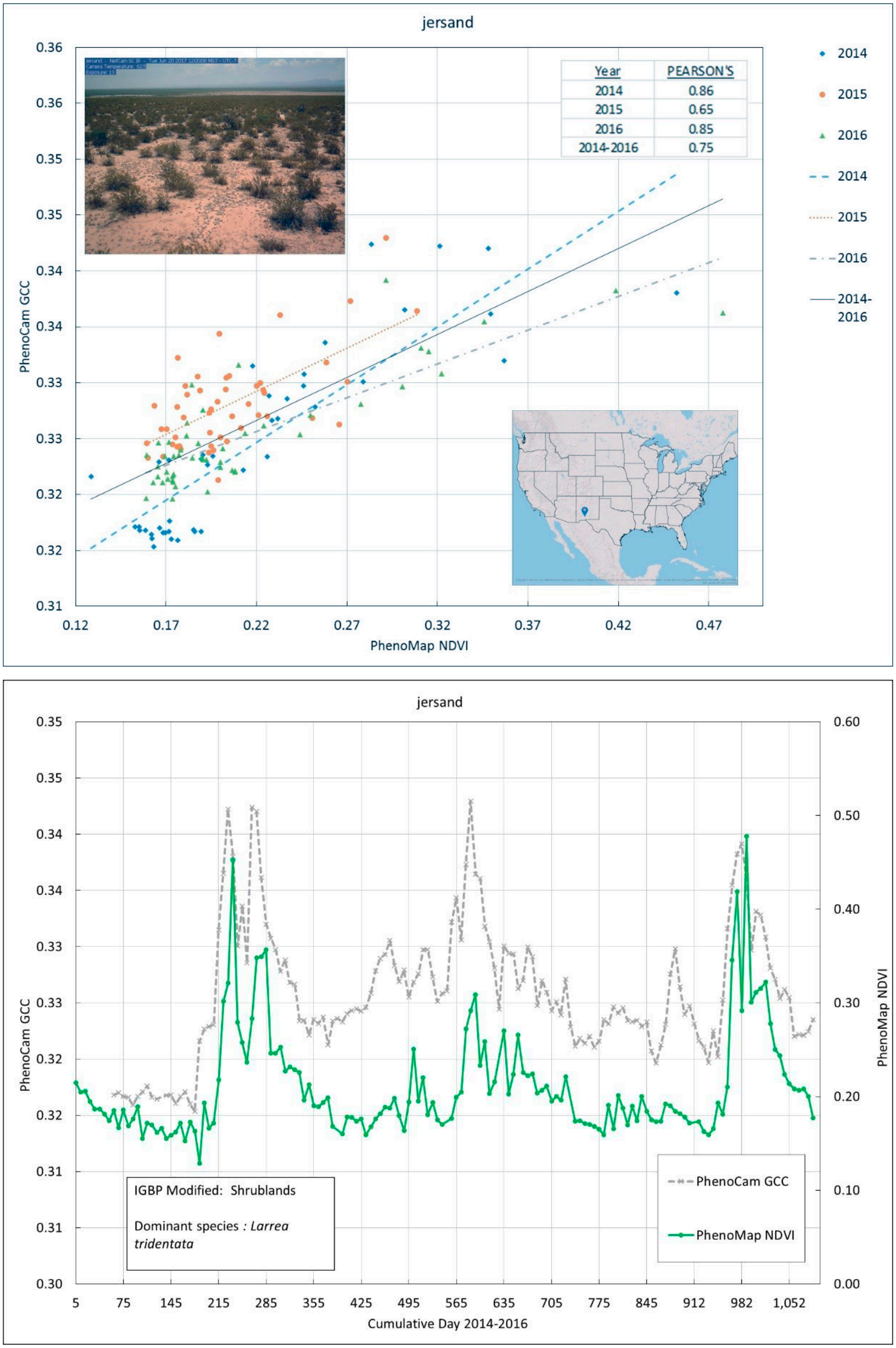


Figure 34—(A) Line graph and (B) scatterplot of the PhenoCam green chromatic coordinate ($gcc_{per90}$) and PhenoMap eMODIS NDVI weekly values 2014–2016 for the jersand site. Inset graphics in the line graph show a representative PhenoCam image and a map showing the location of the site.

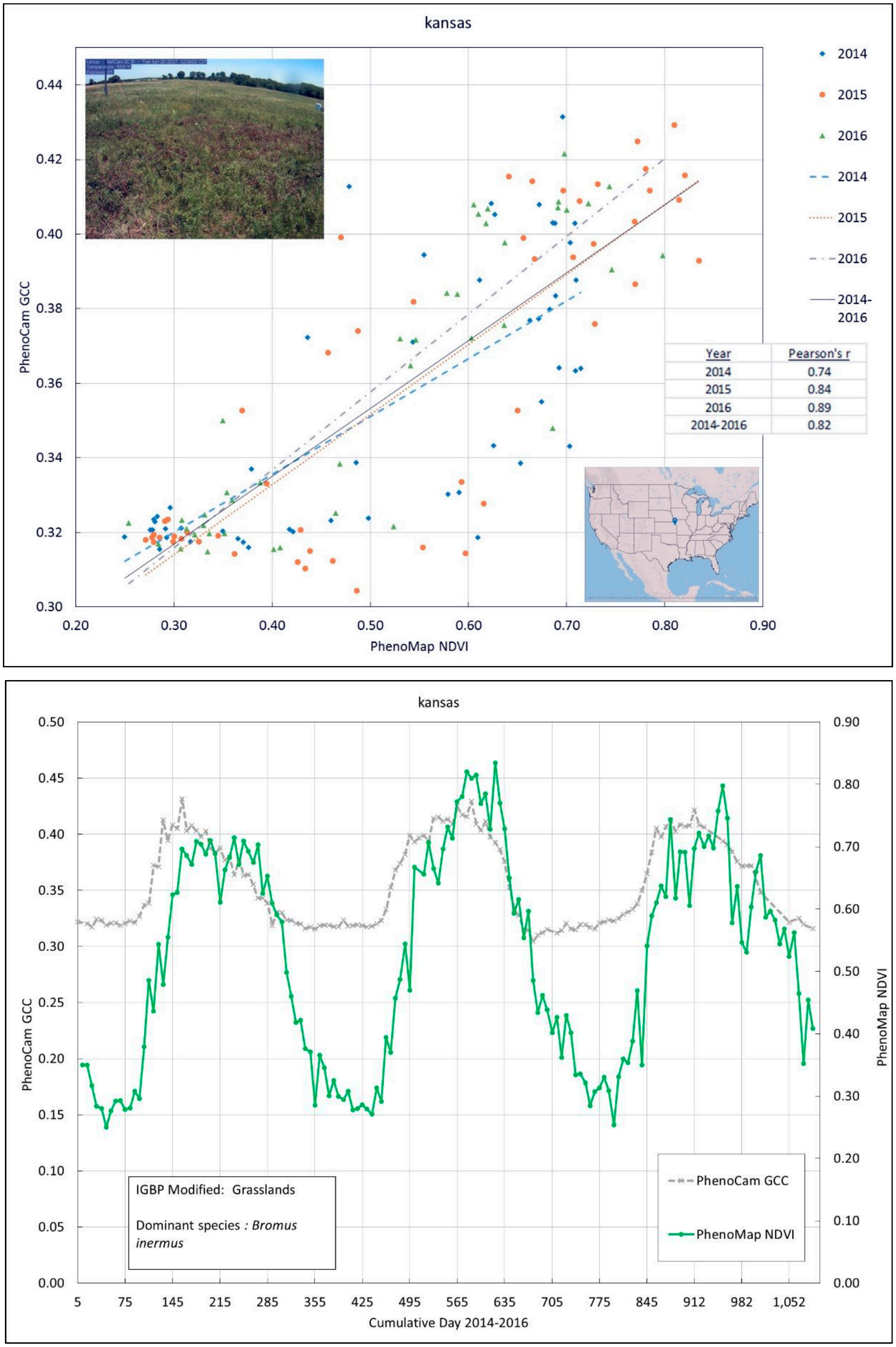


Figure 13—(A) Line graph and (B) scatterplot of the PhenoCam green chromatic coordinate ($gcc_{per90}$) and PhenoMap eMODIS NDVI weekly values 2014–2016 for the kansas site. Inset graphics in the line graph show a representative PhenoCam image and a map showing the location of the site.

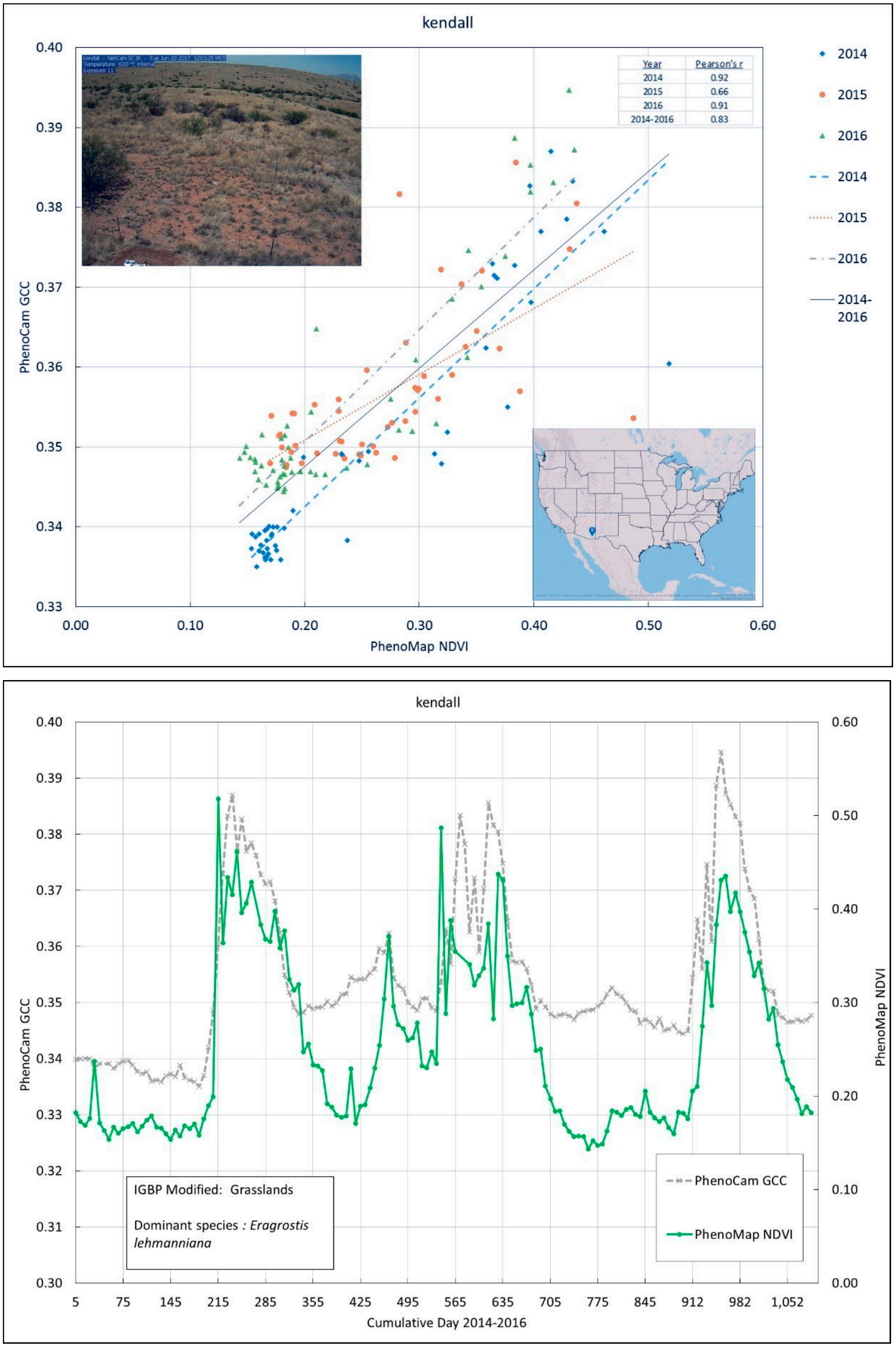


Figure 36—(A) Line graph and (B) scatterplot of the PhenoCam green chromatic coordinate ($gcc_{per90}$) and PhenoMap eMODIS NDVI weekly values 2014–2016 for the kendall site. Inset graphics in the line graph show a representative PhenoCam image and a map showing the location of the site.

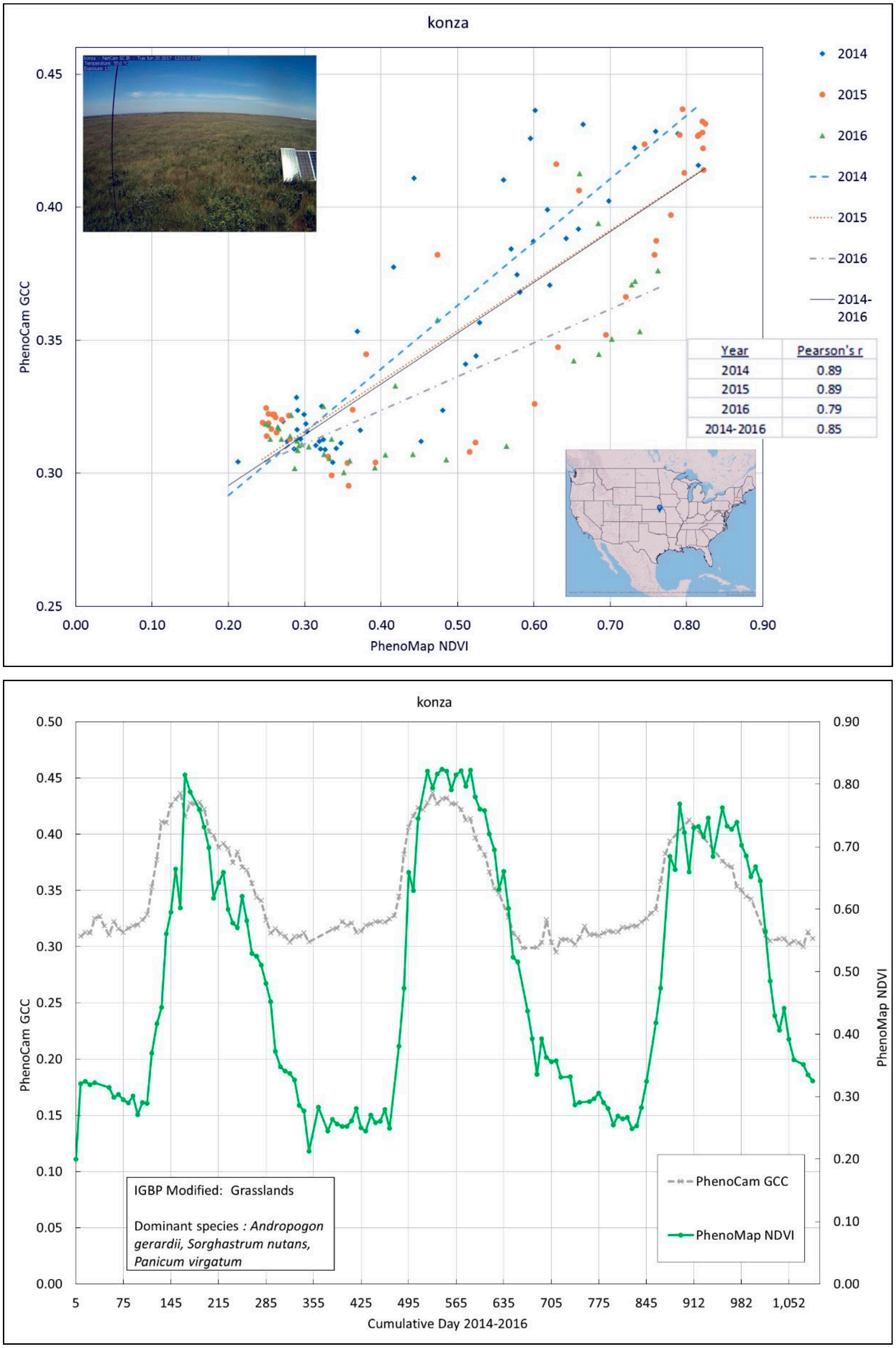


Figure 37—(A) Line graph and (B) scatterplot of the PhenoCam green chromatic coordinate ($gcc_{per90}$) and PhenoMap eMODIS NDVI weekly values 2014–2016 for the konza site. Inset graphics in the line graph show a representative PhenoCam image and a map showing the location of the site.

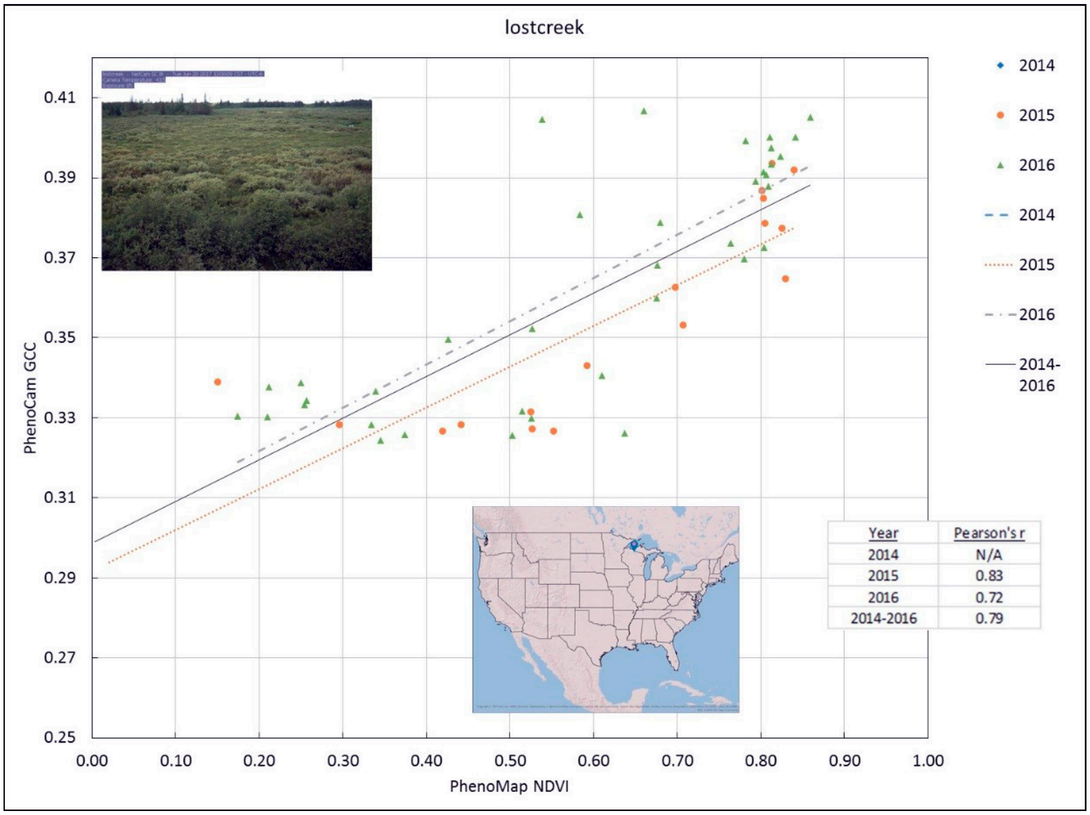


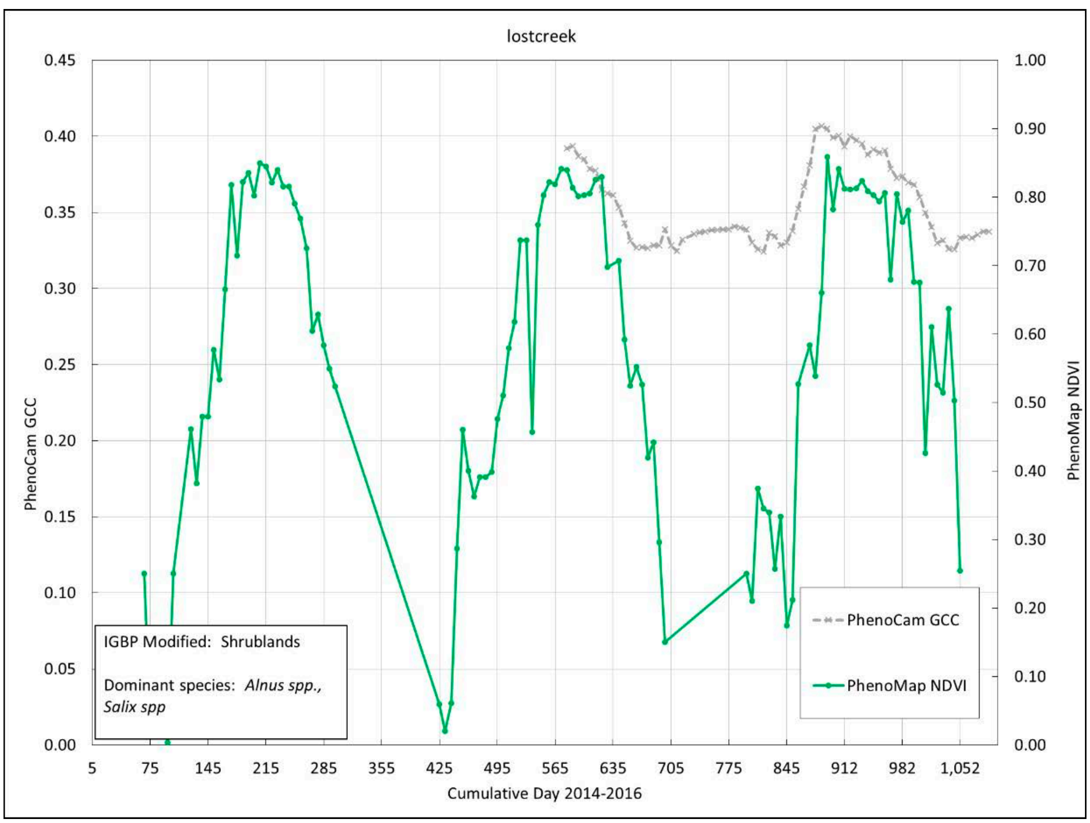


Figure 38—(A) Line graph and (B) scatterplot of the PhenoCam green chromatic coordinate ($gcc_{per90}$) and PhenoMap eMODIS NDVI weekly values 2014–2016 for the lostcreek site. Inset graphics in the line graph show a representative PhenoCam image and a map showing the location of the site.

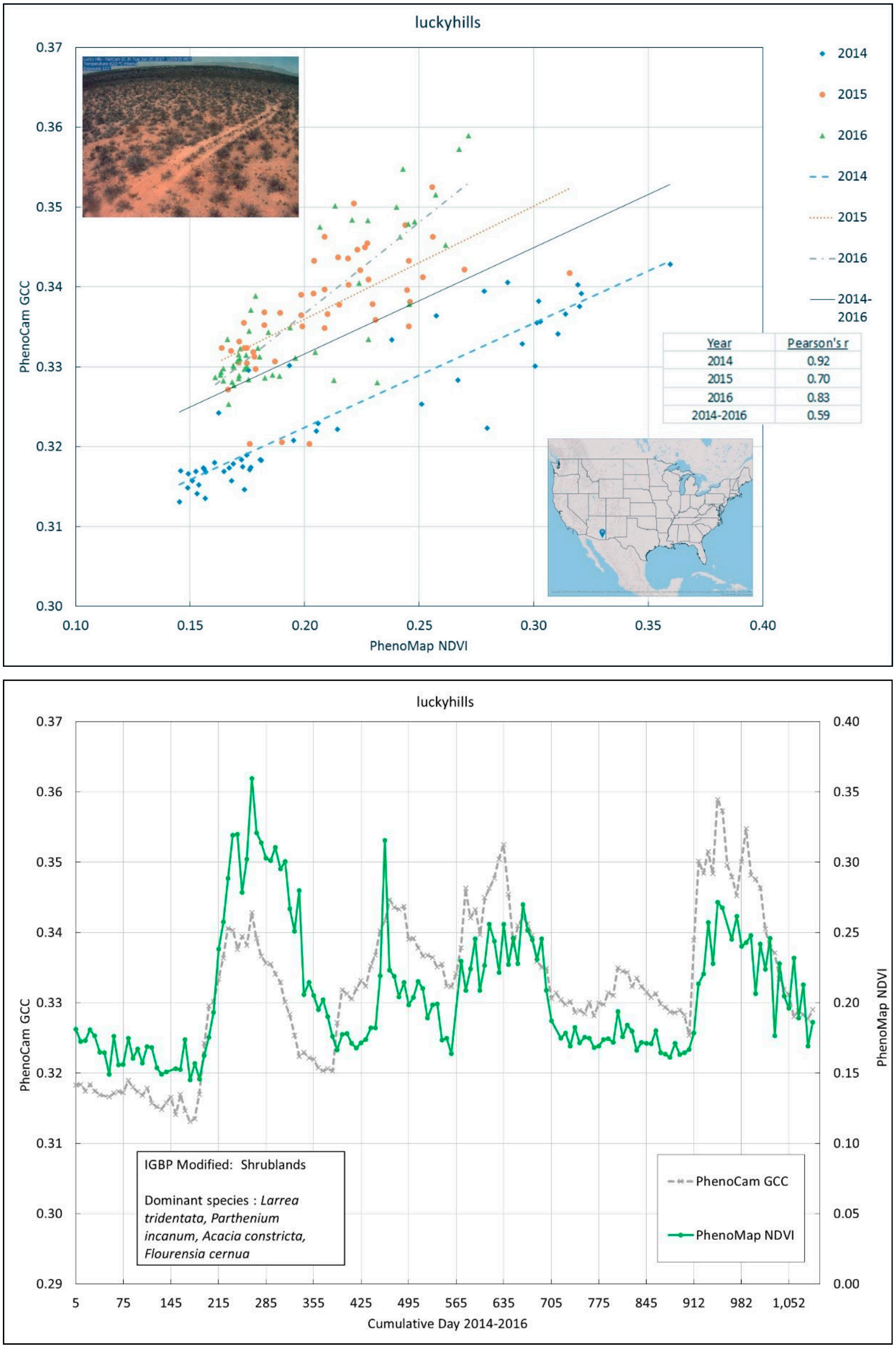


Figure 39—(A) Line graph and (B) scatterplot of the PhenoCam green chromatic coordinate ($gcc_{per90}$) and PhenoMap eMODIS NDVI weekly values 2014–2016 for the luckyhills site. Inset graphics in the line graph show a representative PhenoCam image and a map showing the location of the site.

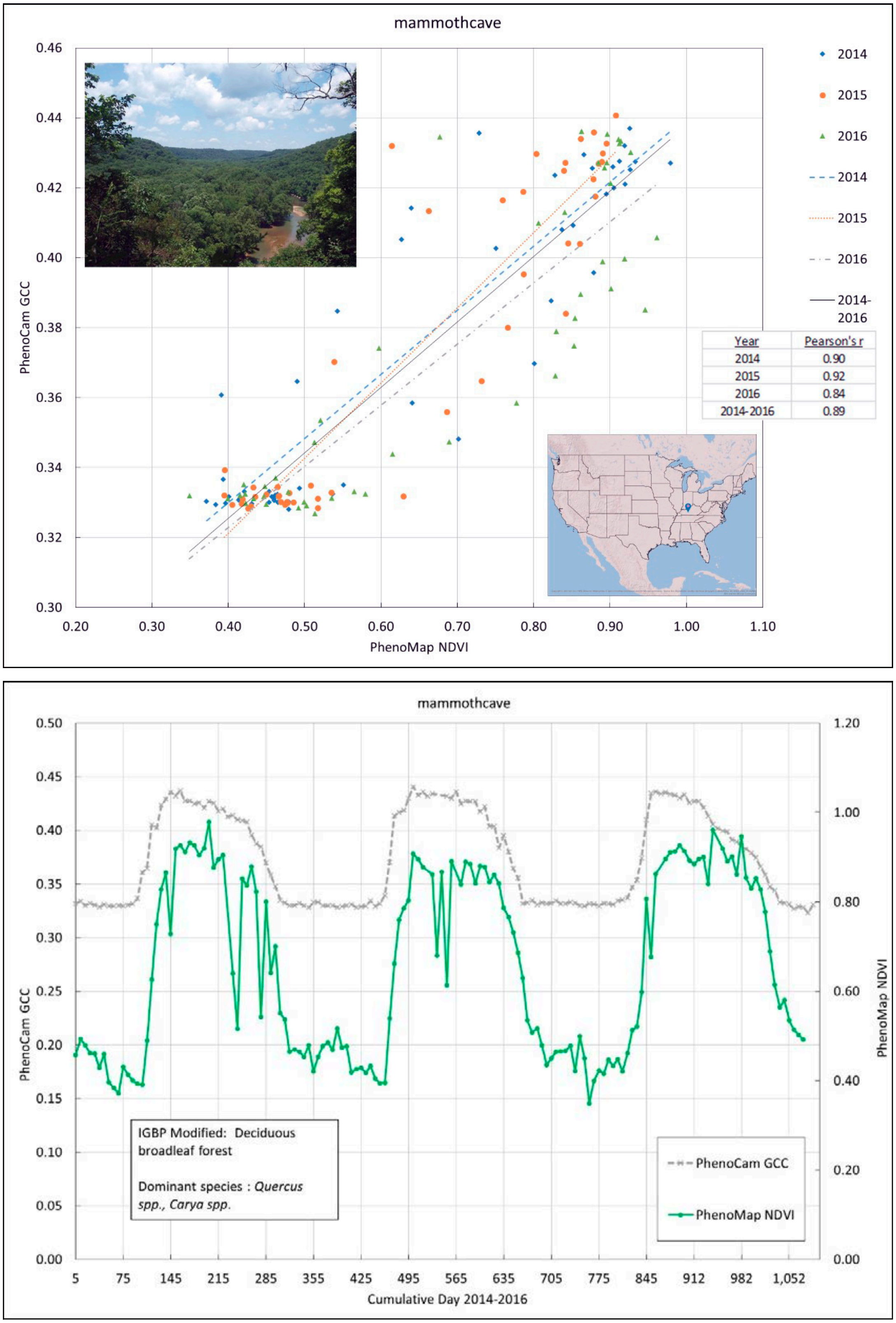


Figure 40—(A) Line graph and (B) scatterplot of the PhenoCam green chromatic coordinate ($gcc_{per90}$) and PhenoMap eMODIS NDVI weekly values 2014–2016 for the mammothcave site. Inset graphics in the line graph show a representative PhenoCam image and a map showing the location of the site.

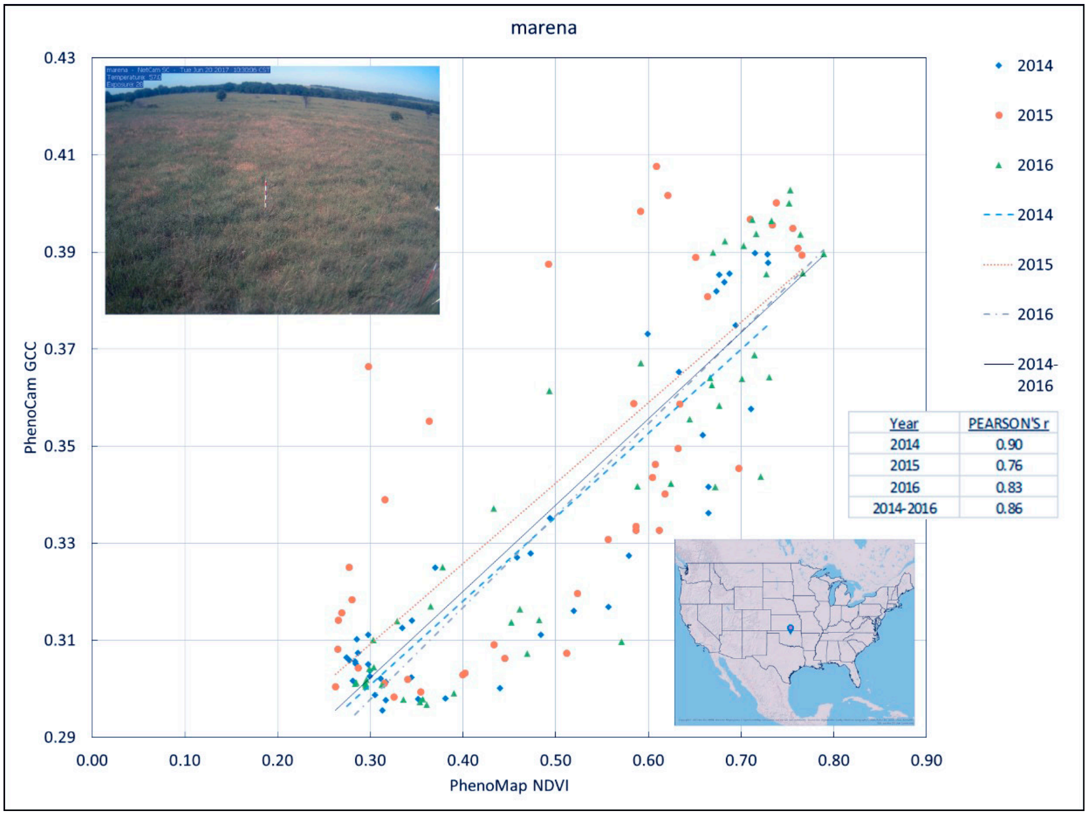


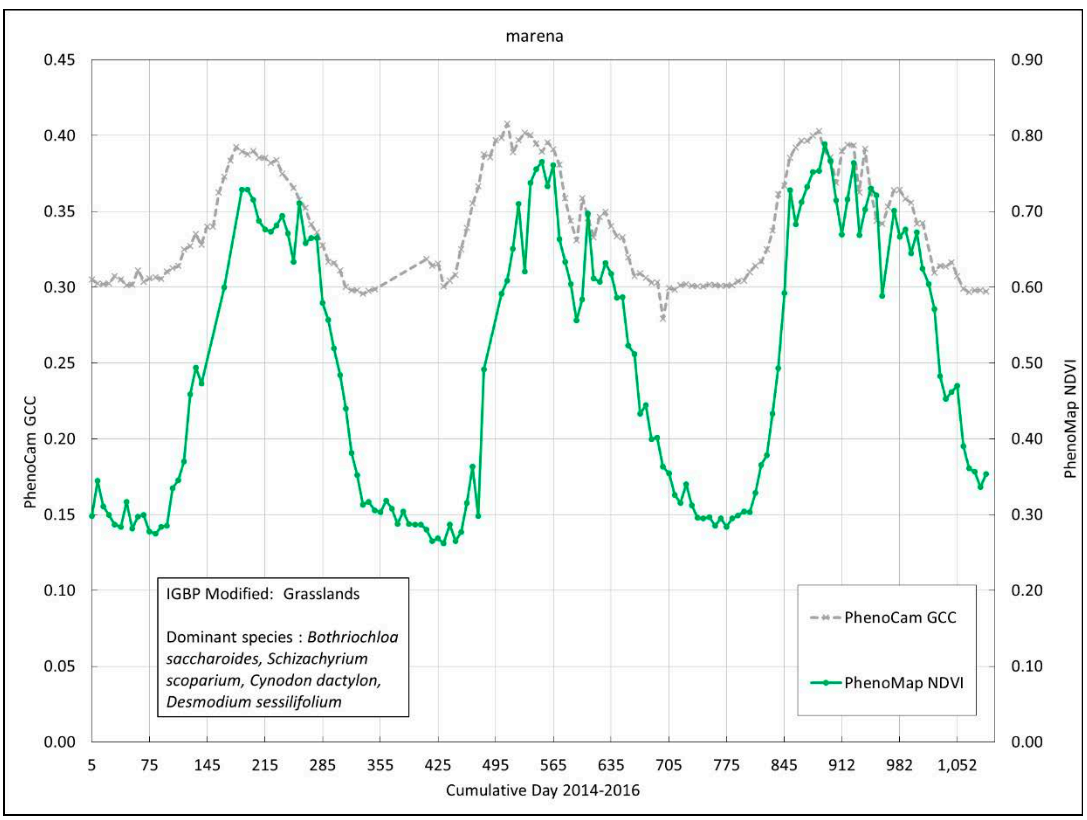


Figure 41—(A) Line graph and (B) scatterplot of the PhenoCam green chromatic coordinate ($gcc_{per90}$) and PhenoMap eMODIS NDVI weekly values 2014–2016 for the marena site. Inset graphics in the line graph show a representative PhenoCam image and a map showing the location of the site.

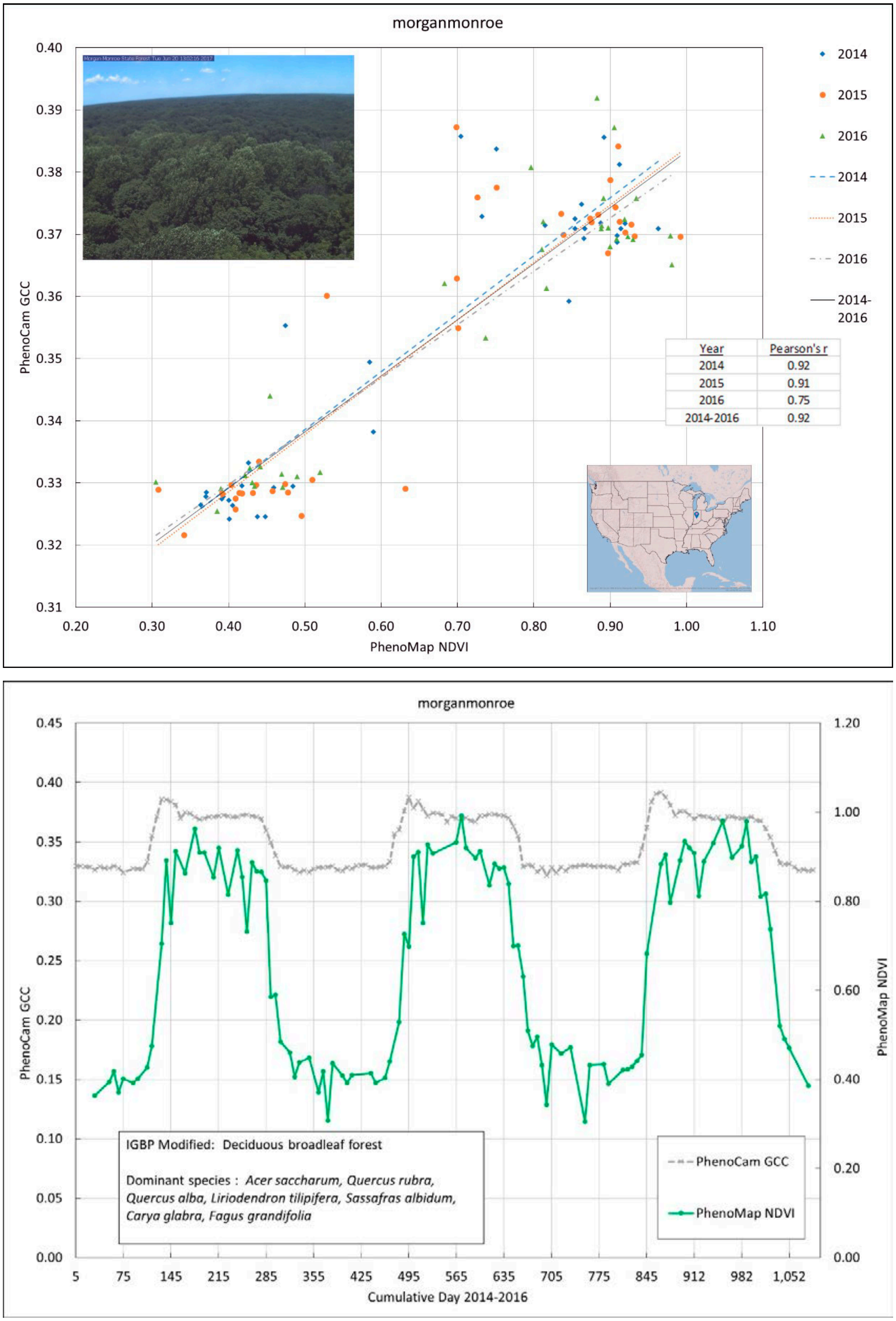


Figure 42—(A) Line graph and (B) scatterplot of the PhenoCam green chromatic coordinate ($gcc_{per90}$) and PhenoMap eMODIS NDVI weekly values 2014–2016 for the morganmonroe site. Inset graphics in the line graph show a representative PhenoCam image and a map showing the location of the site.

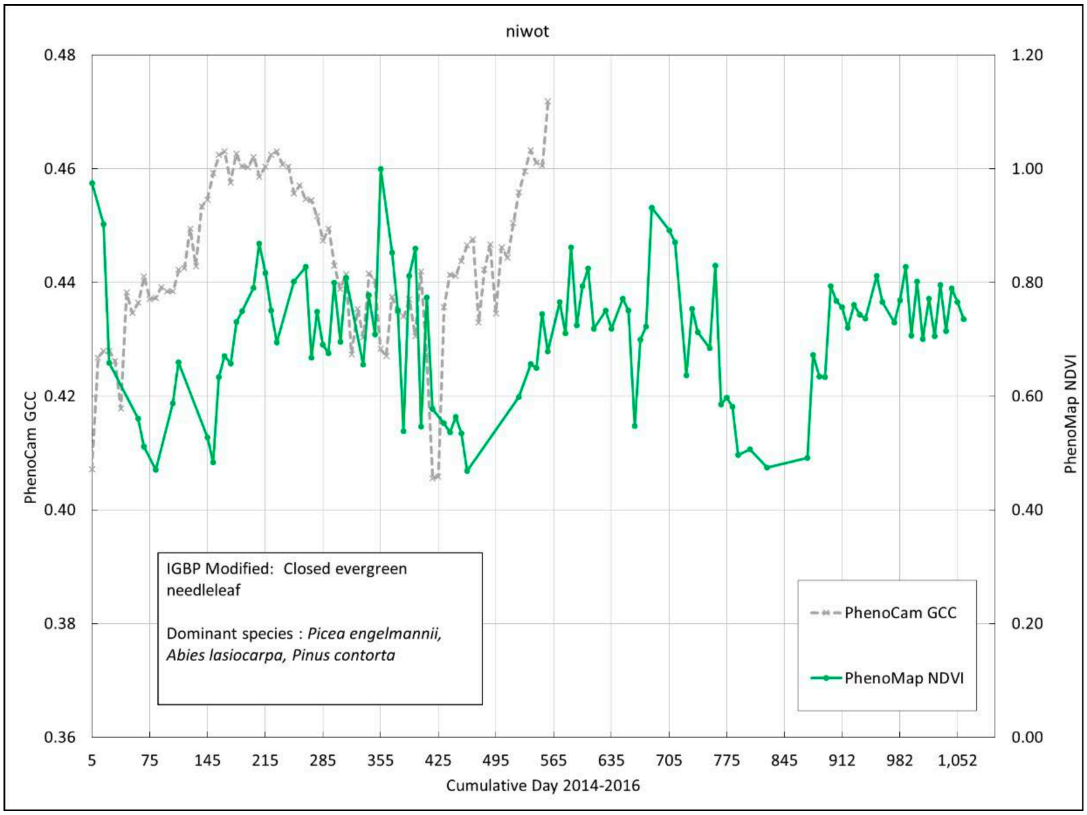


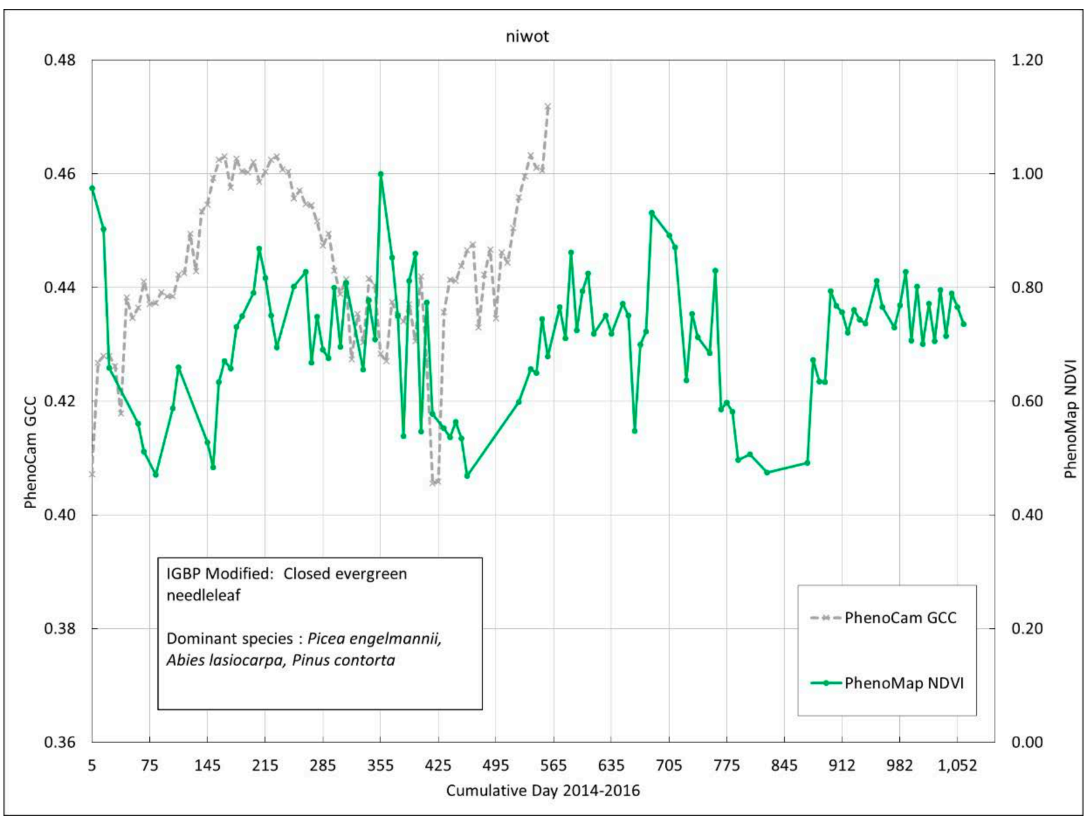


Figure 43—(A) Line graph and (B) scatterplot of the PhenoCam green chromatic coordinate ($gcc_{per90}$) and PhenoMap eMODIS NDVI weekly values 2014–2016 for the niwot site. Inset graphics in the line graph show a representative PhenoCam image and a map showing the location of the site.

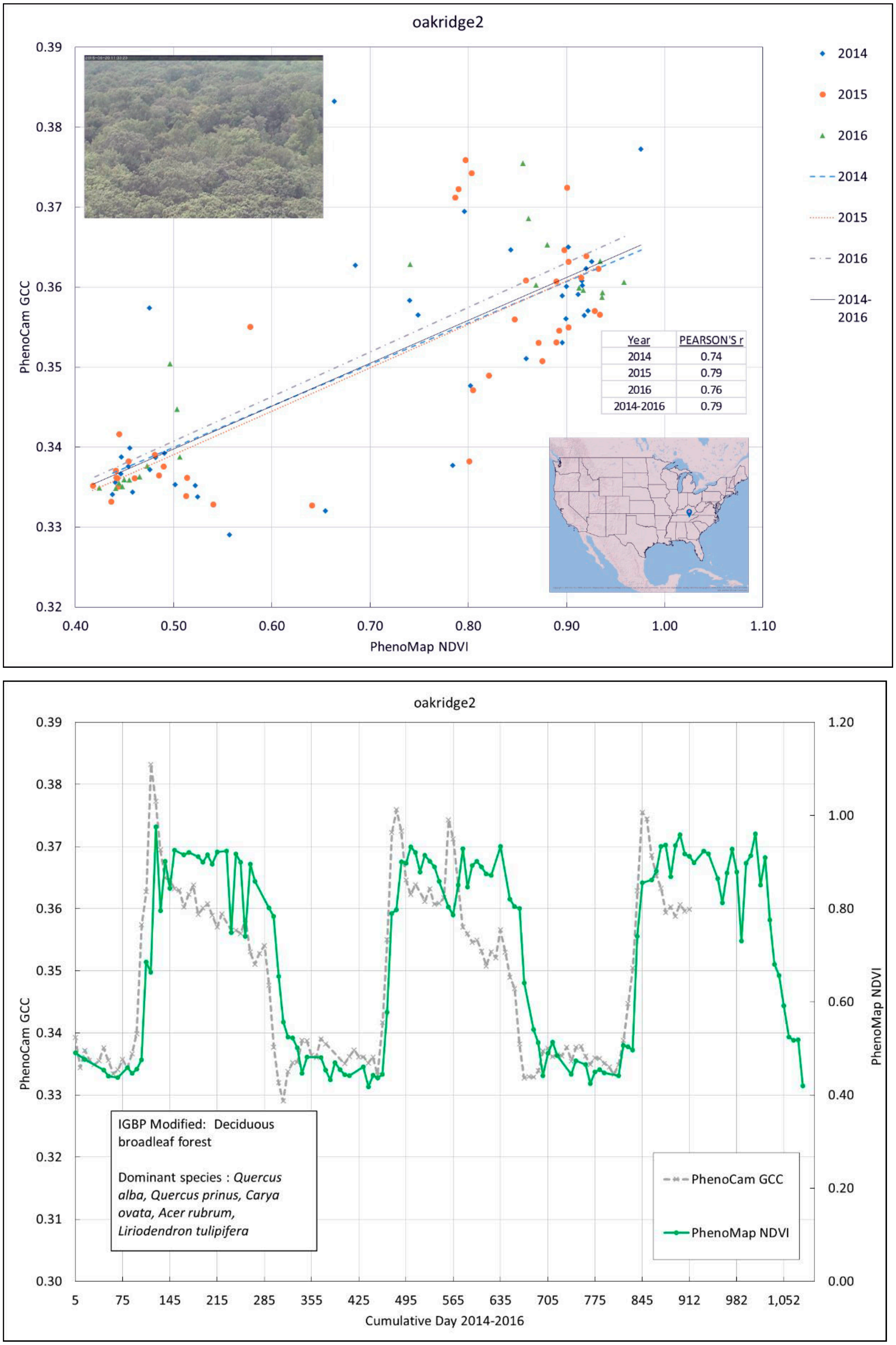


Figure 44—(A) Line graph and (B) scatterplot of the PhenoCam green chromatic coordinate ($gcc_{per90}$) and PhenoMap eMODIS NDVI weekly values 2014–2016 for the oakridge2 site. Inset graphics in the line graph show a representative PhenoCam image and a map showing the location of the site.

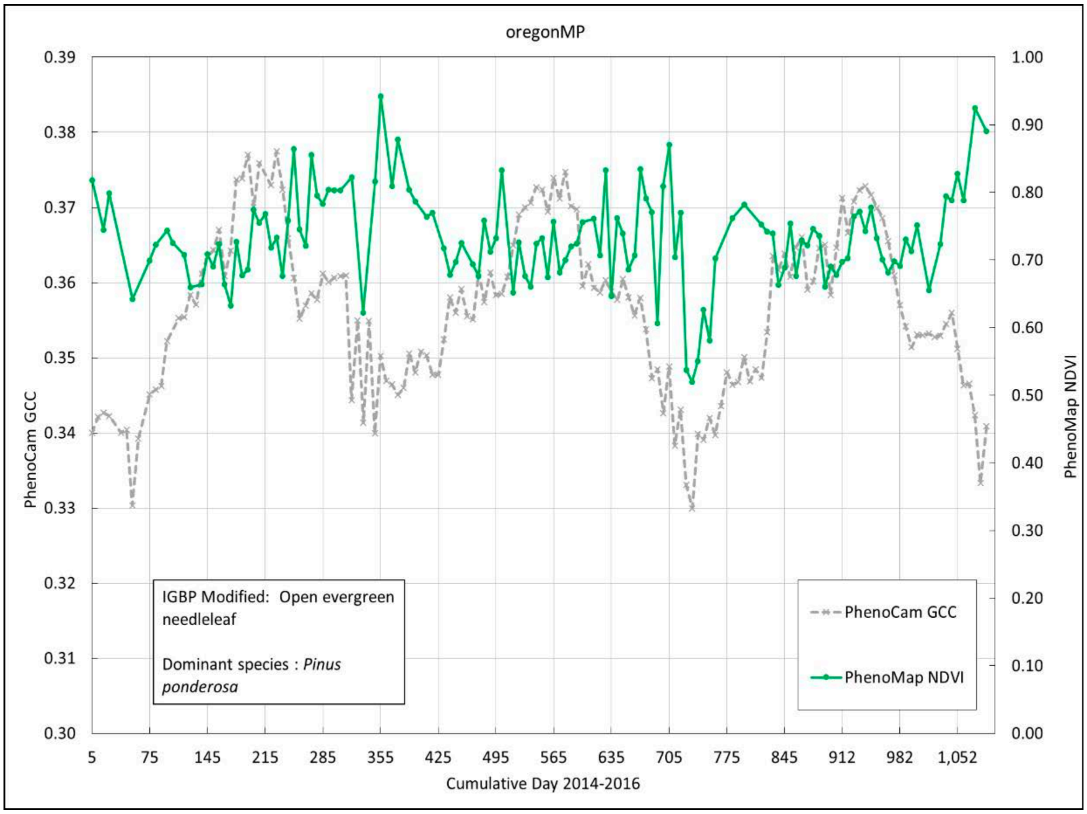


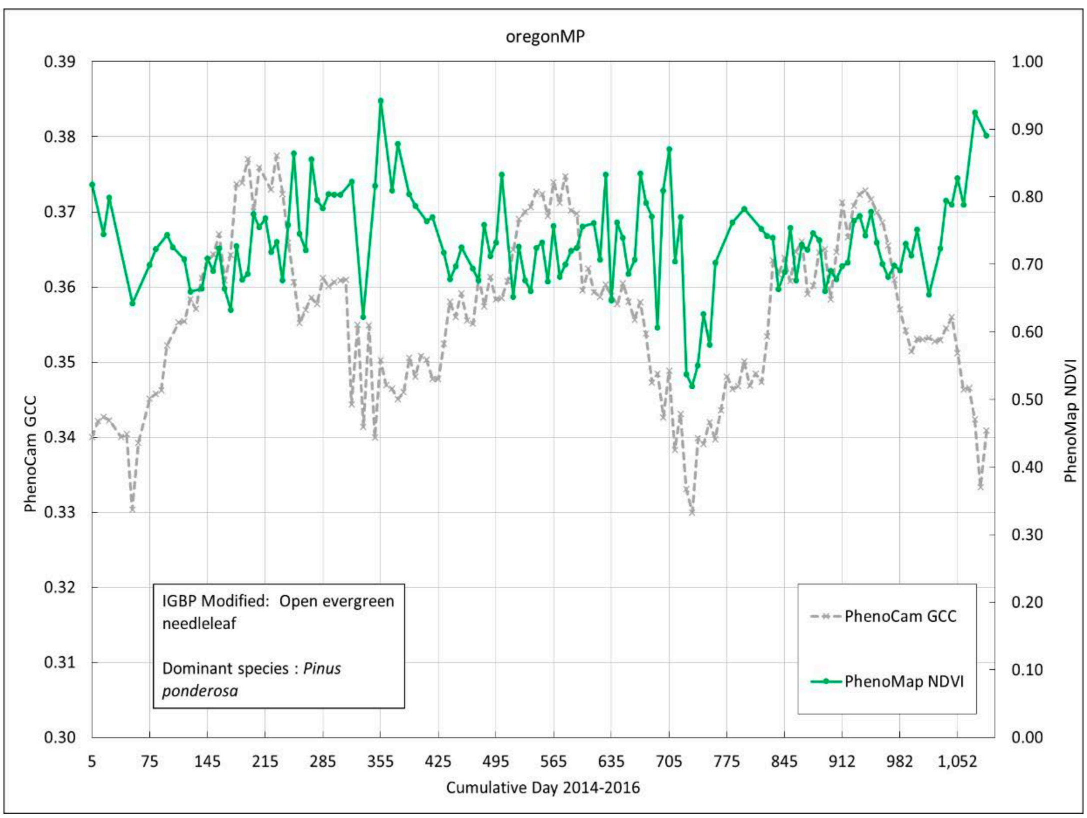


Figure 45—(A) Line graph and (B) scatterplot of the PhenoCam green chromatic coordinate ($gcc_{per90}$) and PhenoMap eMODIS NDVI weekly values 2014–2016 for the oregonMP site. Inset graphics in the line graph show a representative PhenoCam image and a map showing the location of the site.

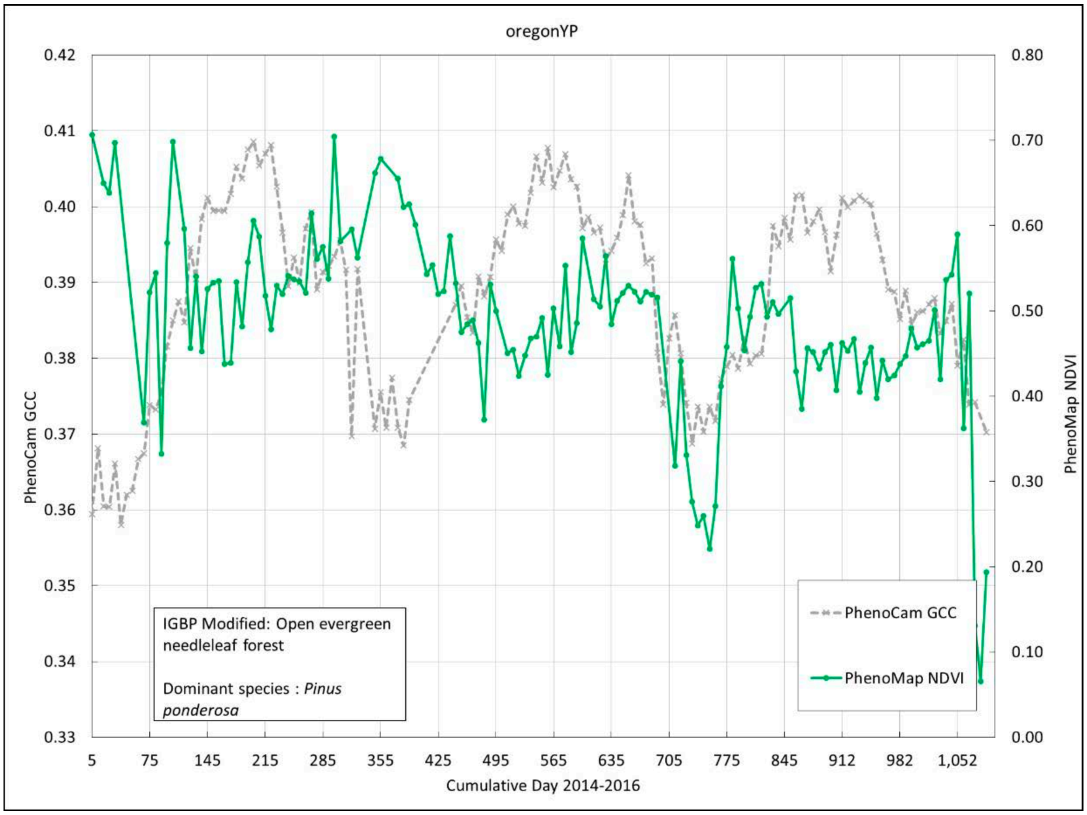


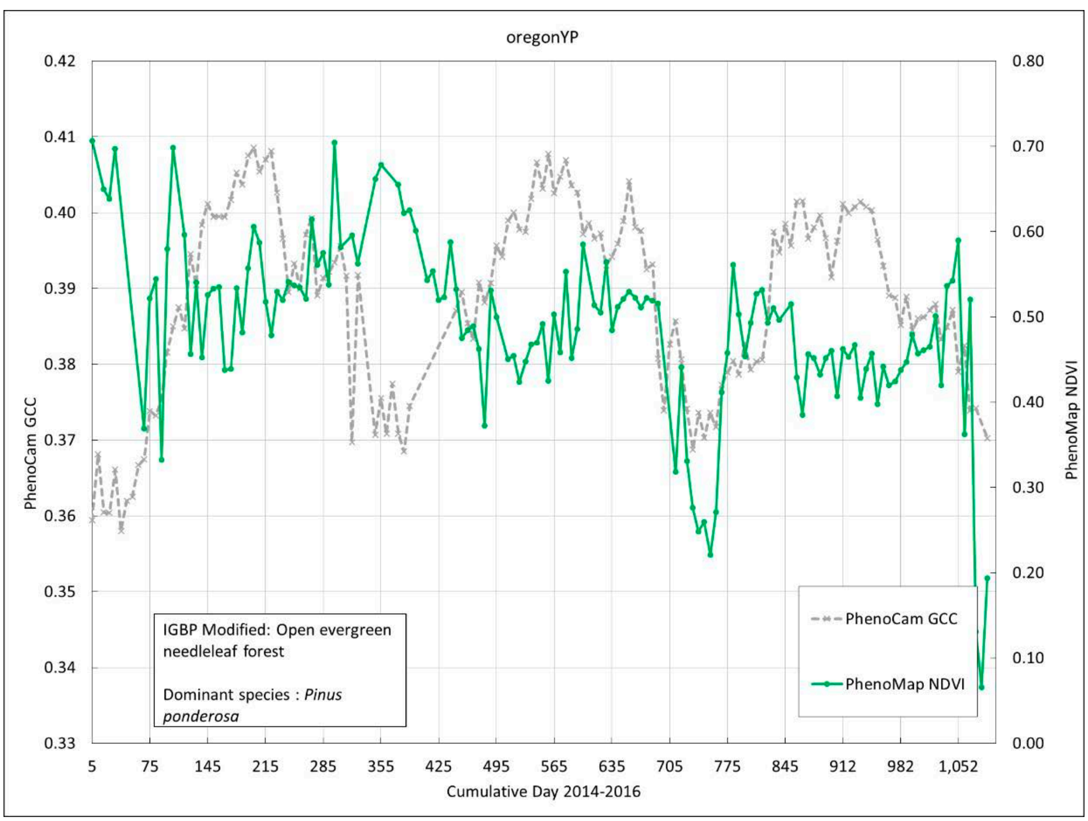


Figure 46—(A) Line graph and (B) scatterplot of the PhenoCam green chromatic coordinate ($gcc_{per90}$) and PhenoMap eMODIS NDVI weekly values 2014–2016 for the oregonYP site. Inset graphics in the line graph show a representative PhenoCam image and a map showing the location of the site.

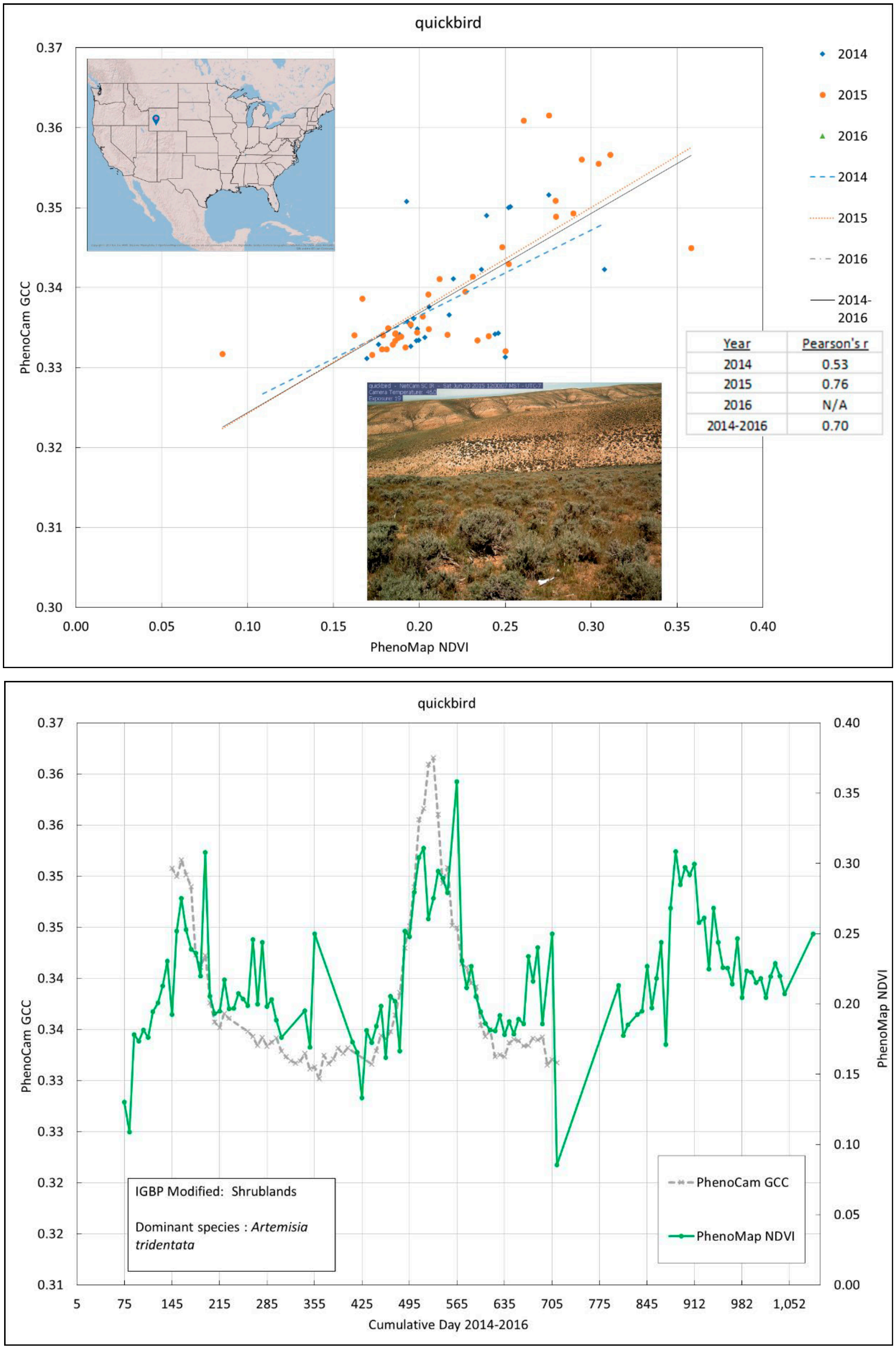


Figure 47—(A) Line graph and (B) scatterplot of the PhenoCam green chromatic coordinate ($gcc_{per90}$) and PhenoMap eMODIS NDVI weekly values 2014–2016 for the quickbird site. Inset graphics in the line graph show a representative PhenoCam image and a map showing the location of the site.

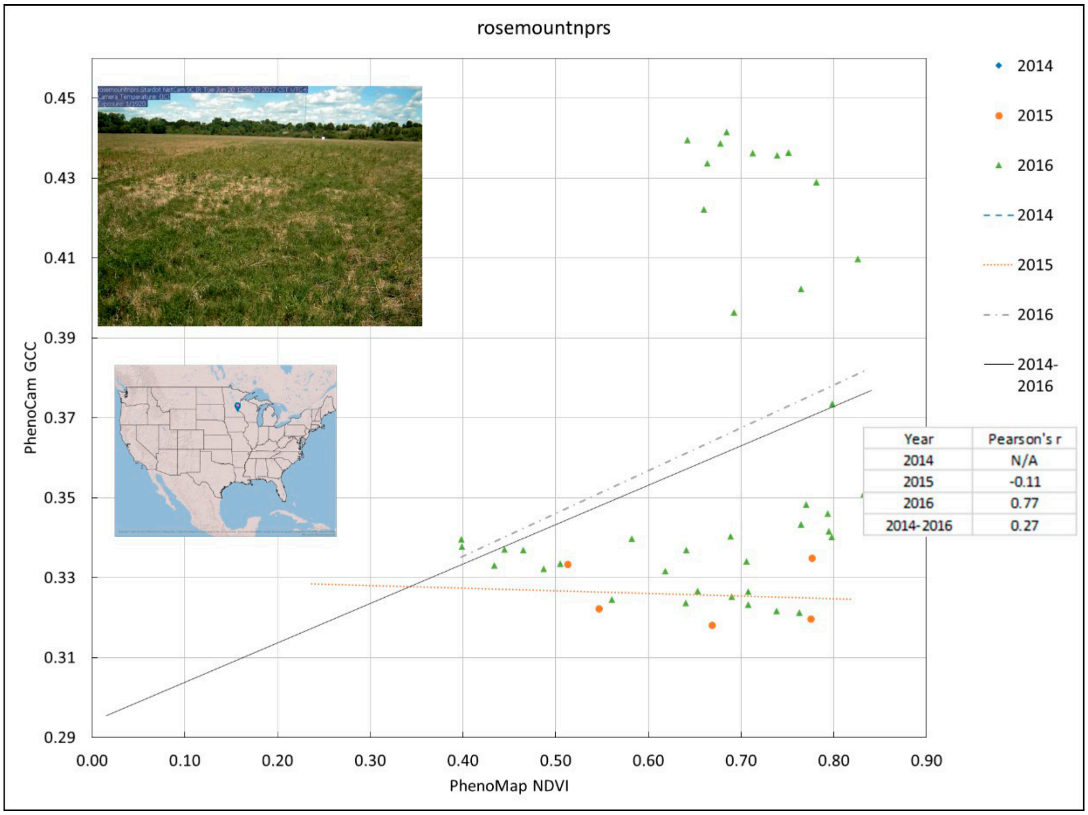


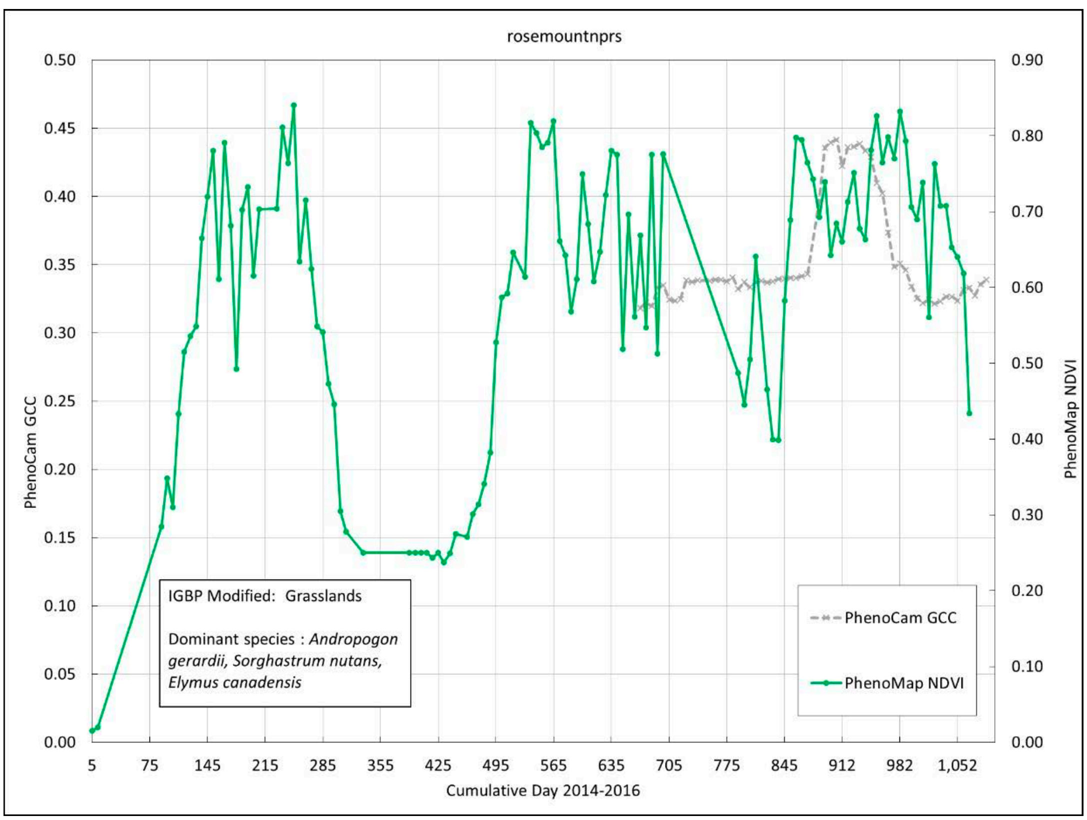


Figure 48—(A) Line graph and (B) scatterplot of the PhenoCam green chromatic coordinate ($gcc_{per90}$) and PhenoMap eMODIS NDVI weekly values 2014–2016 for the rosemountnprs site. Inset graphics in the line graph show a representative PhenoCam image and a map showing the location of the site.

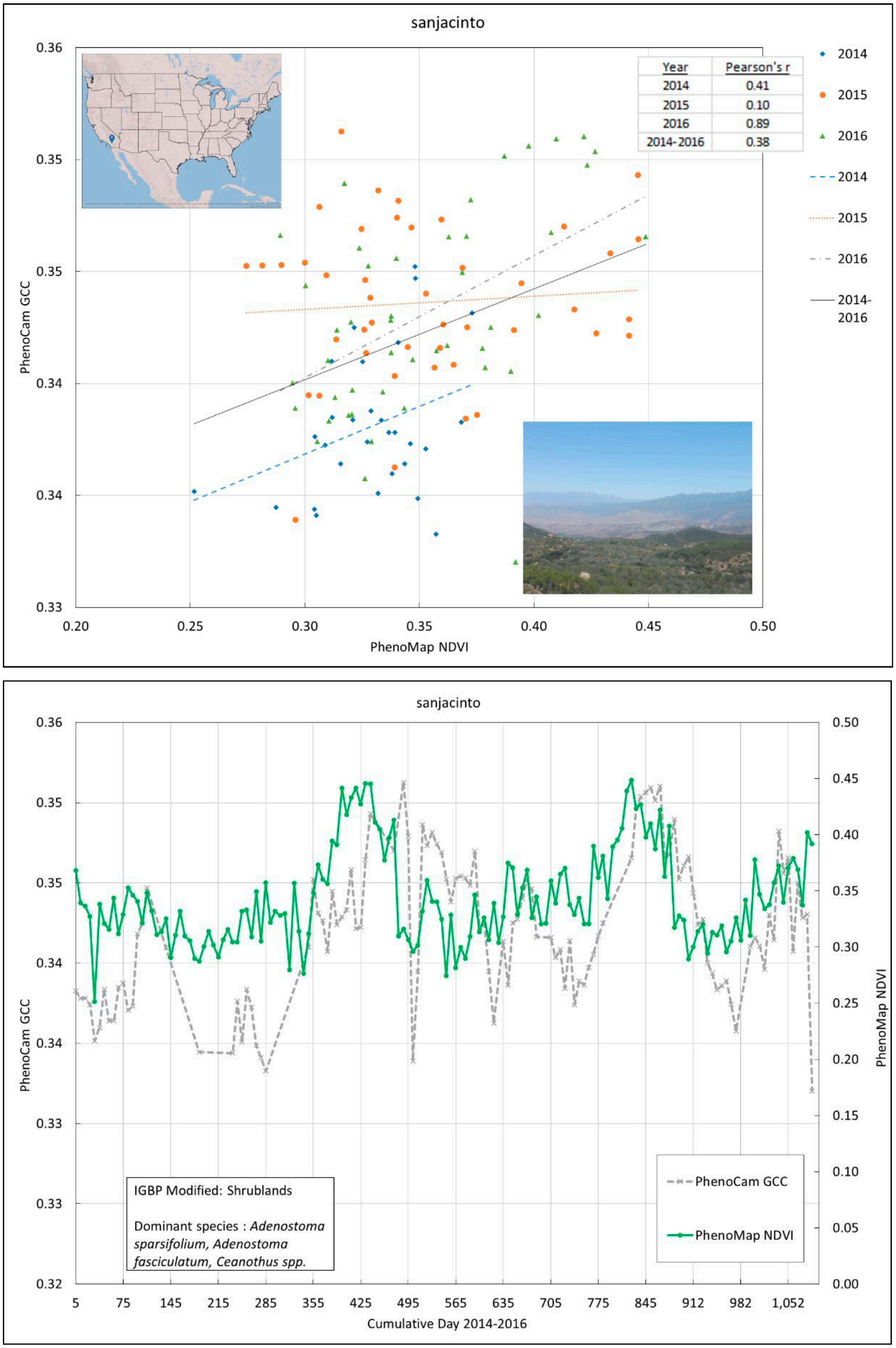


Figure 49—(A) Line graph and (B) scatterplot of the PhenoCam green chromatic coordinate ($gcc_{per90}$) and PhenoMap eMODIS NDVI weekly values 2014–2016 for the sanjacinto site. Inset graphics in the line graph show a representative PhenoCam image and a map showing the location of the site.

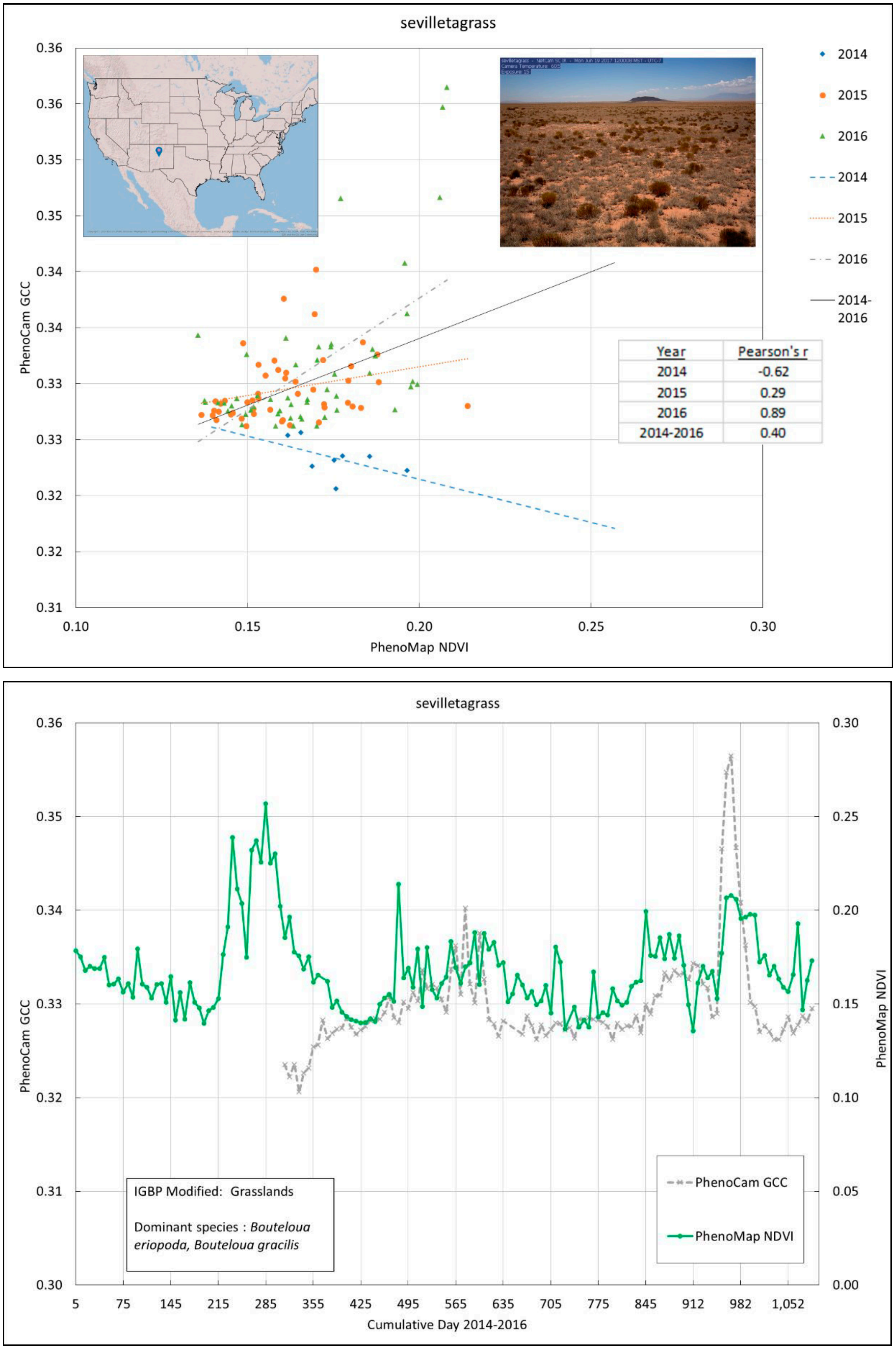


Figure 50—(A) Line graph and (B) scatterplot of the PhenoCam green chromatic coordinate ($gcc_{per90}$) and PhenoMap eMODIS NDVI weekly values 2014–2016 for the sevilletagrass site. Inset graphics in the line graph show a representative PhenoCam image and a map showing the location of the site.

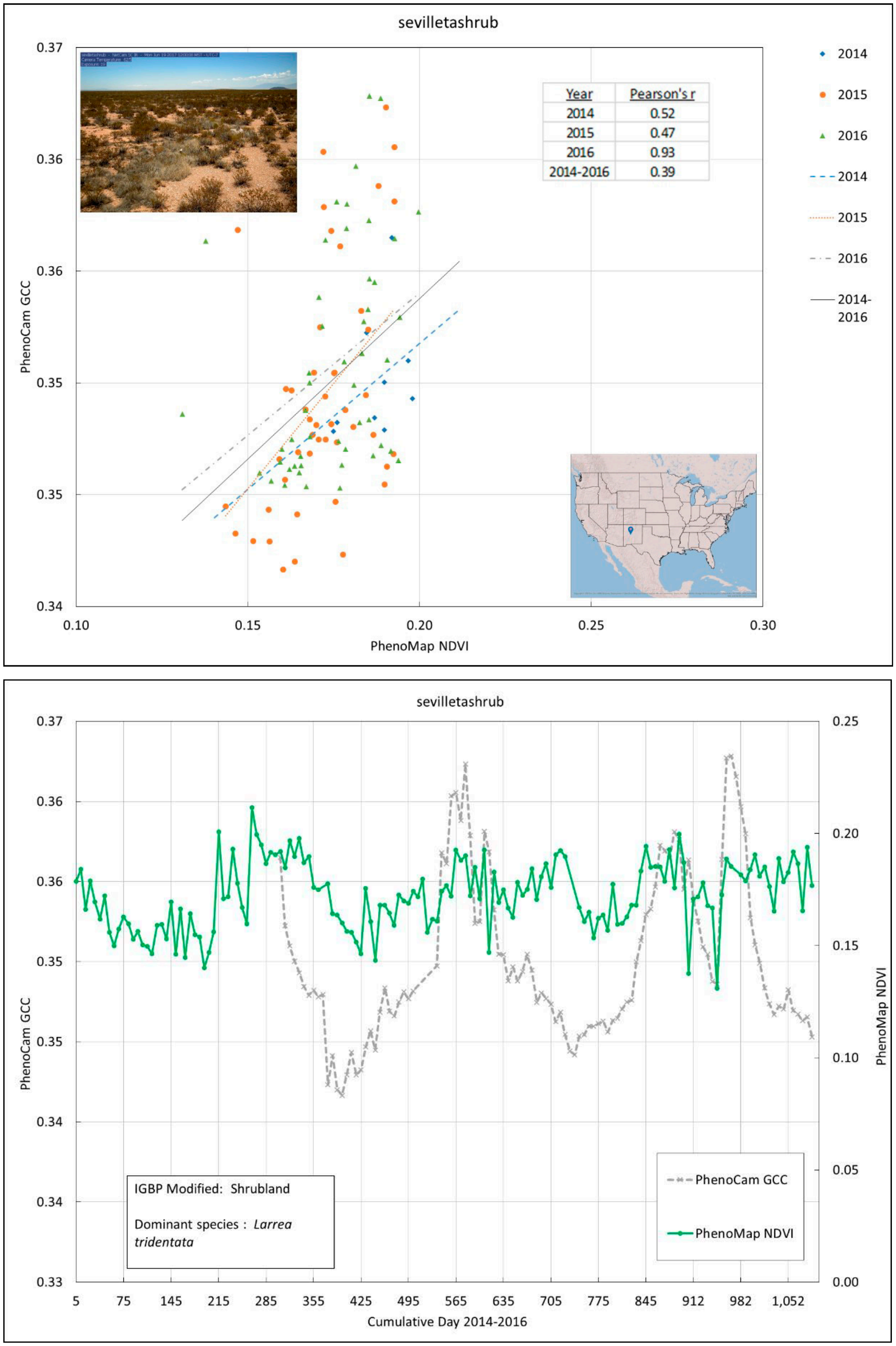


Figure 51—(A) Line graph and (B) scatterplot of the PhenoCam green chromatic coordinate ($gcc_{per90}$) and PhenoMap eMODIS NDVI weekly values 2014–2016 for the sevilletashrub site. Inset graphics in the line graph show a representative PhenoCam image and a map showing the location of the site.

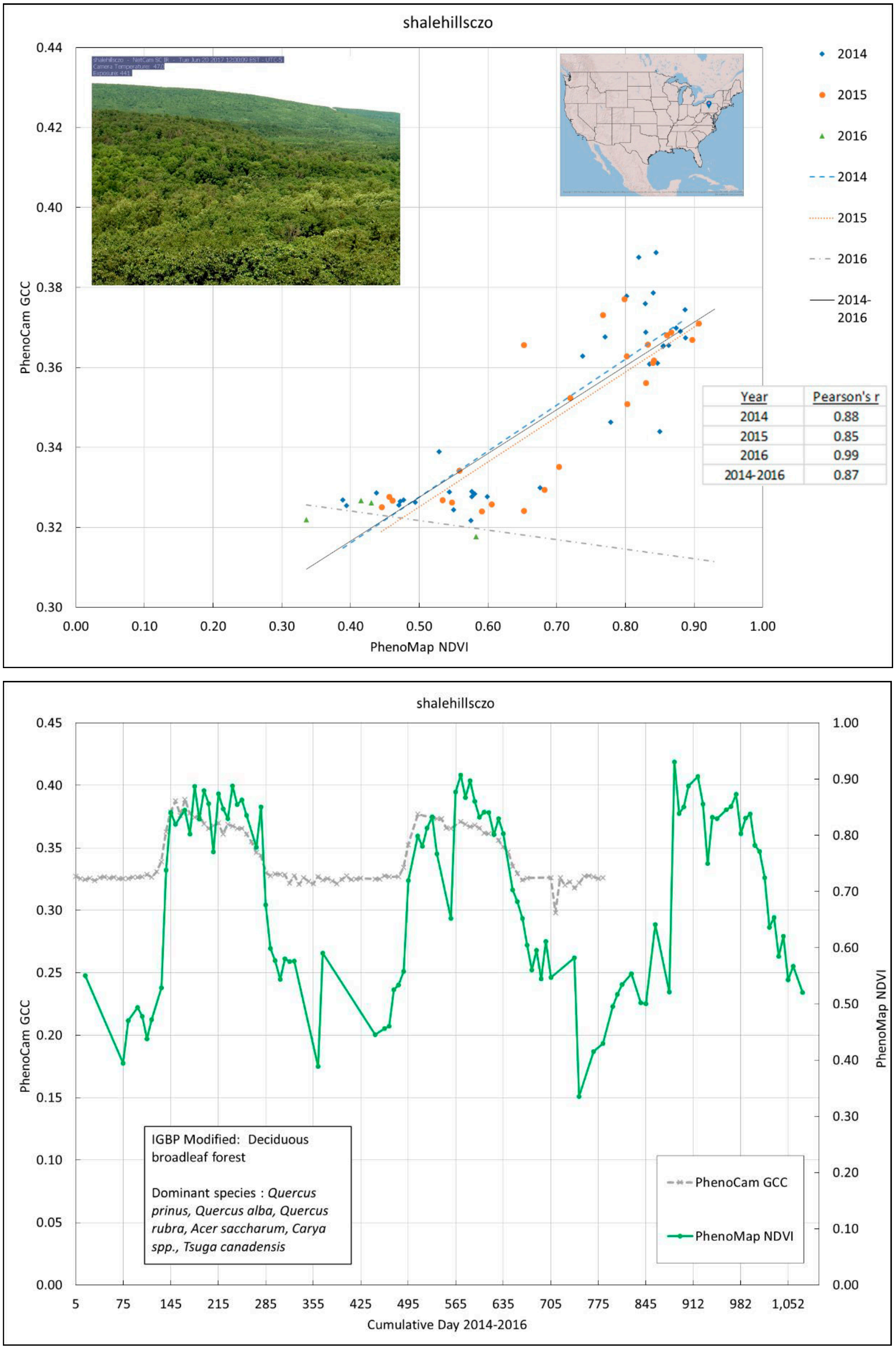


Figure 52—(A) Line graph and (B) scatterplot of the PhenoCam green chromatic coordinate ($gcc_{per90}$) and PhenoMap eMODIS NDVI weekly values 2014–2016 for the shalehillsczo site. Inset graphics in the line graph show a representative PhenoCam image and a map showing the location of the site.

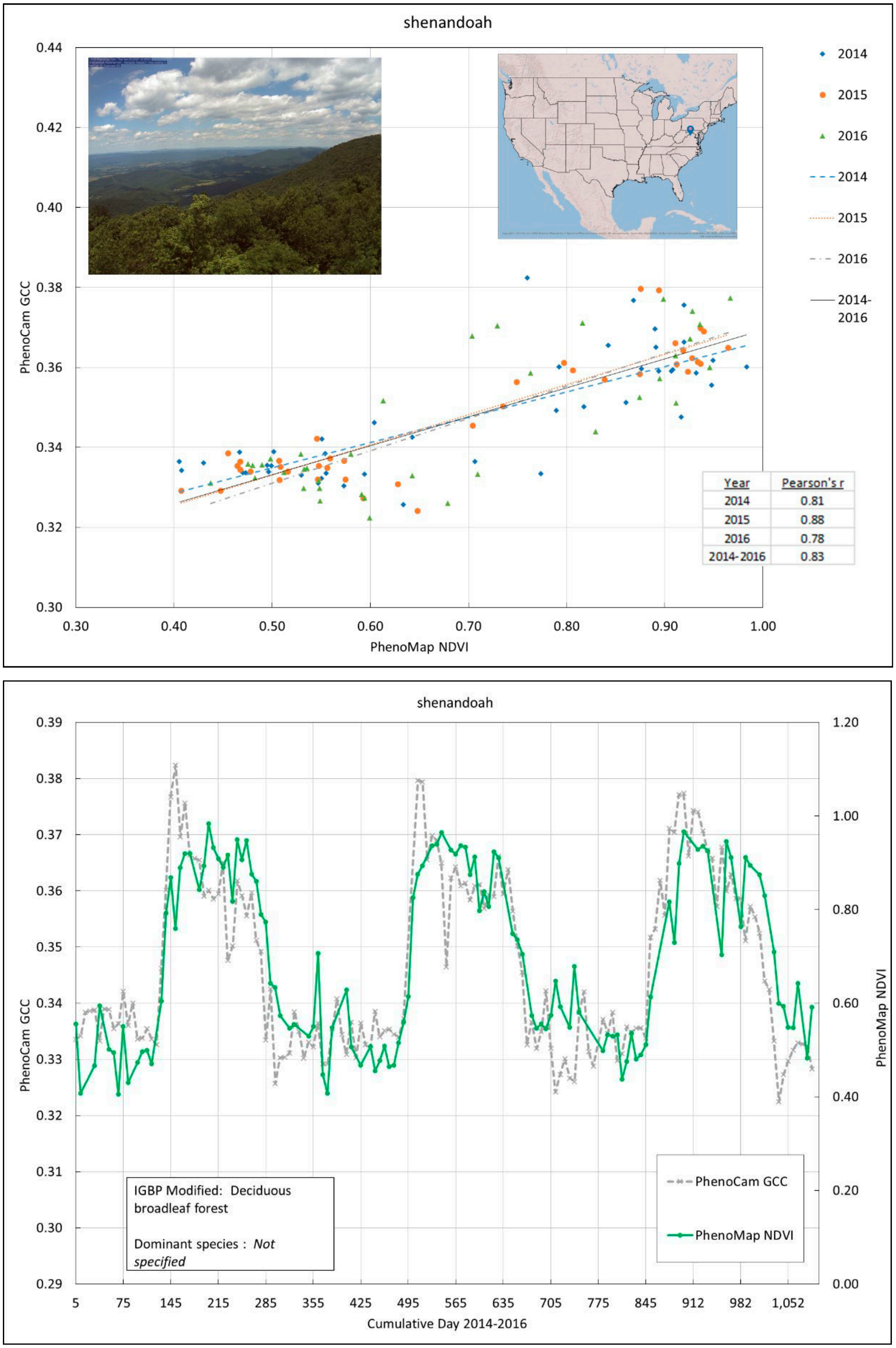


Figure 53—(A) Line graph and (B) scatterplot of the PhenoCam green chromatic coordinate ($gcc_{per90}$) and PhenoMap eMODIS NDVI weekly values 2014–2016 for the shenandoah site. Inset graphics in the line graph show a representative PhenoCam image and a map showing the location of the site.

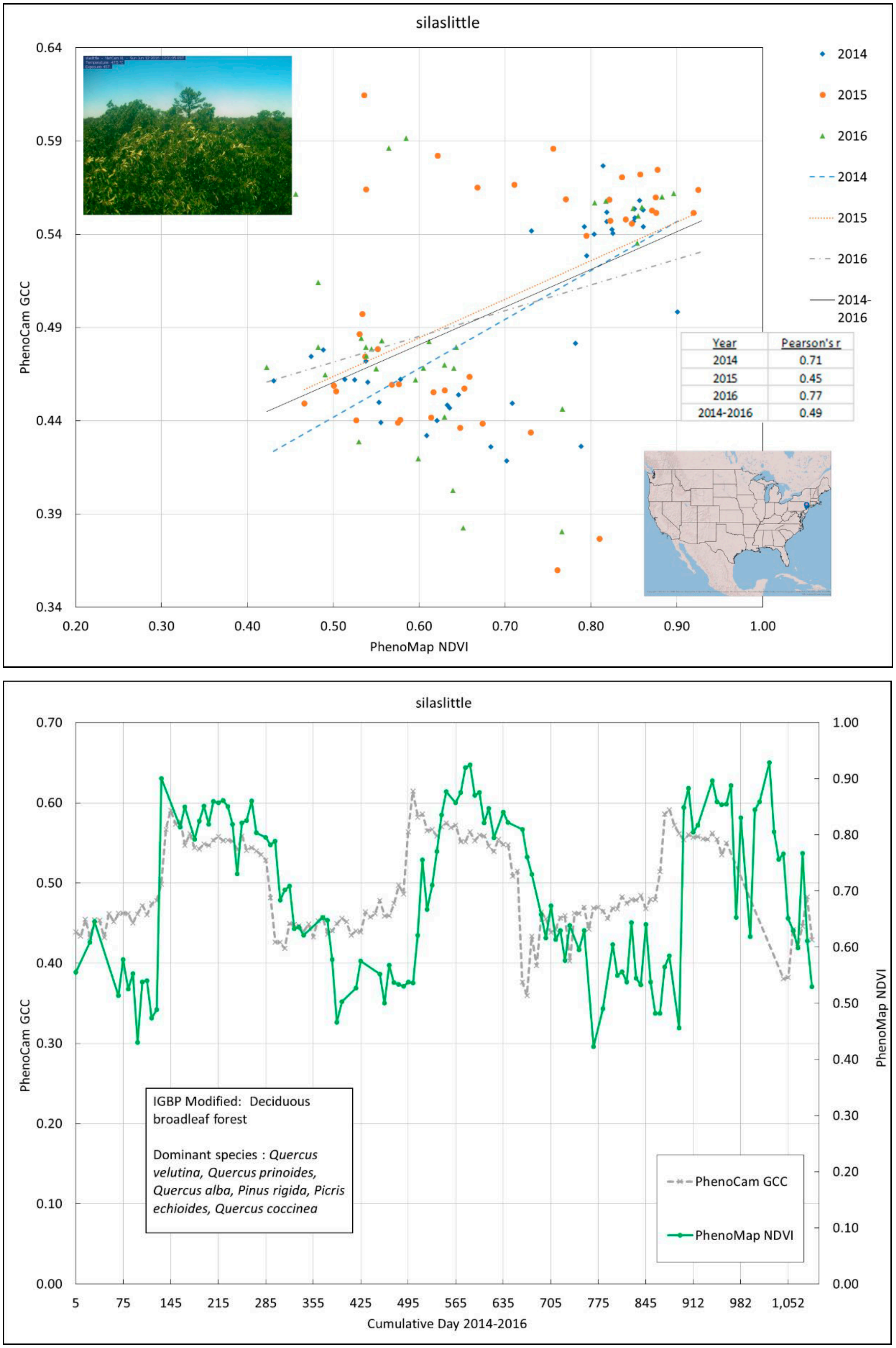


Figure 54—(A) Line graph and (B) scatterplot of the PhenoCam green chromatic coordinate ($gcc_{per90}$) and PhenoMap eMODIS NDVI weekly values 2014–2016 for the silaslittle site. Inset graphics in the line graph show a representative PhenoCam image and a map showing the location of the site.

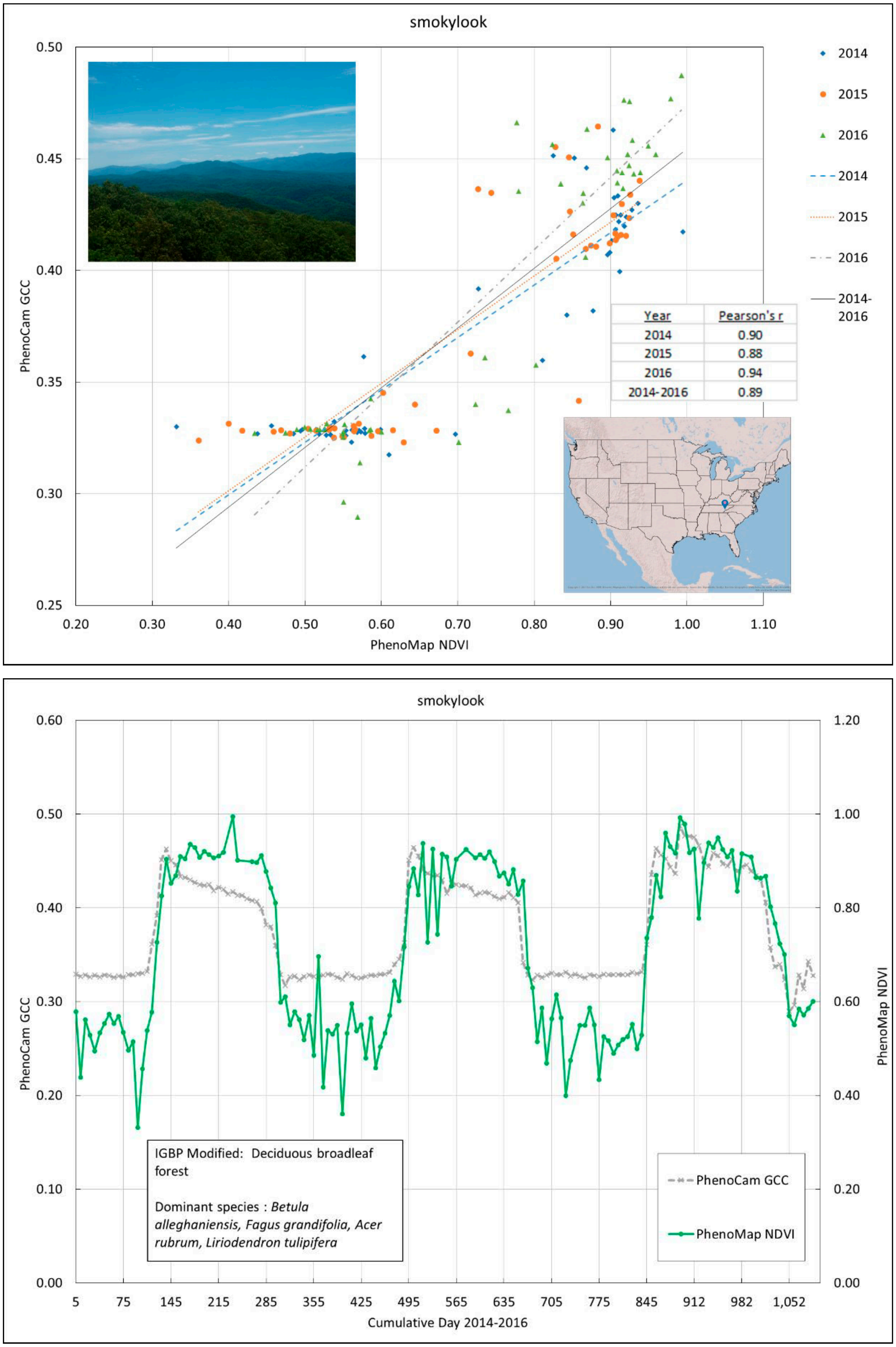


Figure 55—(A) Line graph and (B) scatterplot of the PhenoCam green chromatic coordinate ($gcc_{per90}$) and PhenoMap eMODIS NDVI weekly values 2014–2016 for the smokylook site. Inset graphics in the line graph show a representative PhenoCam image and a map showing the location of the site.

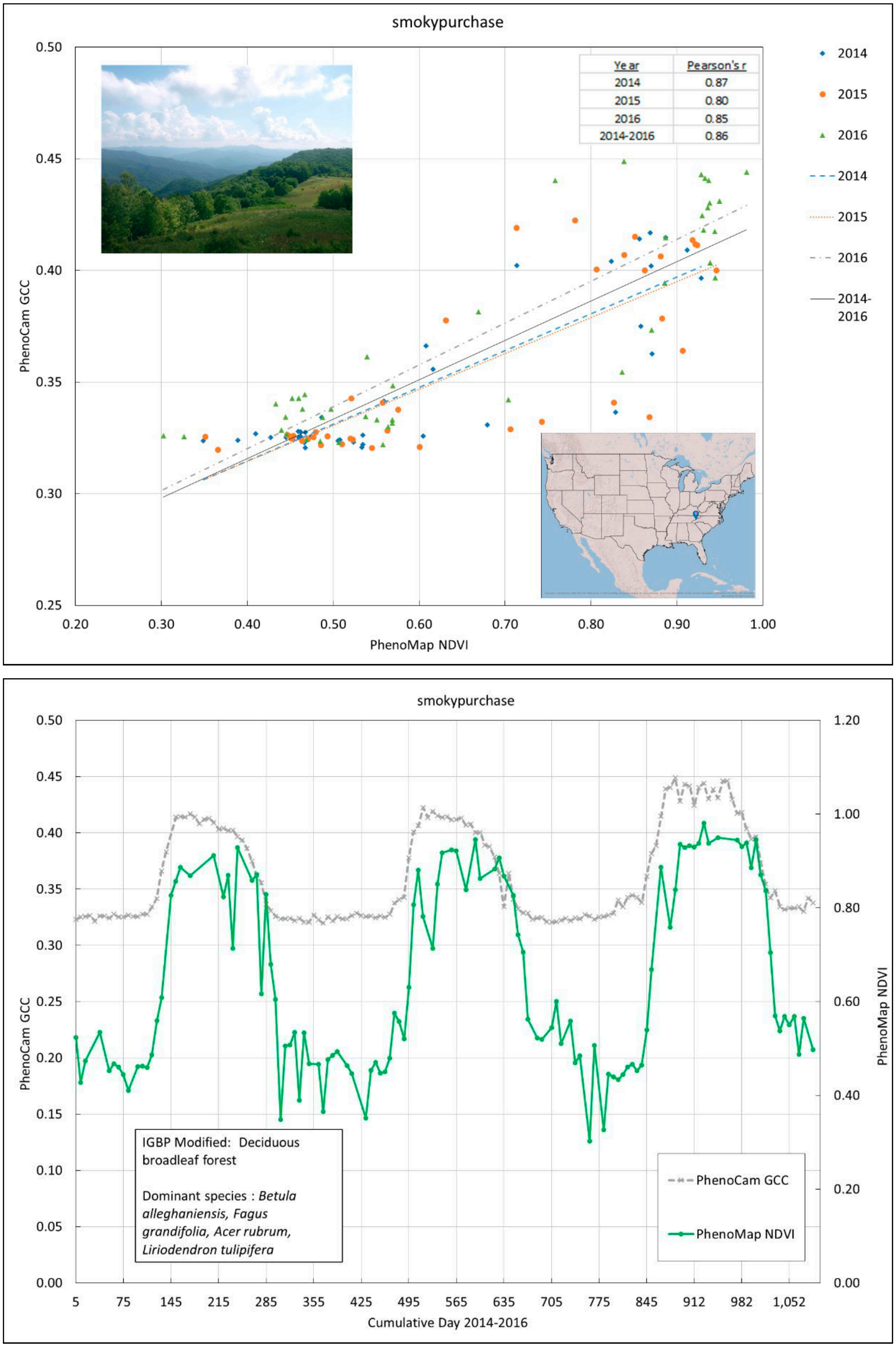


Figure 56—(A) Line graph and (B) scatterplot of the PhenoCam green chromatic coordinate ($gcc_{per90}$) and PhenoMap eMODIS NDVI weekly values 2014–2016 for the smokypurchase site. Inset graphics in the line graph show a representative PhenoCam image and a map showing the location of the site.

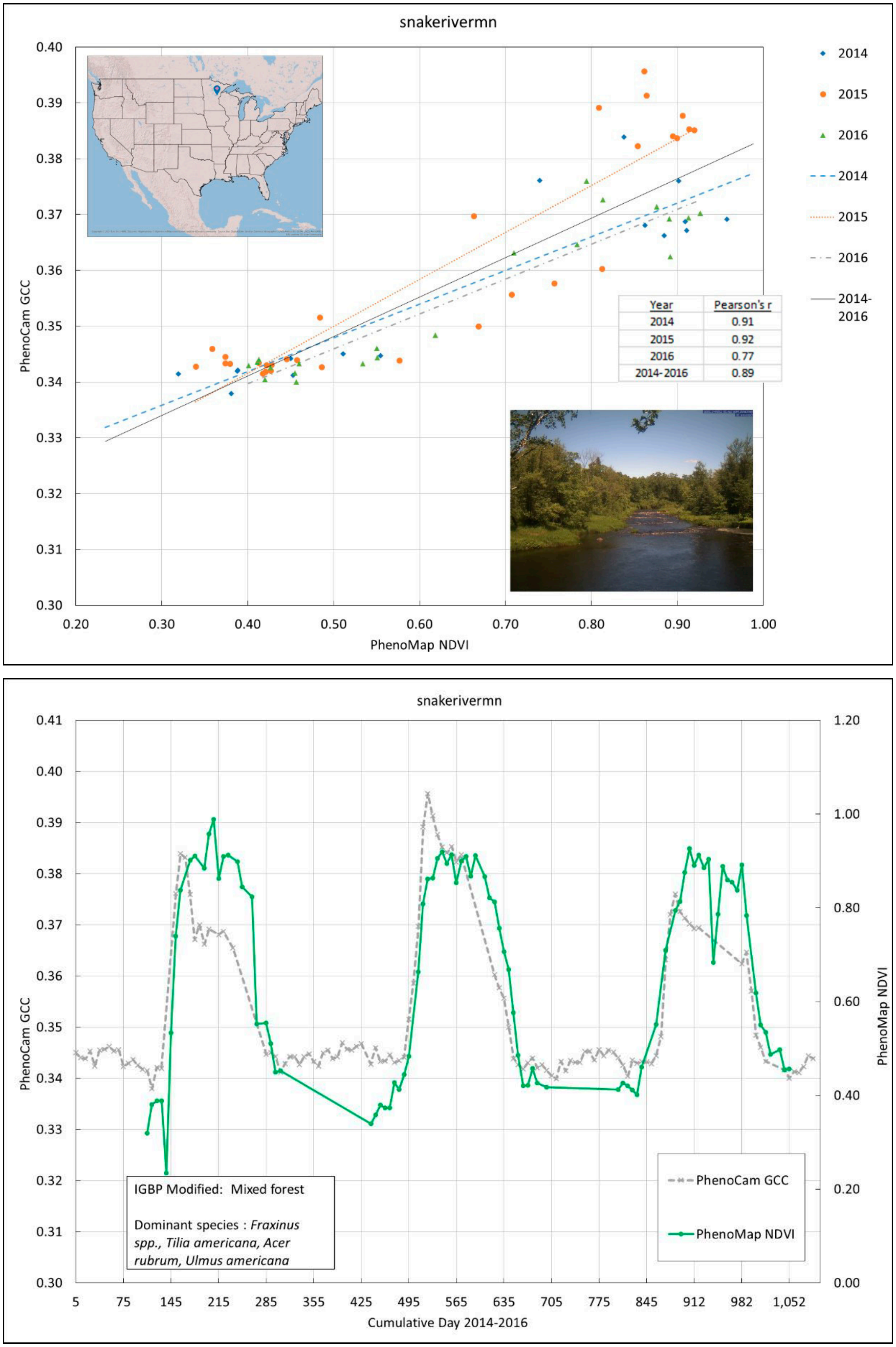


Figure 57—(A) Line graph and (B) scatterplot of the PhenoCam green chromatic coordinate ($gcc_{per90}$) and PhenoMap eMODIS NDVI weekly values 2014–2016 for the snakerivermn site. Inset graphics in the line graph show a representative PhenoCam image and a map showing the location of the site.

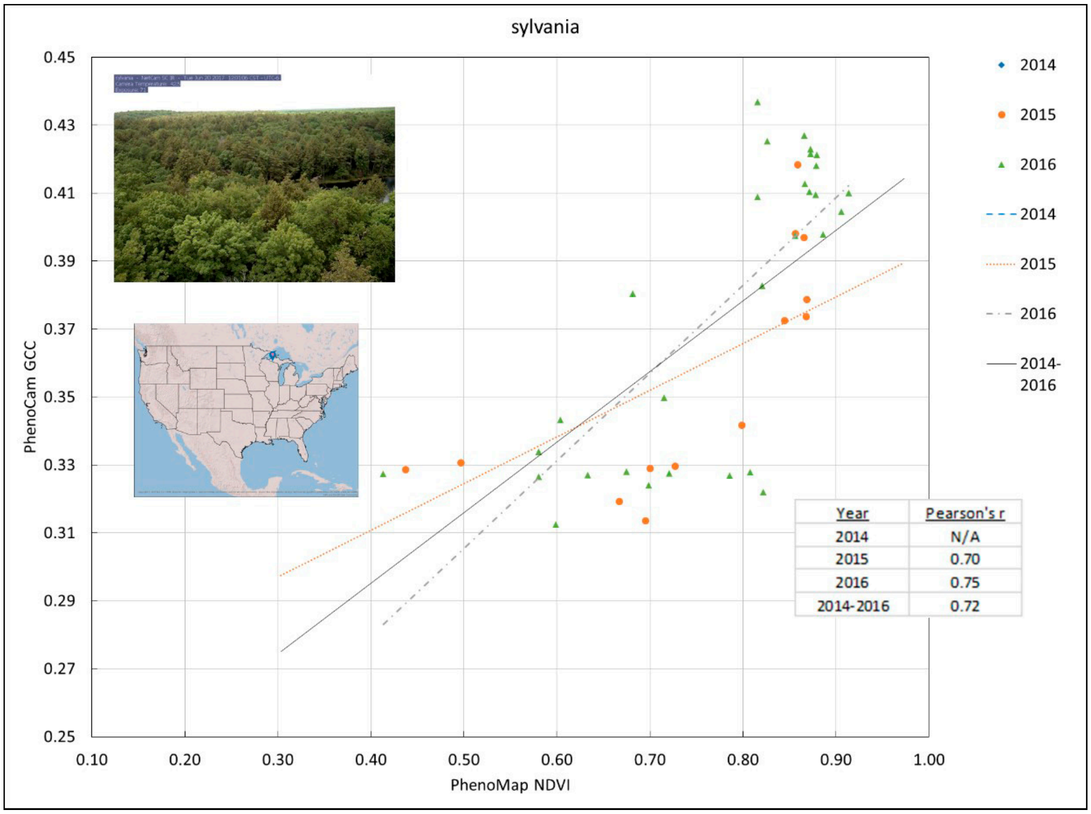


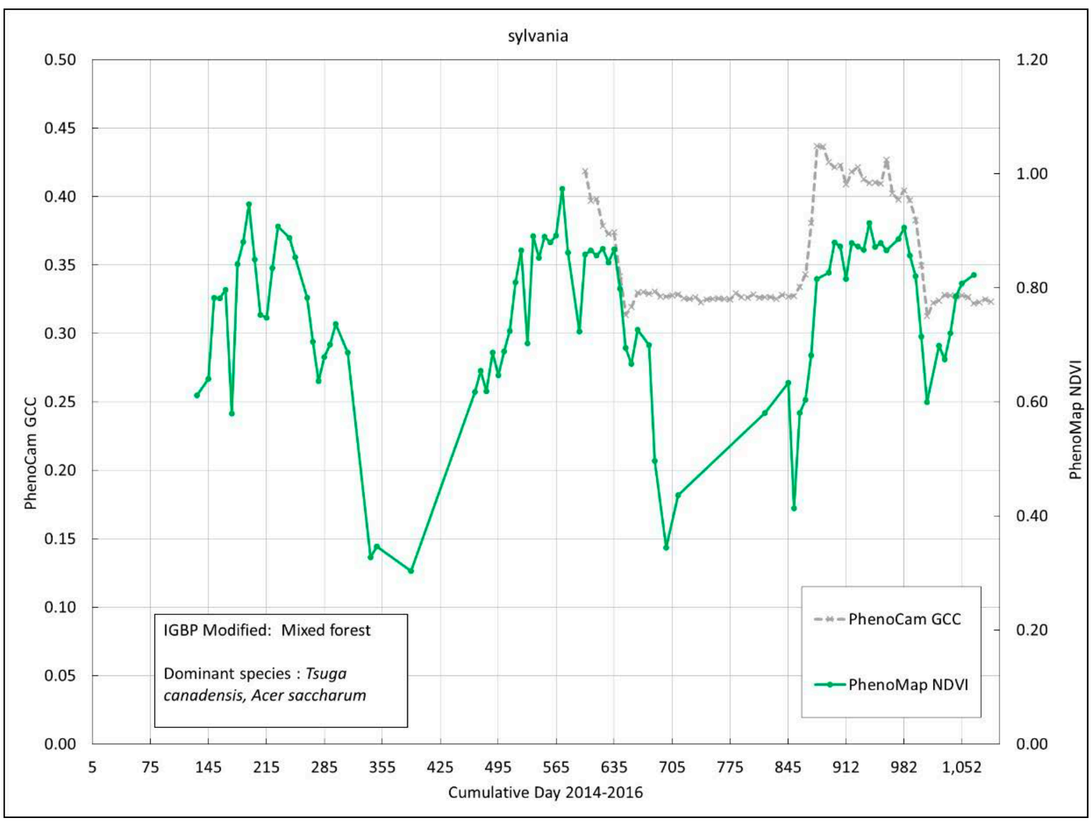


Figure 58—(A) Line graph and (B) scatterplot of the PhenoCam green chromatic coordinate ($gcc_{per90}$) and PhenoMap eMODIS NDVI weekly values 2014–2016 for the sylvania site. Inset graphics in the line graph show a representative PhenoCam image and a map showing the location of the site.

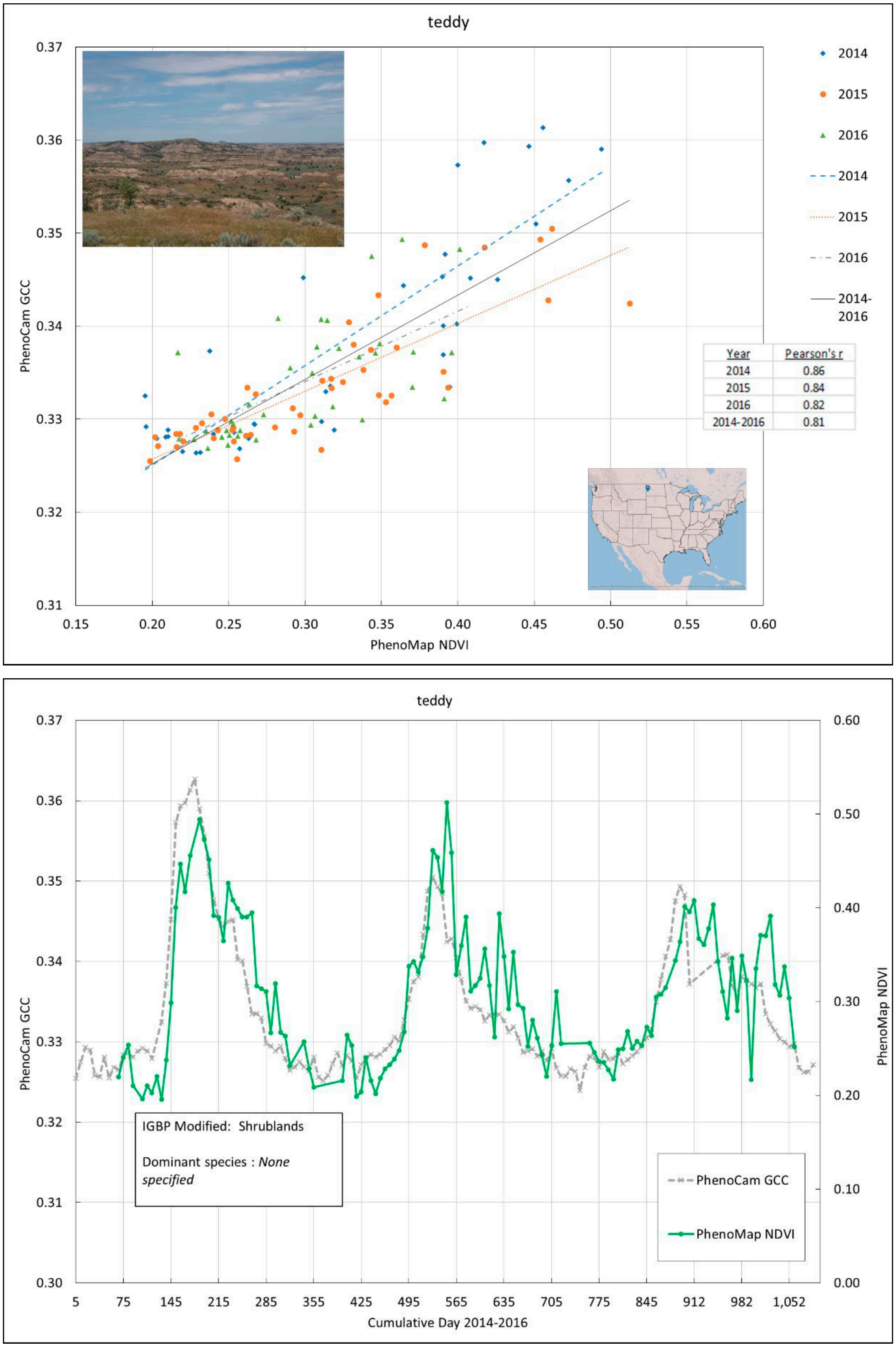


Figure 59—(A) Line graph and (B) scatterplot of the PhenoCam green chromatic coordinate ($gcc_{per90}$) and PhenoMap eMODIS NDVI weekly values 2014–2016 for the teddy site. Inset graphics in the line graph show a representative PhenoCam image and a map showing the location of the site.

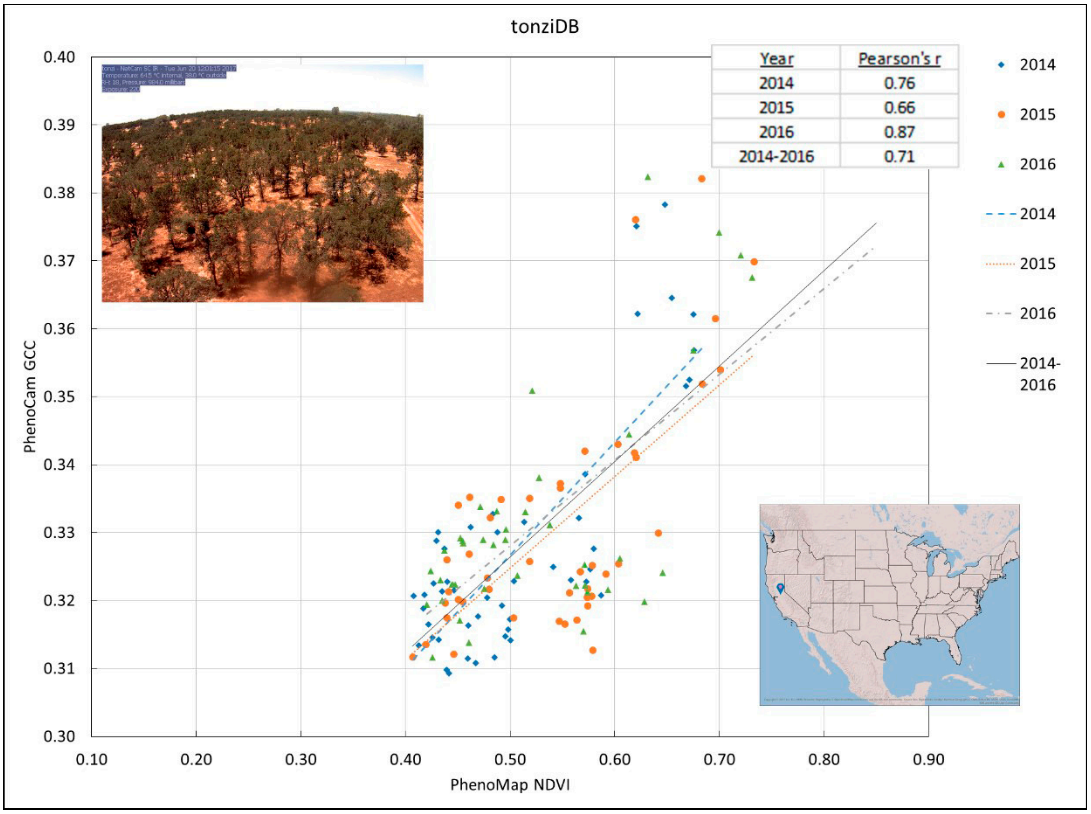


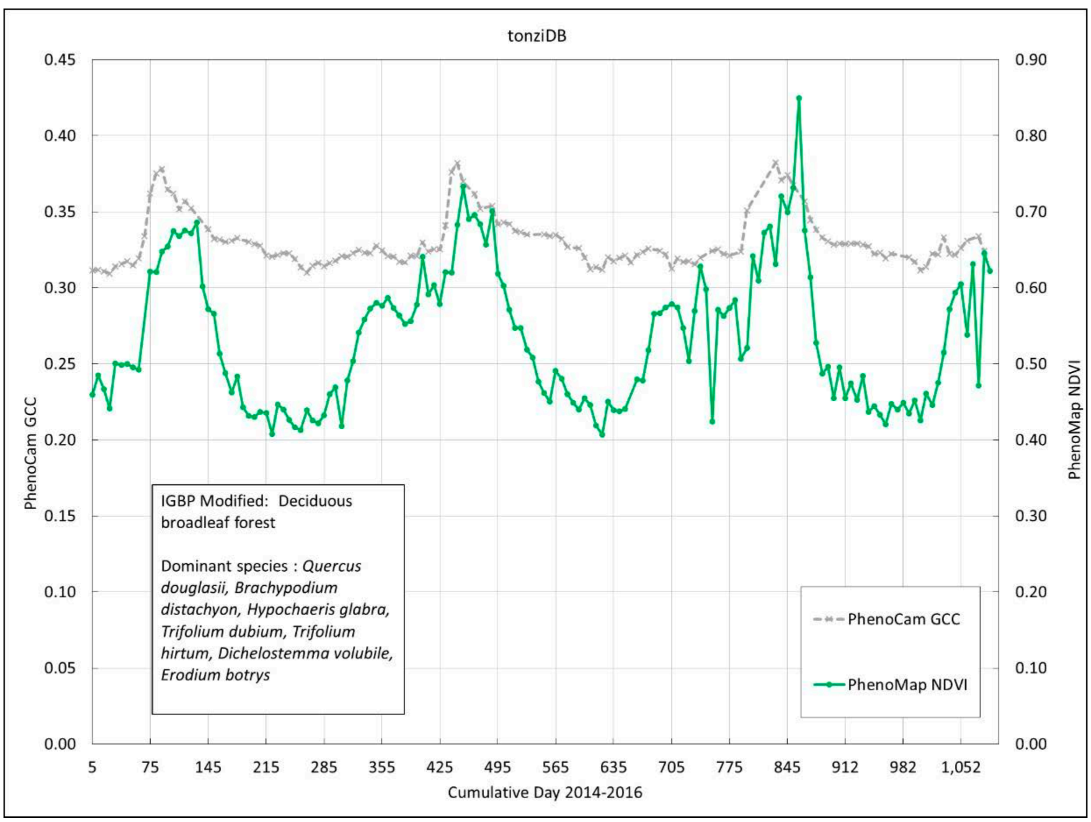


Figure 60—(A) Line graph and (B) scatterplot of the PhenoCam green chromatic coordinate ($gcc_{per90}$) and PhenoMap eMODIS NDVI weekly values 2014–2016 for the tonziDB site. Inset graphics in the line graph show a representative PhenoCam image and a map showing the location of the site.

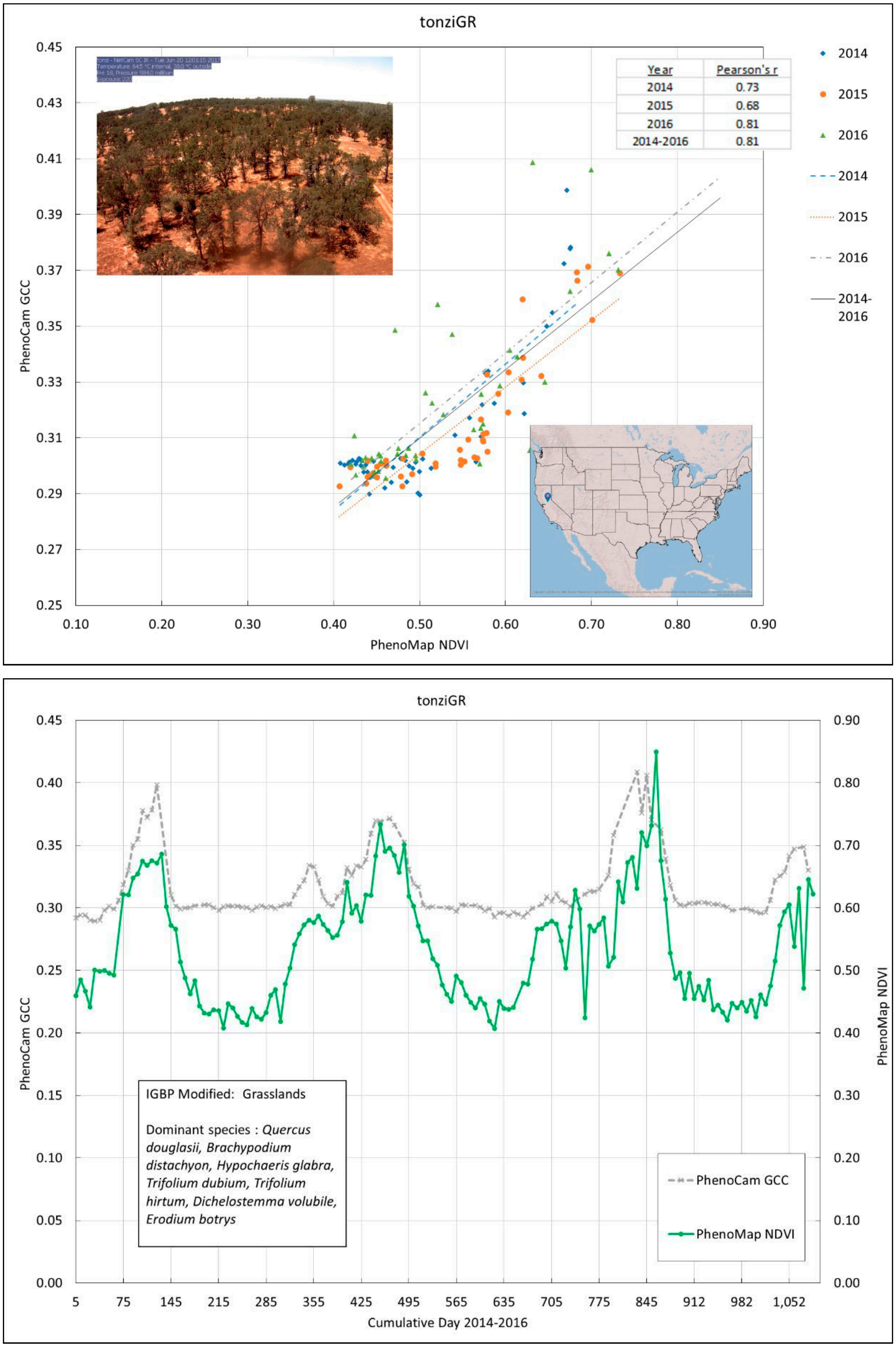


Figure 61—(A) Line graph and (B) scatterplot of the PhenoCam green chromatic coordinate ($gcc_{per90}$) and PhenoMap eMODIS NDVI weekly values 2014–2016 for the tonziGR site. Inset graphics in the line graph show a representative PhenoCam image and a map showing the location of the site.

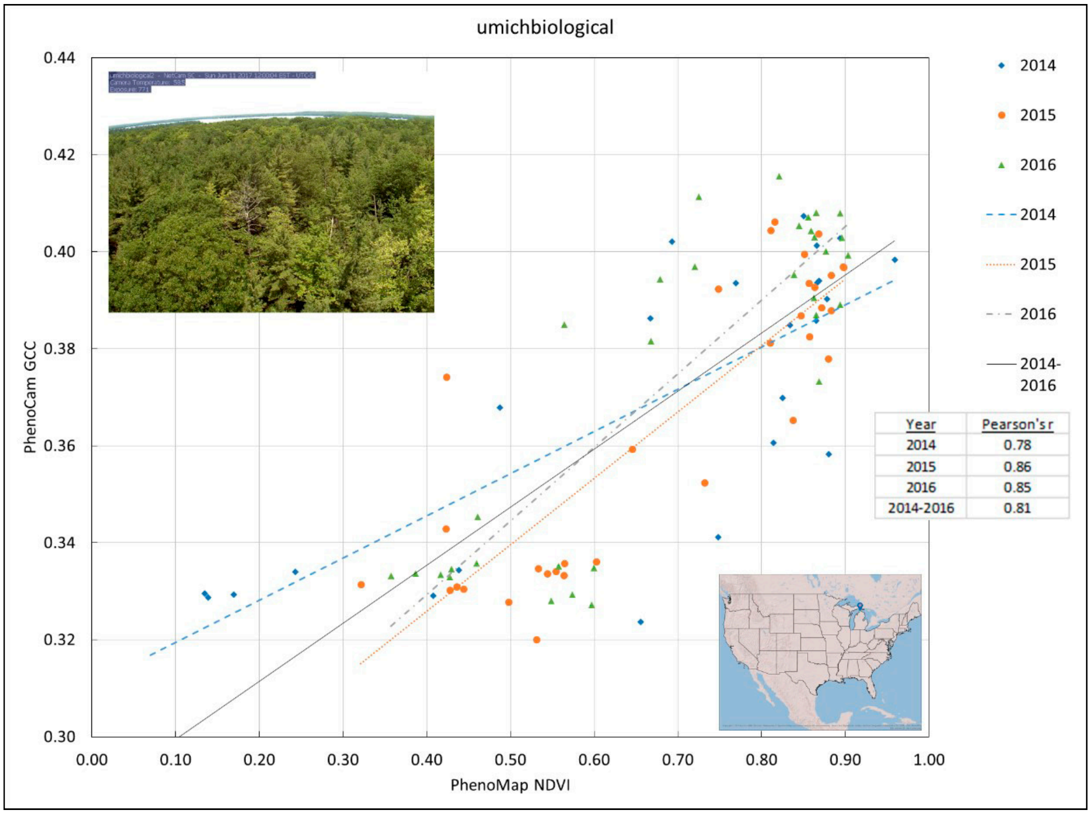


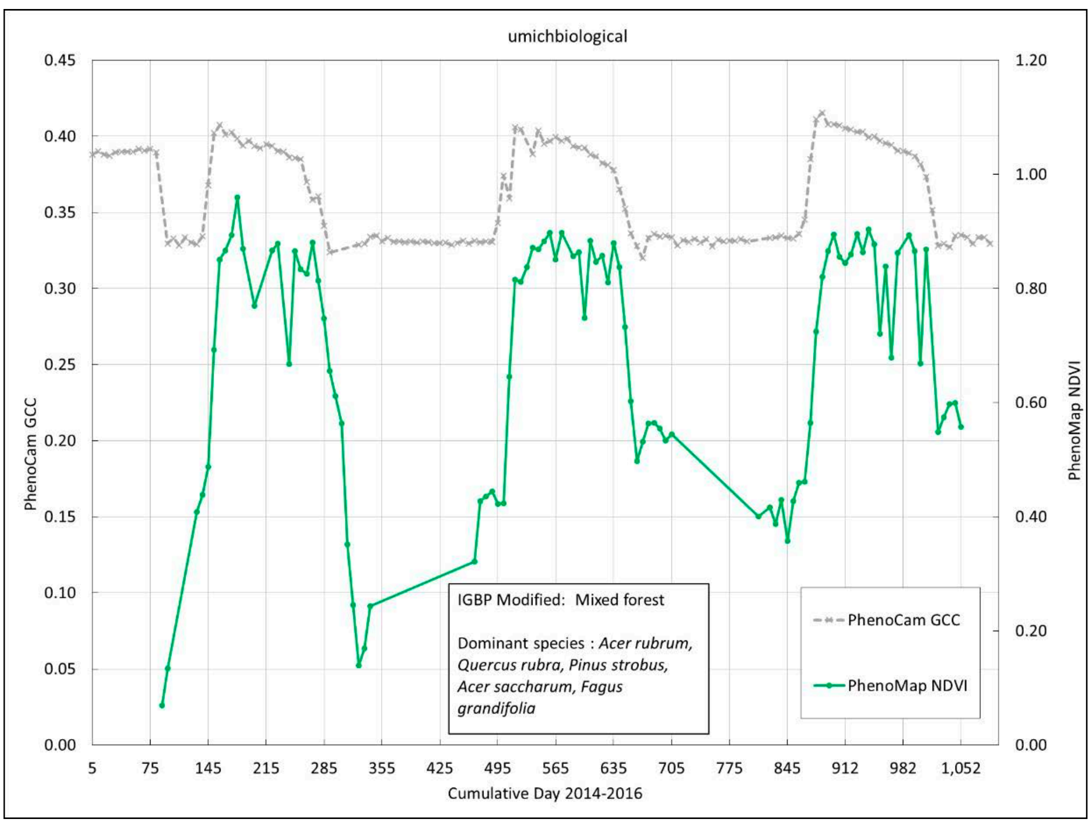


Figure 62—(A) Line graph and (B) scatterplot of the PhenoCam green chromatic coordinate ($gcc_{per90}$) and PhenoMap eMODIS NDVI weekly values 2014–2016 for the umichbiological site. Inset graphics in the line graph show a representative PhenoCam image and a map showing the location of the site.

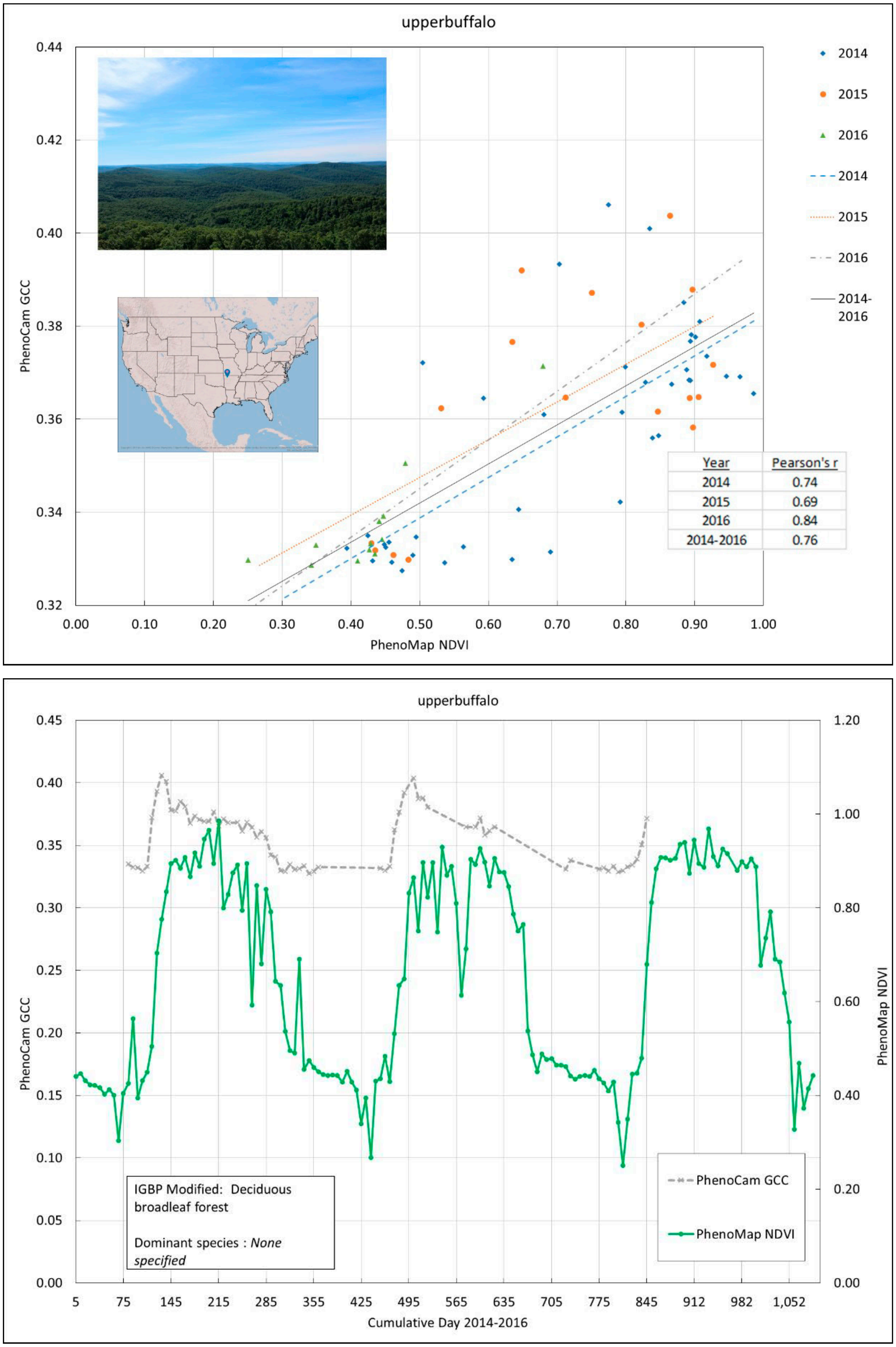


Figure 63—(A) Line graph and (B) scatterplot of the PhenoCam green chromatic coordinate ($gcc_{per90}$) and PhenoMap eMODIS NDVI weekly values 2014–2016 for the upperbuffalo site. Inset graphics in the line graph show a representative PhenoCam image and a map showing the location of the site.

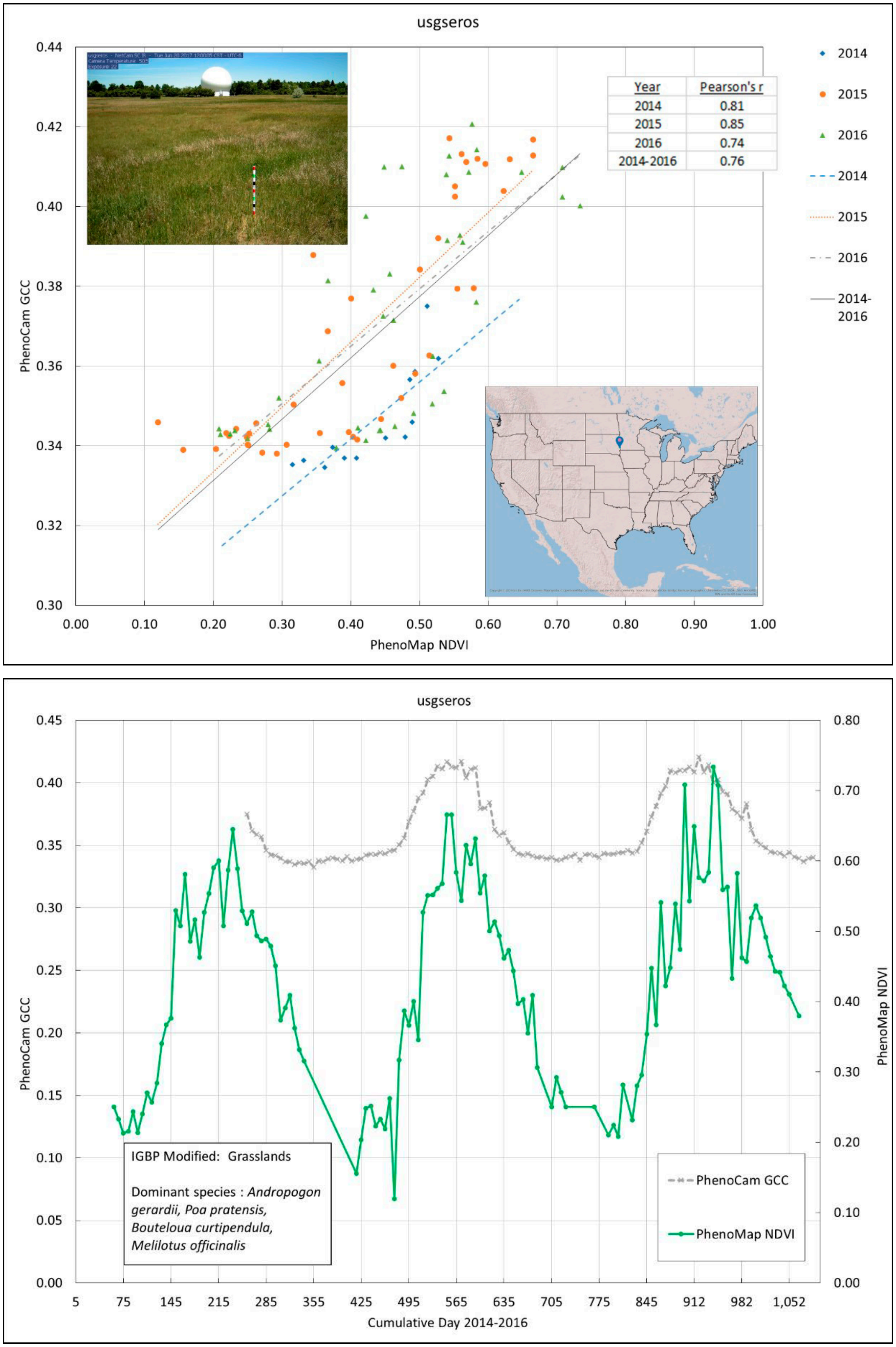


Figure 64—(A) Line graph and (B) scatterplot of the PhenoCam green chromatic coordinate ($gcc_{per90}$) and PhenoMap eMODIS NDVI weekly values 2014–2016 for the usgseros site. Inset graphics in the line graph show a representative PhenoCam image and a map showing the location of the site.

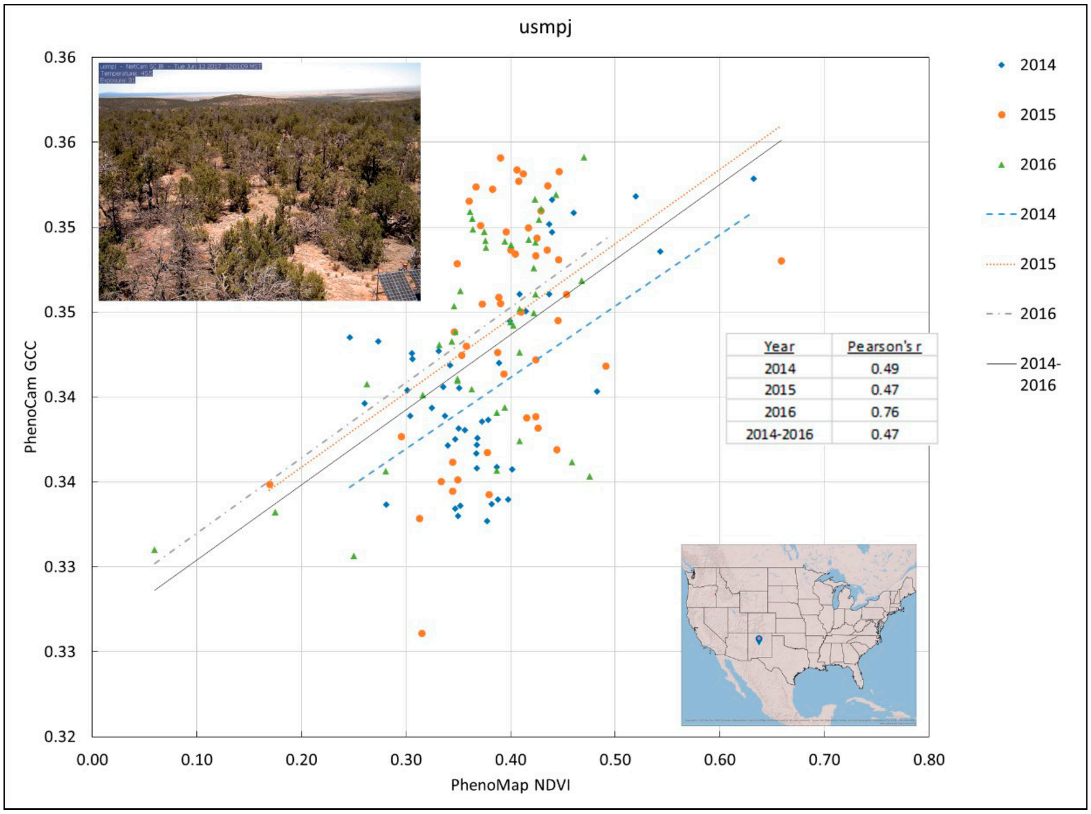


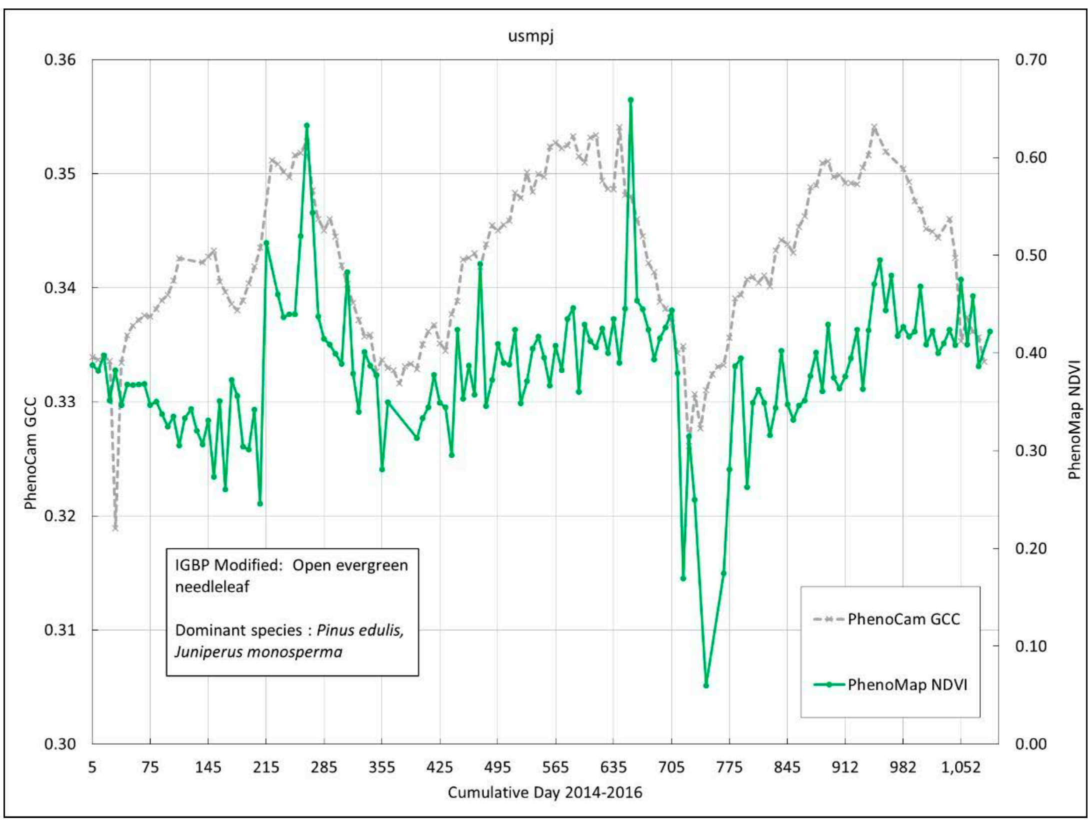


Figure 65—(A) Line graph and (B) scatterplot of the PhenoCam green chromatic coordinate ($gcc_{per90}$) and PhenoMap eMODIS NDVI weekly values 2014–2016 for the usmpj site. Inset graphics in the line graph show a representative PhenoCam image and a map showing the location of the site.

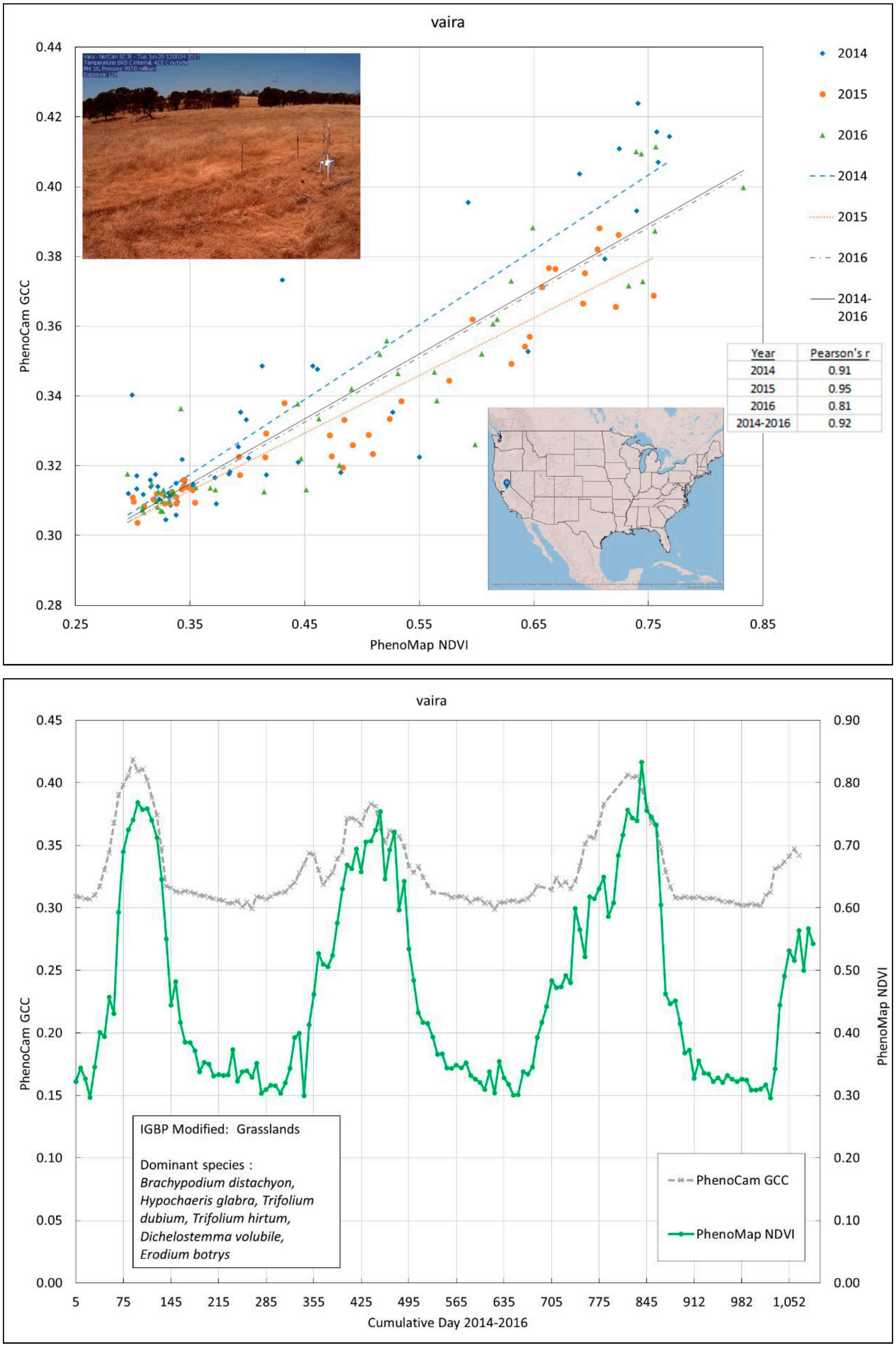


Figure 66—(A) Line graph and (B) scatterplot of the PhenoCam green chromatic coordinate ($gcc_{per90}$) and PhenoMap eMODIS NDVI weekly values 2014–2016 for the vaira site. Inset graphics in the line graph show a representative PhenoCam image and a map showing the location of the site.

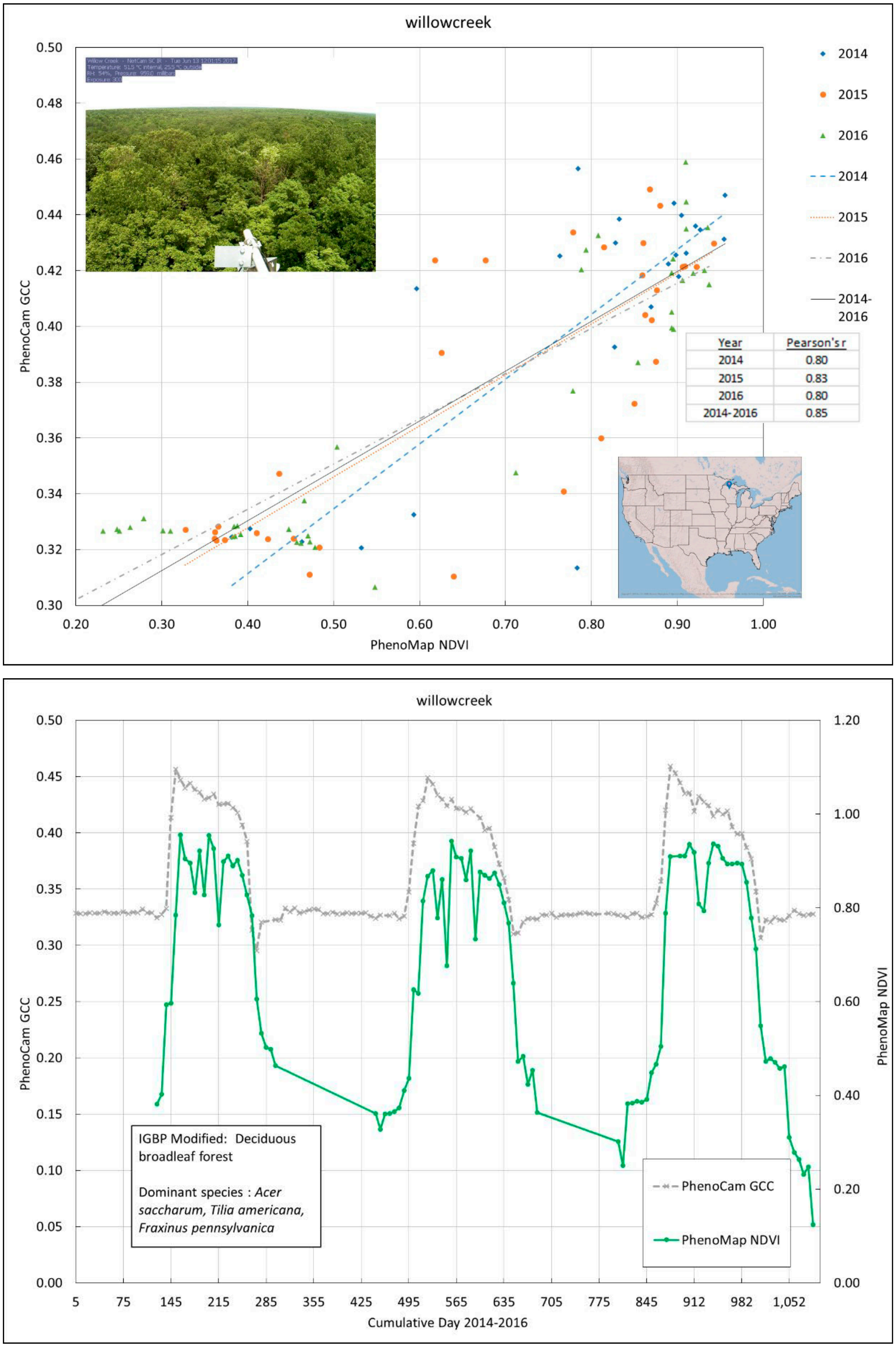


Figure 67—(A) Line graph and (B) scatterplot of the PhenoCam green chromatic coordinate ($gcc_{per90}$) and PhenoMap eMODIS NDVI weekly values 2014–2016 for the willowcreek site. Inset graphics in the line graph show a representative PhenoCam image and a map showing the location of the site.

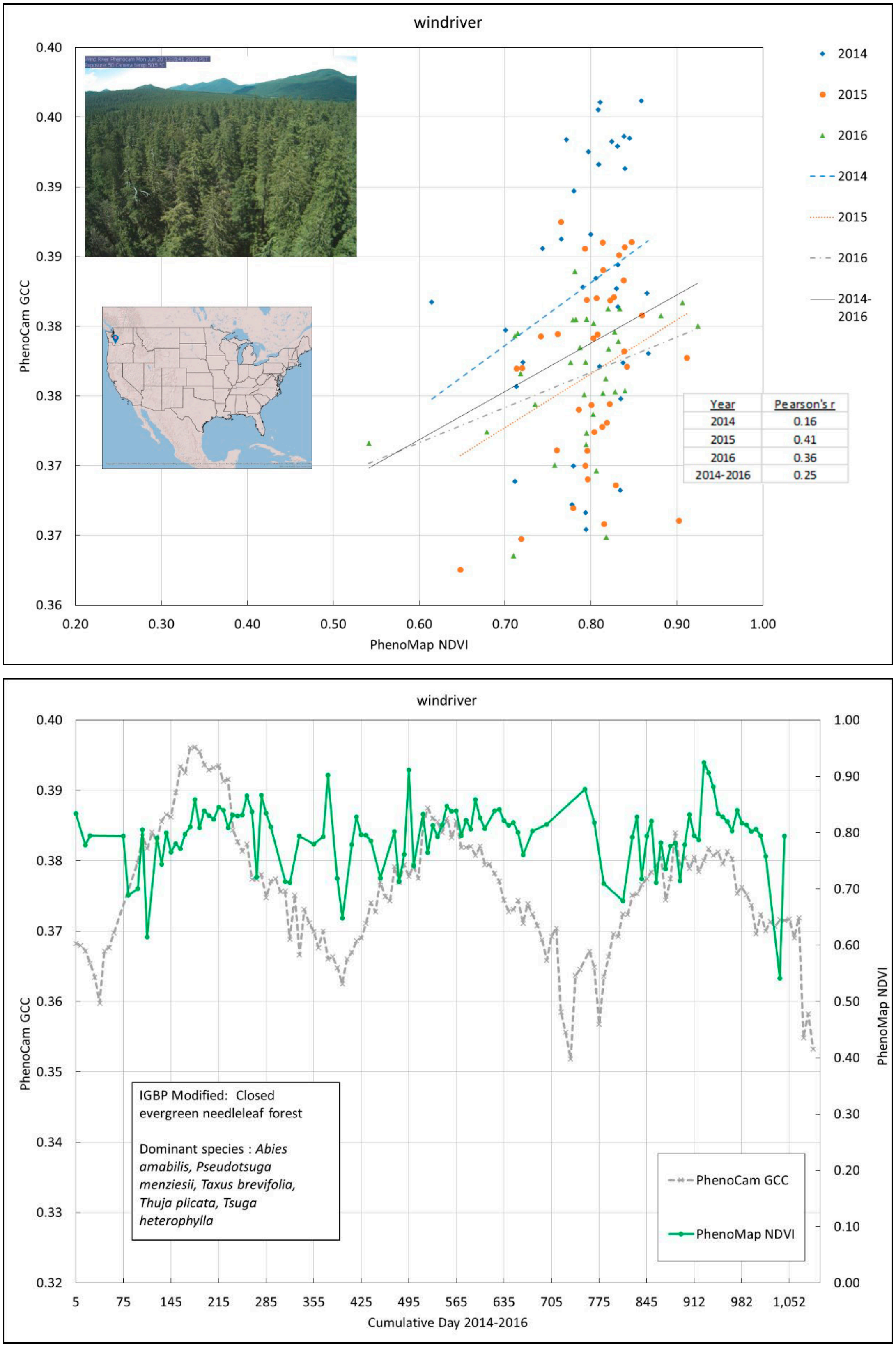


Figure 68—(A) Line graph and (B) scatterplot of the PhenoCam green chromatic coordinate ($gcc_{per90}$) and PhenoMap eMODIS NDVI weekly values 2014–2016 for the windriver site. Inset graphics in the line graph show a representative PhenoCam image and a map showing the location of the site.

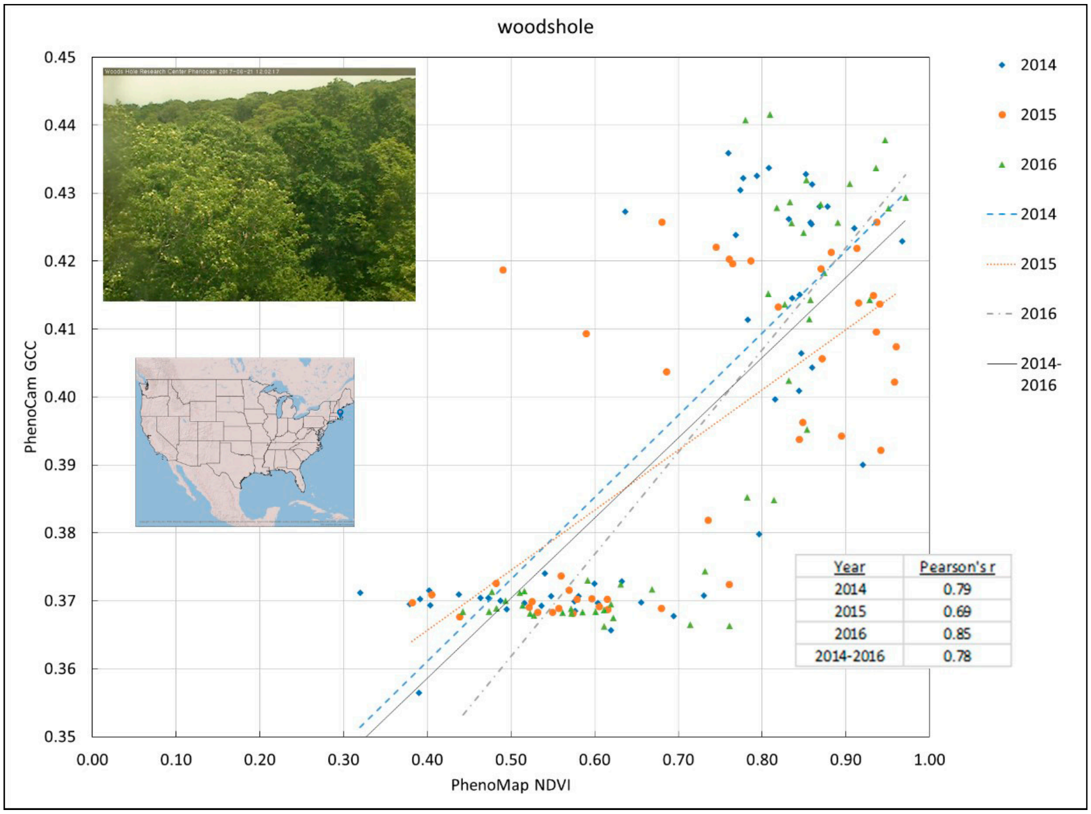


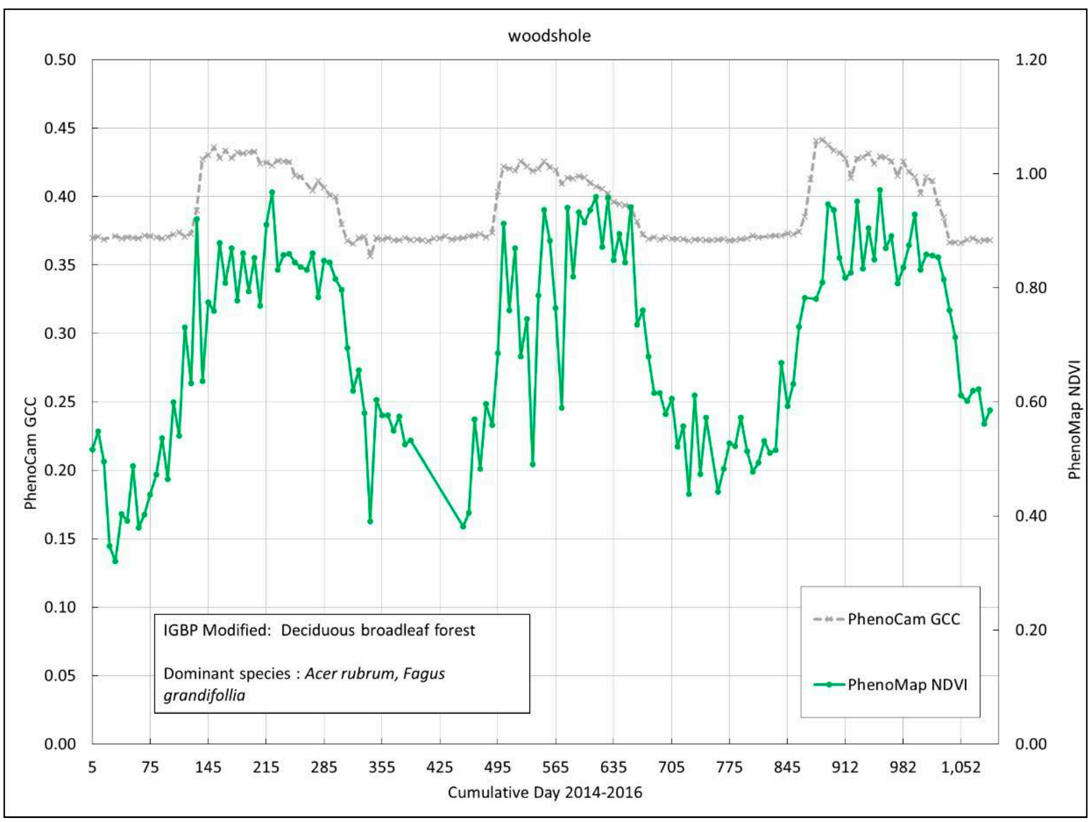


Figure 69—(A) Line graph and (B) scatterplot of the PhenoCam green chromatic coordinate ($gcc_{per90}$) and PhenoMap eMODIS NDVI weekly values 2014–2016 for the woodshole site. Inset graphics in the line graph show a representative PhenoCam image and a map showing the location of the site.

# Appendix 2: Regression Statistics

### PhenoCam GCC–PhenoMap Normalized Differential Vegetation Index linear regression statistics for the PhenoCam sites

| PhenoCam site | IGBP class[a] | Pearson's r | Intercept | Slope | p significance |
|---|---|---|---|---|---|
| alligatorriver | MXF | 0.7798 | -0.06531 | 2.05349 | p < 0.001 |
| breckenridge | ONF | -0.0886 | 1.055 | -1.22 | p >.1 |
| bullshoals | GR | 0.8088072 | -0.84646 | 4.19281 | p < .001 |
| burnssagebrush | SH | 0.5876511 | -1.2523 | 4.2685 | p < .001 |
| butte | GR | 0.5243214 | -0.26252 | 1.58352 | p < .001 |
| coweeta | DBF | 0.8101415 | -0.19113 | 2.32222 | p < .001 |
| cperuvb | GR | 0.5879581 | -1.3951 | 4.9589 | p < .001 |
| downerwoods | DBF | 0.8332388 | -0.88129 | 3.55332 | p < .001 |
| eastend | GR | 0.871243 | -1.2296 | 4.7444 | p < .001 |
| grandrivergrass | GR | 0.7466752 | -0.7815 | 4.1121 | p < .001 |
| grandteton | SH | 0.3587737 | -0.3284 | 2.2211 | .05 > p > .01 |
| hartprairie | GR | 0.5422859 | -0.9091 | 3.9321 | p < .001 |
| howland2 | MXF | 0.5883375 | -0.05578 | 2.14296 | p < .001 |
| hubbardbrook | DBF | 0.8816119 | -2.5405 | 8.4299 | p < .001 |
| ibp | SH | 0.8103008 | -1.7168 | 5.5834 | p < .001 |
| jasperridge | GR | 0.7353189 | -0.63064 | 3.38358 | p < .001 |
| jerbajada | SH | 0.6121171 | -1.0293 | 3.7167 | p < .001 |
| jernort | SH | 0.8582424 | -0.39814 | 1.65123 | p < .001 |
| jersand | SH | 0.747384 | -2.1546 | 7.2598 | p < .001 |
| kansas | GR | 0.8172054 | -0.79007 | 3.66974 | p < .001 |
| kendall | GR | 0.8338026 | -1.7475 | 5.6495 | p < .001 |
| konza | GR | 0.8494196 | -0.84132 | 3.78145 | p < .001 |
| lostcreek | SH | 0.793014 | -1.58 | 6.0335 | p < .001 |
| luckyhills | SH | 0.5949769 | -0.67867 | 2.66313 | p < .001 |
| mammothcave | DBF | 0.8893869 | -0.92289 | 4.22526 | p < .001 |
| marena | GR | 0.8556756 | -0.89089 | 4.11514 | p < .001 |
| morganmonroe | DBF | 0.9180516 | -2.6333 | 9.3411 | p < .001 |
| niwot2 | CNF | -0.1065967 | 1.1161 | -0.9534 | p > .1 |
| oakridge2 | DBF | 0.7942924 | -3.4241 | 11.7633 | p < .001 |
| oregonMP | ONF | -0.05005694 | 0.8496 | -0.327 | p > .1 |
| oregonYP | ONF | 0.01890215 | 0.4281 | 0.1573 | p > .1 |
| quickbird | SH | 0.7038254 | -1.1286 | 3.9741 | p < .001 |
| rosemountnprs | GR | 0.2747173 | 0.3901 | 0.7645 | .1 > p > .05 |
| sanjacinto | SH | 0.3772128 | -0.8519 | 3.5041 | p < .001 |
| sevilletagrass | GR | 0.3978219 | -0.27279 | 1.3283 | p < .001 |
| sevilletashrub | SH | 0.3907543 | -0.19751 | 1.0628 | p < .001 |
| shalehillsczo | DBF | 0.8653079 | -1.6955 | 6.8417 | p < .001 |
| shenandoah | DBF | 0.8341667 | -2.6408 | 9.6031 | p < .001 |
| silaslittle | DBF | 0.4938502 | 0.08123 | 1.20893 | p < .001 |

**PhenoCam GCC–PhenoMap Normalized Differential Vegetation Index linear regression statistics for the PhenoCam sites (continued)**

| PhenoCam site | IGBP class[a] | Pearson's r | Intercept | Slope | p significance |
|---|---|---|---|---|---|
| smokylook | DBF | 0.8939292 | -0.41529 | 2.98707 | p < .001 |
| smokypurchase | DBF | 0.8575161 | -0.8515 | 4.1684 | p < .001 |
| snakerivermn | MXF | 0.8935441 | -3.408 | 11.2985 | p < .001 |
| sylvania | MXF | 0.7214923 | -0.1687 | 2.502 | p < .001 |
| teddy | SH | 0.8098111 | -2.1143 | 7.2308 | p < .001 |
| tonziDB | DBF | 0.7104039 | -0.6587 | 3.5896 | p < .001 |
| tonziGR | GR | 0.8079947 | -0.31166 | 2.64979 | p < .001 |
| umichbiological2 | MXF | 0.8147429 | -1.3669 | 5.5533 | p < .001 |
| upperbuffalo | DBF | 0.7614552 | -1.7913 | 6.8995 | p < .001 |
| usgseros | GR | 0.7550327 | -0.9295 | 3.7132 | p < .001 |
| usmpj | ONF | 0.4718627 | -1.3454 | 5.0362 | P <.001 |
| vaira | GR | 0.9166459 | -1.03342 | 4.5225 | p < .001 |
| willowcreek | DBF | 0.8536744 | -0.87503 | 4.07814 | p < .001 |
| windriver | CNF | 0.25331 | 0.09341 | 1.85488 | P <.01 |
| woodshole | DBF | 0.7762952 | -1.3144 | 5.1137 | p < .001 |

GCC = green chromatic component.
[a] International Geosphere–Biosphere Programme (IGBP) vegetation classes: CNF = closed neadleleaf forest; DBF = deciduous broadleaf forest; GR = grasslands; MXF = mixed needleleaf and deciduous forest; ONF = open needleleaf forest; SH = shrublands.

**Pacific Northwest Research Station**

| | |
|---|---|
| **Website** | https://www.fs.usda.gov/pnw/ |
| **Telephone** | (503) 808–2100 |
| **Publication requests** | (503) 808–2138 |
| **FAX** | (503) 808–2130 |
| **E-mail** | sm.fs.pnw_pnwpubs@usda.gov |
| **Mailing address** | Publications Distribution<br>Pacific Northwest Research Station<br>P.O. Box 3890<br>Portland, OR 97208–3890 |

U.S. Department of Agriculture
Pacific Northwest Research Station
1220 SW 3rd Ave., Suite 1400
P.O. Box 3890
Portland, OR 97208–3890